

The Effect of Electrode Coupling on Single Molecule Device Characteristics:
An X-Ray Spectroscopy and Scanning Probe Microscopy Study

Arunabh Batra

Submitted in partial fulfillment of the
requirements for the degree of
Doctor of Philosophy
in the Graduate School of Arts and Science

COLUMBIA UNIVERSITY
2014

© 2014
Arunabh Batra
All rights reserved

Abstract

The Effect of Electrode Coupling on Single Molecule Device Characteristics: An X-Ray Spectroscopy and Scanning Probe Microscopy Study

Arunabh Batra

This thesis studies electronic properties of molecular devices in the limiting cases of strong and weak electrode-molecule coupling. In these two limits, we use the complementary techniques of X-Ray spectroscopy and Scanning Tunneling Microscopy (STM) to understand the mechanisms for electrode-molecule bond formation, the energy level realignment due to metal-molecule bonds, the effect of coupling strength on single-molecule conductance in low-bias measurements, and the effect of coupling on transport under high-bias. We also introduce molecular designs with inherent asymmetries, and develop an analytical method to determine the effect of these features on high-bias conductance. This understanding of the role of electrode-molecule coupling in high-bias regimes enables us to develop a series of functional electronic devices whose properties can be predictably tuned through chemical design.

First, we explore the weak electrode-molecule coupling regime by studying the interaction of two types of paracyclophane derivatives that are coupled ‘through-space’ to underlying gold substrates. The two paracyclophane derivatives differ in the strength of their intramolecular

through-space coupling. X-Ray photoemission spectroscopy (XPS) and Near-Edge X-ray Absorbance Fine Structure (NEXAFS) spectroscopy allows us to determine the orientation of both molecules; Resonant Photoemission Spectroscopy (RPES) then allows us to measure charge transfer time from molecule to metal for both molecules. This study provides a quantitative measure of charge transfer time as a function of through-space coupling strength. Next we use this understanding in STM based single-molecule current-voltage measurements of a series of molecules that couple through-space to one electrode, and through-bond to the other. We find that in the high-bias regime, these molecules respond differently depending on the direction of the applied field. This asymmetric response to electric field direction results in diode-like behavior. We vary the length of these asymmetrically coupled molecules, and find that we can increase the rectifying characteristics of these molecules by increasing length.

Next, we explore the strong-coupling regime with an X-Ray spectroscopy study of the formation of covalent gold-carbon bonds using benzyltrimethyltin molecules on gold surfaces in ultra high vacuum conditions. Through X-ray Photoemission Spectroscopy (XPS) and X-ray absorption measurements, we find that the molecule fragments at the Sn-Benzyl bond when exposed to gold and the resulting benzyl species only forms covalent Au-C bonds on less coordinated Au surfaces like Au(110). We also find spectroscopic evidence for a gap state localized on the Au-C bond that results from the covalent nature of the bond. Finally, we use Density Functional Theory based Nudged Elastic Band methods to find reaction pathways and energy barriers for this reaction.

We use our knowledge of the electronic structure of these bonds to create single-molecule junctions containing Au-C bonds in STM-based break junction experiments. In analogy with our approach for the weakly coupled ‘through-space’ systems, we study the high-bias current-voltage characteristics of molecules with one strong Au-C bond, and one weaker

donor-acceptor bond. These experiments reveal that the ‘gap state’ created due to the covalent nature of the Au-C bond remains essentially pinned to the Fermi level of its corresponding electrode, and that most of the electric potential drop in the junction occurs on the donor-acceptor bond; as a result, these molecules behave like rectifiers. We use this principle to create a series of three molecular rectifiers, and show that the unique properties of the Au-C bond allow us to easily tune the rectification ratio by modifying a single electronic parameter.

We then explore the process of molecular self-assembly to create organic electronic structures on metal surfaces. Specifically, we study the formation of graphene nanoribbons using a brominated precursor deposited on Au(111) surface in ultra high vacuum. We find that the halogen atoms cleave from the precursors at surprisingly low temperatures of <100C, and find that the resulting radicals bind to Au, forming Au-C and Au-Br bonds. We show that the Br desorbs at relatively low temperatures of <250C, and that polymerization of the precursor molecules to form nanoribbons proceeds only after the debromination of the surface. Finally, with Angle-Resolved Photoemission and Density Functional Theory calculations, we quantify the interaction strength of the resulting nanoribbons with the underlying gold substrate.

Taken together, the results presented in this thesis offer a mechanistic understanding of the formation of electrode-molecule bonds, and also an insight into the high-bias behavior of molecular junctions as a function of electrode-molecule coupling. In addition, our work in developing tunable, functional electronic devices serves as a framework for future technological advances towards molecule-based computation.

Contents

List of Figures	iv
List of Tables	vii
1 Introduction and Outline	1
1.1 Electron Transport in Molecular Junctions	2
1.1.1 Describing Electron Transport in One Dimension	2
1.1.2 The Tight Binding Model	5
1.1.3 Quantum Interference	8
1.1.4 Experimental Techniques	11
1.2 Electron Transfer at Molecule-Metal Interfaces	14
1.2.1 X-Ray Photoemission Spectroscopy	14
1.2.2 Near-Edge X-Ray Absorbance Fine Structure Spectroscopy	16
1.2.3 Resonant Photoemission Spectroscopy	20
1.2.4 Outline	22
2 Through-Space Interactions	23
2.1 Quantifying Through-Space Charge Transfer Dynamics in π -Coupled Molecular Systems	23
2.1.1 Preface	23
2.1.2 Abstract	24
2.1.3 Introduction	24
2.1.4 Results	28
2.1.4.1 Comparison of Monolayer Films	28
2.1.4.2 Resonant Photoemission Measurements	30
2.1.4.3 Determining Charge Transfer Times	33
2.1.5 Conclusion	36
2.1.6 Methods	36
2.1.6.1 Experimental Methods	36
2.1.6.2 Charge Transfer Model	38

2.1.6.3	Supplementary Information	39
2.2	Molecular Diodes Enabled by Quantum Interference	46
2.2.1	Preface	46
2.2.2	Abstract	46
2.2.3	Introduction	46
2.2.4	Experimental Method	48
2.2.5	Results	49
2.2.6	Supplementary Information	54
2.2.6.1	Synthesis	54
3	The Covalent Gold-Carbon Bond	58
3.1	Trimethyltin mediated gold-carbon bond formation	58
3.1.1	Preface	58
3.1.2	Abstract	59
3.1.3	Introduction	59
3.1.4	Experimental Methods	61
3.1.4.1	Theoretical Methods	66
3.1.5	Conclusion	70
3.1.6	Supplementary Information	70
3.1.6.1	Reaction Pathway Calculations	70
3.1.6.2	NEXAFS Calculations	74
3.1.6.3	Calculation of Stoichiometric ratios from XPS	75
3.2	Tuning Rectification in Highly Conductive Single-Molecular Diodes	76
3.2.1	Preface	76
3.2.2	Abstract	76
3.2.3	Introduction	77
3.2.4	Experimental Methods	78
3.2.5	Results	81
3.2.6	Tuning Rectification	84
3.2.7	Supplementary Information	87
3.2.7.1	Density Functional Theory	91
3.2.7.2	Tight Binding Model	96
4	Self-Assembly of Molecular Electronic Components	102
4.1	Probing the Mechanism for Graphene Nanoribbon Formation on Gold Surfaces through X-ray Spectroscopy	102
4.1.1	Preface	102
4.1.2	Abstract	103
4.1.3	Introduction	103
4.1.4	Experimental Methods	104
4.1.5	Results	105
4.1.6	Supplementary Information	111

List of Figures

1.1	Model of a Metal-Molecule-Metal Junction	5
1.2	Conductance pathways for naphthalene	10
1.3	Modeling Quantum Interference Effects	11
1.4	Schematic of STM-BJ Measurements	13
1.5	Schematic of XPS and AES Processes	15
1.6	Schematic of NEXAFS Absorption	17
1.7	Effect of Electric Field Polarization on NEXAFS	18
1.8	NEXAFS spectrum of benzene	19
1.9	Schematic representation of various photoexcitation processes.	21
2.1	Schematic representation of different photoexcitation processes	26
2.2	Chemical Structures	27
2.3	Comparison of XPS and NEXAFS Spectra	29
2.4	Resonant Photoemission (RPES) Intensity Maps	31
2.5	The Charge Transfer Model	32
2.6	Effect of Azimuthal orientation on shadowing	42
2.7	Bonding and Antibonding combinations of xylene LUMO	44
2.8	Molecular Structures and Conductance Data	49
2.9	Current-Voltage Measurement	51

2.10	Model for Rectification and Simulated IV Curves	53
2.11	Effect of electric field on orbital projections and energies	57
3.1	Molecular Structure and Tin XPS Measurement	62
3.2	Carbon XPS and Stoichiometric Ratios	63
3.3	NEXAFS Measurements	64
3.4	Calculated Trajectories and Density of States	68
3.5	Transition state for NEB	70
3.6	Intact molecule on Au(111) surface with adatom	71
3.7	Benzyl and trimethyltin configurations	73
3.8	Calculated NEXAFS spectra for Au ₁ -Benzyl	74
3.9	Experimental and analytical method for current-voltage measurements	80
3.10	Calculated transmission functions and IV curves	83
3.11	Tuning rectification through molecular design	86
3.12	Data selection and sorting methods	89
3.13	Symmetric Control Molecules	91
3.14	Curves for Symmetric Control Molecules	92
3.15	DFT Optimized Geometries	93
3.16	Scattering states for molecule 1	94
3.17	Potential profile for molecule 1 at 50mV to 1V	95
3.18	Potential profile across molecular diode	97
3.19	Tight binding model for rectifiers	98
3.20	Transmission Curves from Tight Binding	100
4.1	Nanoribbon Formation Scheme and XPS Results	105
4.2	NEXAFS and UPS Spectroscopy	107
4.3	Evolution of the Shockley Surface State via ARPES	110

4.4	Helium Atom Scattering with Temperature Ramp	114
4.5	Comparing HAS and XPS signals	115
4.6	UPS measurements show GNR film saturation	116
4.7	Temperature dependent XPS on Au(110)	117
4.8	HAS on DBBA/Au(110)	118
4.9	Unit cell of the GNR + Au(111) surface system used in the calculations . .	119
4.10	Surface Band energy level convergence	120

List of Tables

3.1	Binding Energies with vdW-optB86b functional	72
3.2	Binding Energies with PBE functional (no van der Waals)	72
3.3	Parameters for tight binding model	101

To my parents, Sonali and Anil Batra

Chapter 1

Introduction and Outline

In 1958, Colonel C.H. Lewis of the Air Research and Development Command[1], unsatisfied with the slow progress made by the semiconductor industry in delivering small, light, reliable electronics for the Air-force's flying machines, proposed this radical new idea:

Instead of taking known materials which will perform explicit electronic functions, and reducing them in size, we should build materials which due to their inherent molecular structure will exhibit certain electronic property phenomena. Once we can correlate electronic property phenomena with the chemical, physical, structural, and molecular properties of matter, we should be able to tailor materials with predetermined characteristics. We call this more exact process of constructing materials with predetermined electrical characteristics *Molecular Electronics*[1].

The prescience of this idea is seen in the fact that 56 years hence, the goals of *Molecular Electronics* remain essentially the same. The modern view of the field was shaped by Ari Aviram and Mark Ratner's seminal paper on molecular diodes in 1974[2], where they proposed a simple organic molecule sandwiched between two metal electrodes that could potentially act as a diode element. The more general vision of this paper is the attractive idea that chemically attaching functional units to a carbon backbone could dramatically

alter the electronic properties of the backbone itself. While much experimental and theoretical progress has been made towards this vision, replacing current silicon-based computational devices is still a distant dream. There remain many obstacles in the road towards truly functional molecular electronics: assembling many molecular components into multi-component circuits, understanding energy level alignment between molecule and electrode, the response of molecular orbitals to high electric fields, improving the thermal and mechanical stability of chemical linker groups, among others[3].

In this thesis, I report the results of a study of the electronic and chemical properties of three distinct organic-electronic systems using a combination of Scanning Tunneling Microscopy (STM) and X-Ray Spectroscopy techniques. These results address many of the major challenges in molecular electronics mentioned above, and are a step towards the grand goal of using single molecules as commercial circuit elements . The remainder of this chapter presents a brief theoretical and experimental background of the methods used in this thesis.

1.1 Electron Transport in Molecular Junctions

1.1.1 Describing Electron Transport in One Dimension

The Landauer-Buttiker formalism[4, 5] is perhaps the most well accepted theoretical framework for describing ballistic transport in one dimension. This method converts the electron transport problem into a scattering problem. In this formalism, the conductance \mathcal{G} of a metal-molecule-metal junction is related to the probability of an electron from one electrode, emerging at the Fermi energy E_F (modulo any applied bias), being transmitted across the molecular junction. The conductance \mathcal{G} is given by

$$\mathcal{G} = \mathcal{G}_0 T(E_F) = \frac{2e^2}{h} \sum_i T_i(E_F) \quad (1.1)$$

where e is the charge of an electron, h is Planck's constant, i is the index associated with a conducting channel, and $\mathcal{G}_0 = \frac{2e^2}{h}$ is the *quantum of conductance*. A heuristic argument[6] for the *quantum of conductance* can be made using the Uncertainty Principle. Current can be defined as $I = e/\Delta t$ where Δt is defined as the time taken for an electron to traverse a channel. The energy difference between source and drain electrodes, $\Delta E = eV$, where V is the applied voltage. Combining these two equations, we have $\mathcal{G} = \frac{I}{V} = \frac{e^2}{\Delta t \Delta E} \propto \frac{e^2}{h}$. That a macroscopically observable quantity like \mathcal{G} is related to a quantum transmission probability, a coherent property, results from the fact that even at room temperature and higher biases, inelastic scattering lengths are large compared to the typical size of molecular junctions[6]. A more detailed analysis of the origin of \mathcal{G}_0 is shown elsewhere[6, 7, 8]. In this thesis, we use an alternative formulation of the Landauer approach based on solving the Schrödinger Equation using Non Equilibrium Green's Functions (NEGF). The NEGF approach is more convenient than directly solving the forward eigenvalue problem as it allows the electrodes and molecules to be treated independently, thus allowing external perturbations (like electric fields) to be incorporated into calculations easily [9]. Here, I briefly summarize the basic aspects of NEGF. I base the following description on two excellent review articles by Paulsson, Zahid and coworkers[7, 10].

In the localized basis of our choice, the Schrödinger Equation is given by

$$\begin{array}{ccc} H |n\rangle & = & E |n\rangle \\ \left[\begin{array}{ccc} H_l & \tau_l & 0 \\ \tau_l^\dagger & H_d & \tau_r^\dagger \\ 0 & \tau_r & H_r \end{array} \right] \left[\begin{array}{c} |ll\rangle \\ |d\rangle \\ |rl\rangle \end{array} \right] & = & E \left[\begin{array}{c} |ll\rangle \\ |d\rangle \\ |rl\rangle \end{array} \right] \end{array}$$

Here, we define $|ll\rangle, |rl\rangle$ and $H_{l,r}$ as the wavefunctions and Hamiltonians for left and right electrodes, $|d\rangle$ and H_d as those for the device (the molecule), and $\tau_{l,r}$ as coupling constants between electrodes and device. The Green's function for this equation is:

$$(E - H)G(E) = I$$

where I is the Identity, and $G(E)$ is the Green's function solution. The advantages of using such an approach are two-fold: first, for large basis sets describing multi-atom junctions, solving for $G(E)$ is simpler; second, this method allows us to calculate the Green's function solution for the device region, $G_d(E)$, separate from the electrodes. Solving this equation results in the following Green's function for the device region:

$$G_d = (E - H_d - \Sigma_l - \Sigma_r)^{-1} \quad (1.2)$$

where $\Sigma_{l,r} = \tau_{l,r}^\dagger (E - H_{l,r})^{-1} \tau_{l,r}$ are called the *self-energies* of the left and right electrodes. In the above equation, the *self-energy* matrices have two effects. The real parts of $\Sigma_{l,r}$ serve to renormalize the energy eigenvalues of H_d , while the imaginary parts serve to broaden these energy levels. We can use this formalism to calculate the current flowing through the device (See Ref. [10] for details):

$$I = \frac{2e}{h} \int_{E=-\infty}^{\infty} dE (f(E, \mu_l) - f(E, \mu_r)) \text{Tr}(G_d^\dagger \Gamma_r G_d \Gamma_l) \quad (1.3)$$

where $\Gamma_{l,r} = i(\Sigma_{l,r} - \Sigma_{l,r}^\dagger)$ are hermitian *coupling matrices* for left and right leads, and the conductance

$$\mathcal{G}(E_F) = \frac{2e^2}{h} \text{Tr}(G_d^\dagger \Gamma_r G_d \Gamma_l) \quad (1.4)$$

Equations 1.4 and 1.3 allow us to calculate conductance and current-voltage character-

istics for molecular junctions.

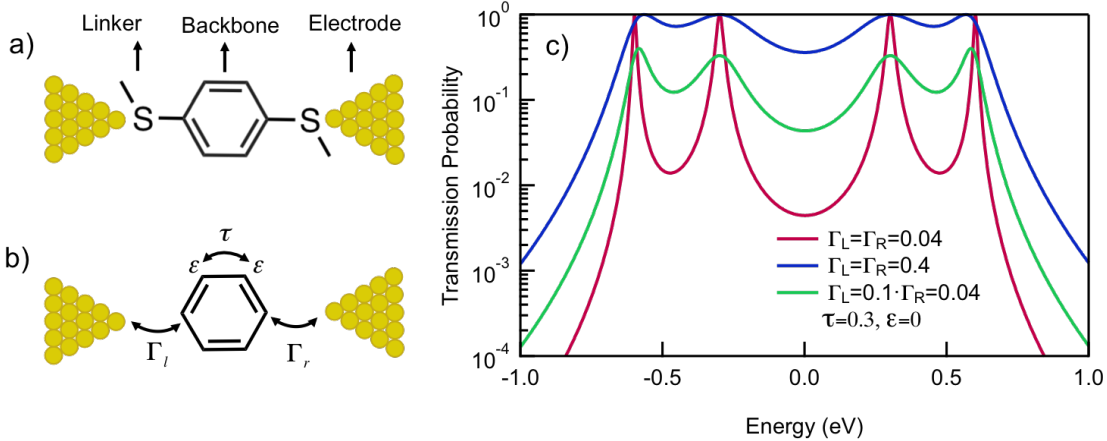


Figure 1.1 – Model of a Metal-Molecule-Metal Junction

a A molecular junction can be seen as a molecular backbone connected to metal electrodes through chemical anchoring groups, or linkers, which define the coupling strength of the electrodes to the molecule. **b** A simplified tight-binding model of this junction involving the p_z atomic orbitals of each carbon atom with an on-site energy ε , coupled to nearest-neighboring orbitals via τ . The molecule is coupled to metal electrodes via $\Gamma_{l,r}$. **c** Transmission probability $T(E)$ calculated using the tight-binding hamiltonian. Increasing the value of $\Gamma_{l,r}$ broadens the molecular orbitals (red curve to blue curve). If coupling constants $\Gamma_{l,r}$ are not equal on left and right electrodes, transmission probabilities for conducting channels do not reach unity (green curve).

1.1.2 The Tight Binding Model

Detailed calculations of junction characteristics based on the formalism outlined above are usually carried out numerically, using Density Functional Theory optimized geometries to define coupling terms, and periodic boundary conditions to describe the electrodes. However, an intuitive understanding of the conductance characteristics of molecular wires can be gained using simple tight-binding based methods. Here I present an example of the tight-binding method used to calculate electronic transmission through benzene, a simple organic molecule, connected to a left and right electrode (Figure 1.1b).

We consider a 6-site model of benzene, with each carbon atom contributing a p_z orbital and interacting with its nearest neighbor; for simplicity, we do not explicitly include the methylsulfide[11] linker groups in our model. The hamiltonian representing the device, H_d then has the form

$$H_d = \begin{bmatrix} \varepsilon & \tau & 0 & 0 & 0 & \tau \\ \tau^\dagger & \varepsilon & \tau & 0 & 0 & 0 \\ 0 & \tau^\dagger & \varepsilon & \tau & 0 & 0 \\ 0 & 0 & \tau^\dagger & \varepsilon & \tau & 0 \\ 0 & 0 & 0 & \tau^\dagger & \varepsilon & \tau \\ \tau^\dagger & 0 & 0 & 0 & \tau^\dagger & \varepsilon \end{bmatrix}$$

$$\begin{aligned} \varepsilon &= \langle \psi_i | H_d | \psi_i \rangle \\ \tau &= \langle \psi_i | H_d | \psi_j \rangle, i \neq j \end{aligned}$$

The self-energies $\Sigma_{l,r}$ are taken to be purely imaginary, resulting in coupling matrices of the form:

$$\Gamma_l = \begin{bmatrix} \Gamma_l & 0 & 0 & 0 & 0 & 0 \\ 0 & 0 & 0 & 0 & 0 & 0 \\ 0 & 0 & 0 & 0 & 0 & 0 \\ 0 & 0 & 0 & 0 & 0 & 0 \\ 0 & 0 & 0 & 0 & 0 & 0 \\ 0 & 0 & 0 & 0 & 0 & 0 \end{bmatrix} \quad \Gamma_r = \begin{bmatrix} 0 & 0 & 0 & 0 & 0 & 0 \\ 0 & 0 & 0 & 0 & 0 & 0 \\ 0 & 0 & 0 & 0 & 0 & 0 \\ 0 & 0 & 0 & \Gamma_r & 0 & 0 \\ 0 & 0 & 0 & 0 & 0 & 0 \\ 0 & 0 & 0 & 0 & 0 & 0 \end{bmatrix}$$

Using Equation 1.2, we get a Green's function equation:

$$G_d = \begin{bmatrix} E - \varepsilon - \frac{i\Gamma_l}{2} & \tau & 0 & 0 & 0 & \tau \\ \tau^\dagger & E - \varepsilon & \tau & 0 & 0 & 0 \\ 0 & \tau^\dagger & E - \varepsilon & \tau & 0 & 0 \\ 0 & 0 & \tau^\dagger & E - \varepsilon - \frac{i\Gamma_r}{2} & \tau & 0 \\ 0 & 0 & 0 & \tau^\dagger & E - \varepsilon & \tau \\ \tau^\dagger & 0 & 0 & 0 & \tau^\dagger & E - \varepsilon \end{bmatrix}^{-1}$$

From here, the conductance \mathcal{G} can be calculated using Equation 1.4. In Figure 1.1c, I show the numerically calculated conductance from the tight-binding model for benzene. Here, we assume $E_F = 0$ eV. The transmission function shows four prominent peaks, which correspond to the six molecular orbitals obtained from diagonalizing the hamiltonian. The two peaks closest to E_F correspond the highest occupied molecule orbital (HOMO) at $E=-0.4$ eV, and lowest unoccupied molecular orbital (LUMO) at $E=+0.4$ eV. Both these orbitals are degenerate, giving us 6 total molecular orbitals as expected. The transmission function $T(E)$ peaks at 1 for energies equal to molecular orbital energies. Transport in this regime is considered *resonant transport*, providing the quantum of conductance of $\mathcal{G}_0 = \frac{2e^2}{h}$ available through a fully open channel. However in general, E_F is not aligned to a molecular resonance, and conductances much lower than \mathcal{G}_0 are observed. The three curves in Figure 1.1c serve to illustrate the role of the coupling matrices, Γ_i , in determining the shape of the transmission function. As Γ_i is increased, the width of the transmission peaks increases, resulting in higher conductance and a flatter density of states near E_F . It is interesting to note that in the case of unequal Γ_i , transmission does not go to unity (green curve). Such a situation will be discussed in the context of asymmetrically contacted

molecular rectifiers later in this thesis.

1.1.3 Quantum Interference

One of the unique features of scaling electronic transport down to the single-molecule level is that conduction becomes a coherent process. This opens the possibility of exploiting *wave-like* phenomena to create unexpected electronic properties. Quantum interference is one such phenomenon that has generated a tremendous amount of interest because of its possible uses in technological applications such as molecular transistors [12, 13, 14, 15, 16, 17] and molecular diodes. In essence, interference results from the coherent sum of transmission functions from different conducting channels (for example, HOMO and LUMO) which can be entirely constructive or destructive, depending on the energy of the incoming electron and phase difference between the two pathways. Here, I follow the approach of Yoshizawa et al. [16] to explain Quantum Interference effects from a localized orbital perspective.

Using a nearest-neighbor approximation, Equation 1.2 can be converted into a form that results in

$$G(E) \propto G^0$$

where G^0 is a matrix representing the *zeroth order Green's function* of the device[16]. The matrix elements of G^0 are of the form

$$G_{\alpha\beta}^0 \propto \sum_m \frac{C_{\alpha,m} C_{\beta,m}^\dagger}{E - \varepsilon_m \pm i\eta} \quad (1.5)$$

where m is an index of all molecular orbitals, ε_m is the orbital energy, $C_{\alpha m}$ and $C_{\beta m}$ are the projections of the molecular orbital m on the atomic sites α and β on the molecule, and η is an infinitesimally small constant. The intuitive result of this representation is

that the projections $C_{\alpha,m}$ and $C_{\beta,m}$ must have the correct sign in order for the terms in the summation not to cancel each other.

Consider connecting a molecule to electrodes at sites α and β . In such a case, Equation 1.5 can be expanded as:

$$G_{\alpha\beta}^0 \propto \dots + \frac{C_{\alpha,HOMO-n} C_{\beta,HOMO-n}^\dagger}{E - \varepsilon_{HOMO-n} \pm i\eta} + \dots + \frac{C_{\alpha,HOMO} C_{\beta,HOMO}^\dagger}{E - \varepsilon_{HOMO} \pm i\eta} + \\ \frac{C_{\alpha,LUMO} C_{\beta,LUMO}^\dagger}{E - \varepsilon_{LUMO} \pm i\eta} + \dots + \frac{C_{\alpha,LUMO+n} C_{\beta,LUMO+n}^\dagger}{E - \varepsilon_{LUMO+n} \pm i\eta} + \dots$$

Since the Fermi energy E_F is generally in between ε_{HOMO} and ε_{LUMO} , these two terms dominate the expansion:

$$G_{\alpha\beta}^0 \propto \frac{C_{\alpha,HOMO} C_{\beta,HOMO}^\dagger}{E - \varepsilon_{HOMO} \pm i\eta} + \frac{C_{\alpha,LUMO} C_{\beta,LUMO}^\dagger}{E - \varepsilon_{LUMO} \pm i\eta}$$

As E_F is between ε_{HOMO} and ε_{LUMO} , the denominators of these terms will have opposite signs, and therefore the projections in the numerators must have opposite phase in order not to cancel completely. In the case that they do cancel, complete destructive interference results, and the molecule does not conduct. An example of this phenomenon is shown in Figure 1.2. Here, connecting a naphthalene molecule to electrodes at the 1 and 4 positions results in the product $C_{1,HOMO} C_{4,HOMO}^\dagger$ having a negative sign, and $C_{1,LUMO} C_{4,LUMO}^\dagger$ having a positive sign. Since the denominators of the two terms also have opposite signs, the sum is non-zero and constructive interference occurs between the HOMO and LUMO pathways. Alternatively, connecting the molecule to electrodes at the 2 and 7 positions results in destructive interference.

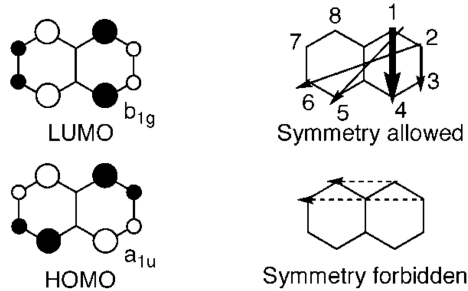


Figure 1.2 – Conductance pathways for naphthalene

Adapted from Reference [16]. The left panel shows projections of HOMO and LUMO of naphthalene, where phases of the orbitals is represented by black and white. The right panel shows the conductance pathways showing constructive interference (symmetry allowed) and destructive interference (symmetry forbidden).

It is important to note that this picture is correct insofar as the nearest neighbor and independent electron approximations are valid. These rules break down in certain molecular systems [18] where electron-electron interactions become important. Here, I restrict my description to cases where this approach accurately predicts constructive and destructive interference.

To illustrate this example further, I return to the model of Figure 1.1b. Figure 1.3a shows the possible configurations when connecting a benzene ring to two electrodes. Figure 1.3b shows their corresponding transmission functions calculated using the same hamiltonian discussed in the earlier section. The only difference is in the position of the non-zero entry in the coupling matrix Γ_r , which represents the position at which the right electrode contacts the benzene ring. The meta connected (red) transmission function shows a dip in conductance at $E_F = 0$, and suggests that no conductance should be observed for such a molecule. This has been experimentally confirmed in conductive-AFM studies which show no conductance signature but do show a force associated with the meta connected molecule binding to metal electrodes.[19, 20].

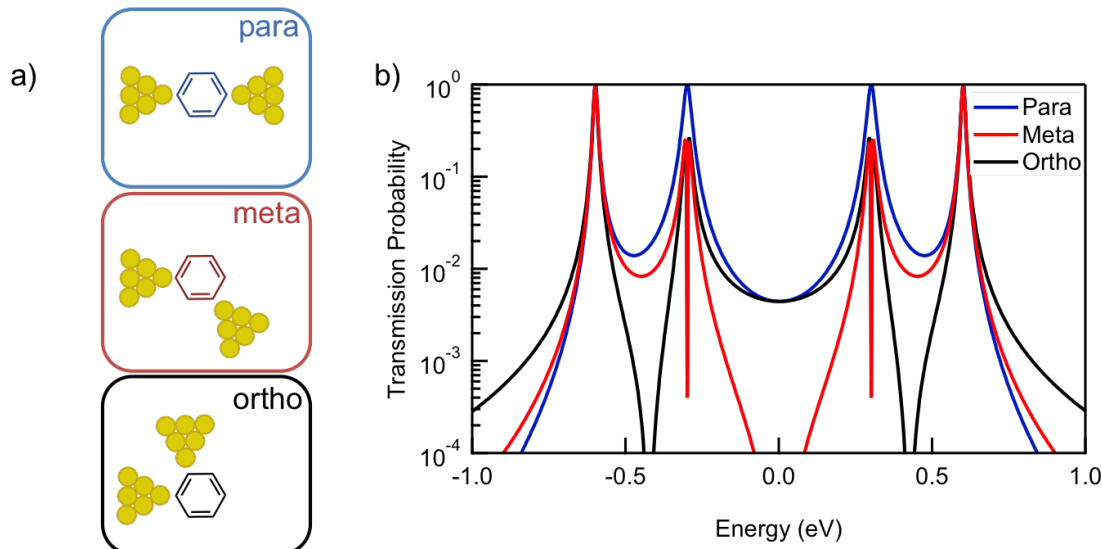


Figure 1.3 – Modeling Quantum Interference Effects

a Three possible electrode configurations to connect to a benzene ring, labeled *para*, *meta*, and *ortho*. **b** Transmission functions corresponding to these three electrode configurations. *Para* (blue curve) shows non-negligible transmission due to constructive interference between HOMO and LUMO orbitals. In contrast, *meta* (red) connected junctions show a sharp dip at E_F resulting in negligible conductance through the junction because of complete destructive interference. *ortho* (black) shows similar destructive interference, but in this case between HOMO-1 and HOMO and LUMO-1 and LUMO.

1.1.4 Experimental Techniques

A variety of experimental techniques are used to create single or few molecule circuits, including mechanically controlled break junctions (MCBJ) [21], electromigration techniques[22, 23], functionalized carbon nanotube electrodes[24], photolithographic methods[25], and scanning tunneling microscopy in break junction mode (STM-BJ)[26]. In this thesis, we focus on the STM-BJ technique, and present a brief overview of the method. Typically, our STM-BJ measurements are performed using a gold substrate made by thermally evaporating \sim 100 nm of gold on freshly cleaved mica. A gold STM tip is made by hand-cutting 0.25 mm thick gold wire. A bias is applied to either tip or substrate while grounding

the other electrode through a transimpedance amplifier (current-to-voltage converter). The tip is brought into and out of contact (See Figure 1.4 with the substrate using a piezoelectric stage while current and applied voltage are both measured. To measure molecular conductance, experiments are performed in a dilute solution ($\sim 1\text{mM}$) of the molecule of interest in a non-polar solvent. In the schematic shown in Figure 1.4a, break junction measurements are performed using gold tip and substrate electrodes in a solution of stilbenoid molecules with methylsulfide linker groups. Sample traces in Figure 1.4b show quantized conductance at integer multiples of \mathcal{G}_0 , until the final gold-gold point contact is broken. The tunneling current drops abruptly, until a plateau is seen at around $10^{-3}\mathcal{G}_0$. The tip continues to be retracted until the molecular junction is broken, and measured conductance drops to the experimental noise floor. Several thousand such traces are taken, resulting in a conductance histogram as shown in Figure 1.4c. The sharp features at integer multiples of \mathcal{G}_0 correspond to gold-gold junctions, while the broad peak at $3 \times 10^{-3}\mathcal{G}_0$ corresponds to the molecular feature.

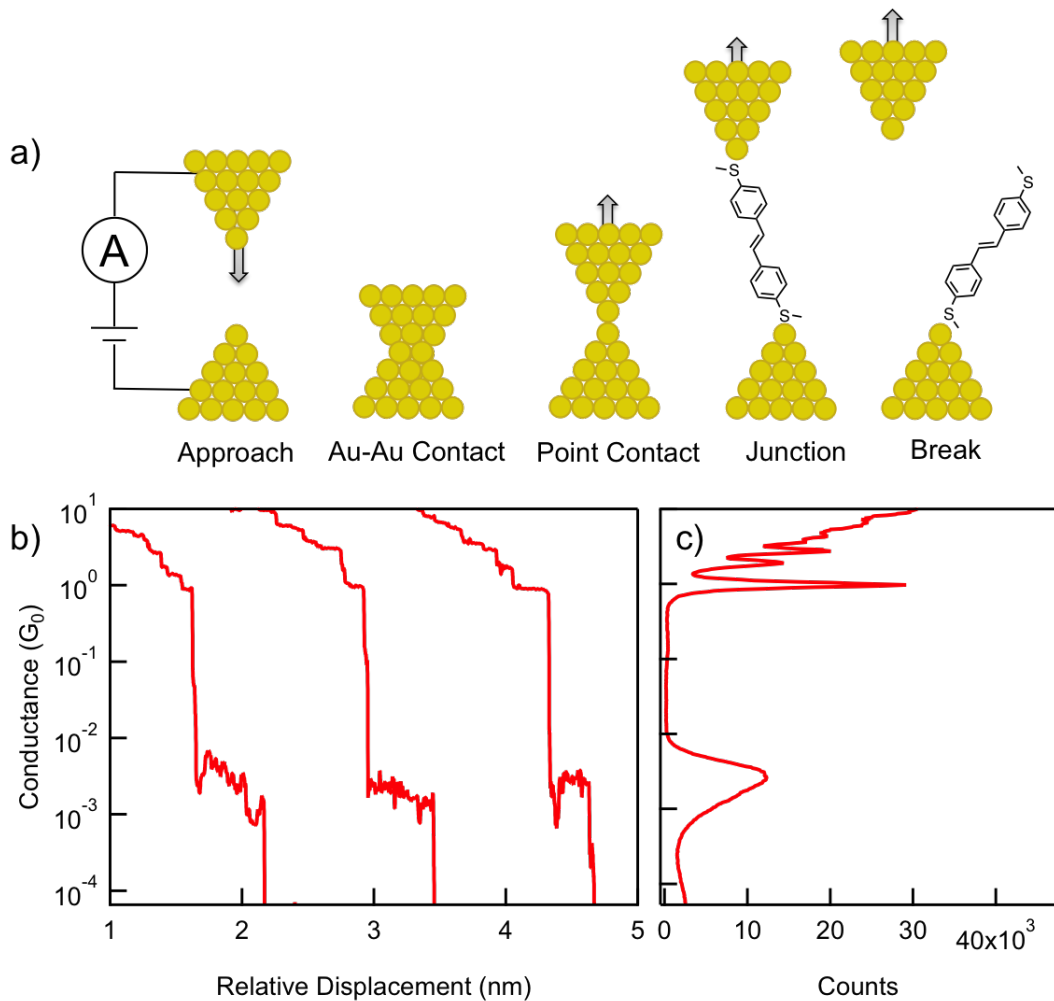


Figure 1.4 – Schematic of STM-BJ Measurements

a The evolution of single molecule junction formation. **L-R:** A sharp gold tip approaches a gold substrate; a multi-atom gold-gold contact is formed, the gold tip is then retracted until a single gold-gold point contact is created with a conductance of $1G_0$. As the tip continues to retract, a molecule from solution becomes trapped in the junction, resulting in a stable gold-molecule-gold circuit. Next the molecular contact breaks. **b** Sample conductance traces on a log scale vs. tip-substrate displacement. Traces show decreasing quantized conductance steps at integer multiples of G_0 as the tip is pulled away from the surface. The final step at $1G_0$ is followed by a sharp drop, and then a plateau near $10^{-3}G_0$ corresponding to the molecular conductance. **c** Conductance histogram made from thousands of traces result is a statistical measure of the characteristic conductance of a molecule.

1.2 Electron Transfer at Molecule-Metal Interfaces

1.2.1 X-Ray Photoemission Spectroscopy

X-Ray Photoemission Spectroscopy (XPS) is a common surface science technique used to characterize elemental composition of samples and chemical bonding in materials[27, 28]. In general, samples to be measured are prepared in ultra-high vacuum conditions and exposed to X-Ray spectrum radiation. There is a finite probability of the impinging photons interacting with bound electrons in the sample material, resulting in the ejection of these electrons (Figure 1.5b); the kinetic energy of these electrons can be measured, and can be converted into a characteristic binding energy of the electron, E_b using the following formula:

$$E_b = E_{final} - E_{initial} = h\nu - E_{kin} - \phi$$

where E_b is binding energy, E_{kin} is the measured kinetic energy, $h\nu$ is the energy of the incoming photon, and ϕ is the work function of the sample. Usually, a fixed photon energy $h\nu$ is used, and a variable energy electron analyzer (most commonly an electrostatic hemispherical detector) measures photoemitted electron intensity as a function of electron kinetic energy, which is then converted into a binding energy. The characteristic binding energy allows the identification of the element and the local chemical environment it is in.

In general, the electronic levels of interest are core level electrons, such as 1s levels of carbon, oxygen or nitrogen, or 2p levels for sulfur or copper. These core level electrons are too deep in energy to be involved in chemical binding, but do experience a shift in E_b based on changes in the atom's electrostatic or chemical environments. The XPS spectra therefore serve as a fingerprint for elemental analysis, and shifts in these spectra probe

local chemical and electronic structure. In conjunction with XPS on core-levels, X-ray photoemission is also used to probe higher energy occupied levels that are often involved in chemical bonding processes. This Valence Band (VB) photoemission (Figure 1.9b) is a complementary technique to other photoemission measurements such as ultraviolet photoemission spectroscopy (UPS).

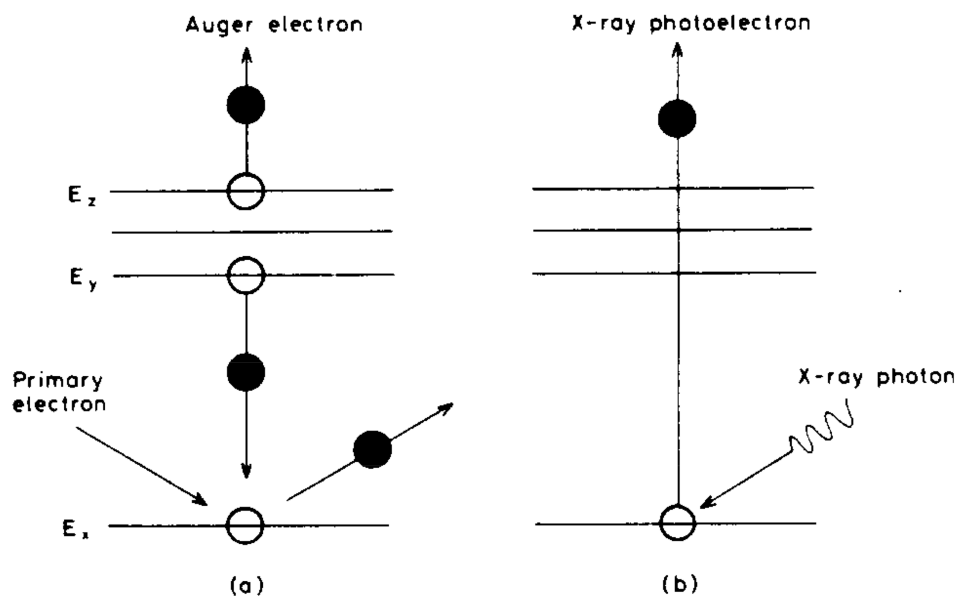


Figure 1.5 – Schematic of XPS and AES Processes

Adapted from [28]. **a** Auger emission process showing direct photoemission from the core level E_x , followed by a non-radiative decay in which the electron E_y fills the core-hole and emits an Auger electron from E_z **b** Direct Photoemission Process from core level E_x .

Both VB and core-level XPS techniques result in the direct photoemission of an electron, leaving behind an ionized atom. The ionized atom may then decay to its group state through radiative or non-radiative processes. An example of a non-radiative process is Auger electron emission (Figure 1.5a), where an electron decays to fill a core-hole and emits another electron. These Auger electrons have low kinetic energies and short inelastic mean free paths, and provide information on the top few atomic layers of the sample under study. Note that the Auger electron decay process described here leaves the atom doubly

ionized, with one electron lost to direct photoemission, and another through Auger decay. This process will be contrasted with 'Resonant Auger' processes discussed in [1.2.3](#).

1.2.2 Near-Edge X-Ray Absorbance Fine Structure Spectroscopy

In contrast to XPS and VB photoemission, Near-Edge X-Ray Absorbance Fine Structure (NEXAFS) spectroscopy is a measure of the unoccupied density of states of a molecule. NEXAFS measures the absorption of photons near strong absorption features (called edges) as a function of photon energy[[29](#), [30](#)]. Since a variable energy X-Ray source with high flux is required for this measurement, these experiments are carried out at synchrotrons. The basic NEXAFS process is outlined in Figure [1.6](#). Here a diatomic molecule is excited by incident light with energy $h\nu$ while a NEXAFS signal is collected (inset). This signal is a result of non-radiative Auger electron decay processes that follow excitation by light. The total Auger electron yield from these processes is counted using an electron multiplier tube (such as a channeltron) as the incident photon energy is swept across absorption edges. At energies that are resonant with atomic transition energies (e.g. $1s \rightarrow \pi^*$), a strong NEXAFS signal is observed (inset).

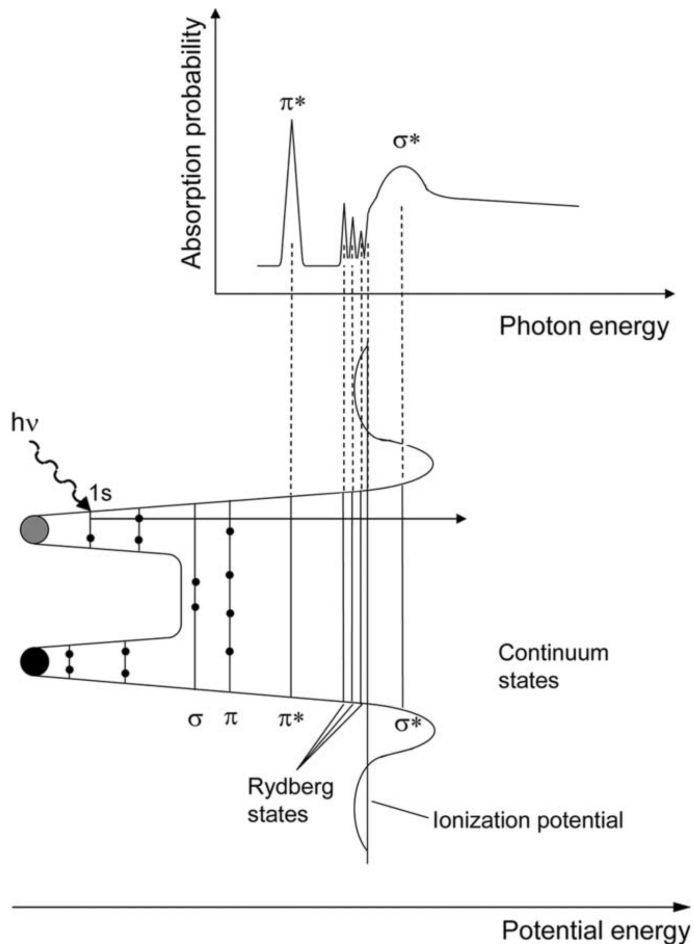


Figure 1.6 – Schematic of NEXAFS Absorption

Adapted from [30]. Schematic potential (bottom axis) and corresponding NEXAS spectrum (inset) for a diatomic molecule. A variable wavelength light source is used to excite the diatom, and strong absorption is seen at incident light energies $h\nu$ corresponding to the $1s \rightarrow \pi^*$ transition, where π^* is the first unoccupied molecular orbital. Higher energy resonances are observed corresponding to Rydberg states and unoccupied σ^* states.

Since NEXAFS spectroscopy involves a dipole transition from an initially bound state (e.g. carbon 1s) to a final state that is also bound (e.g. π^*), dipole transition rules affect the cross-section of the absorbance. Under the dipole approximation [31] the interaction cross-section $\sigma \propto \langle \psi_{final} | \vec{e} \cdot \hat{p} | \psi_{initial} \rangle$ where \hat{p} is the momentum operator for electrons and \vec{e} is the E-field polarization of the incoming light. For K-shell excitations (e.g. carbon 1s),

dipole selection rules ($\Delta l = \pm 1$) require that the final state is a p orbital. Additionally, the $\vec{e} \cdot \hat{p}$ term in the transition matrix results in polarization-dependent excitation of absorbance (Figure 1.7).

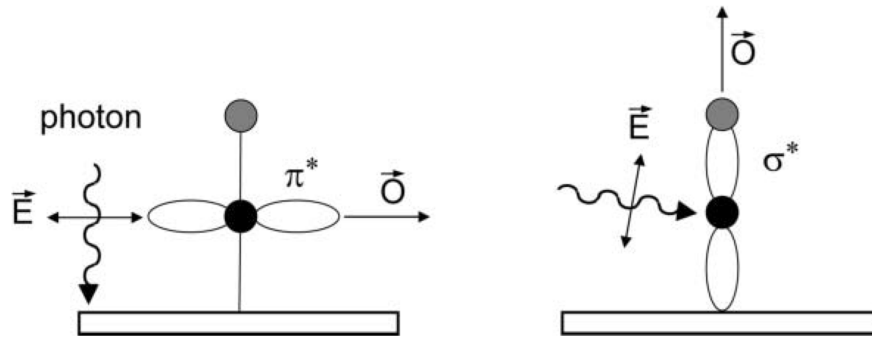


Figure 1.7 – Effect of Electric Field Polarization on NEXAFS

Adapted from [30]. Schematic representation of an incident photon interacting with a π^* resonance. For a $1s \rightarrow \pi^*$ transition, the absorption cross-section is at a minimum when the E-field of incident light is polarized perpendicular to the direction of the π^* orbital (left panel), and a maximum with polarized parallel (right panel).

We can thus gather orientational information on the LUMO by measuring NEXAFS intensity as a function of incident light polarization. An example of using NEXAFS for orientational information is shown in Figure 1.8. Here, a monolayer of benzene is deposited on Ag(110)[32]; the presence of a stronger π^* absorbance feature in the top panel (*p-pol*, incident E-field perpendicular to substrate) than in the bottom panel indicates that the π^* system is aligned perpendicular to the plane of the substrate (equivalently, the benzene ring lies flat on the substrate).

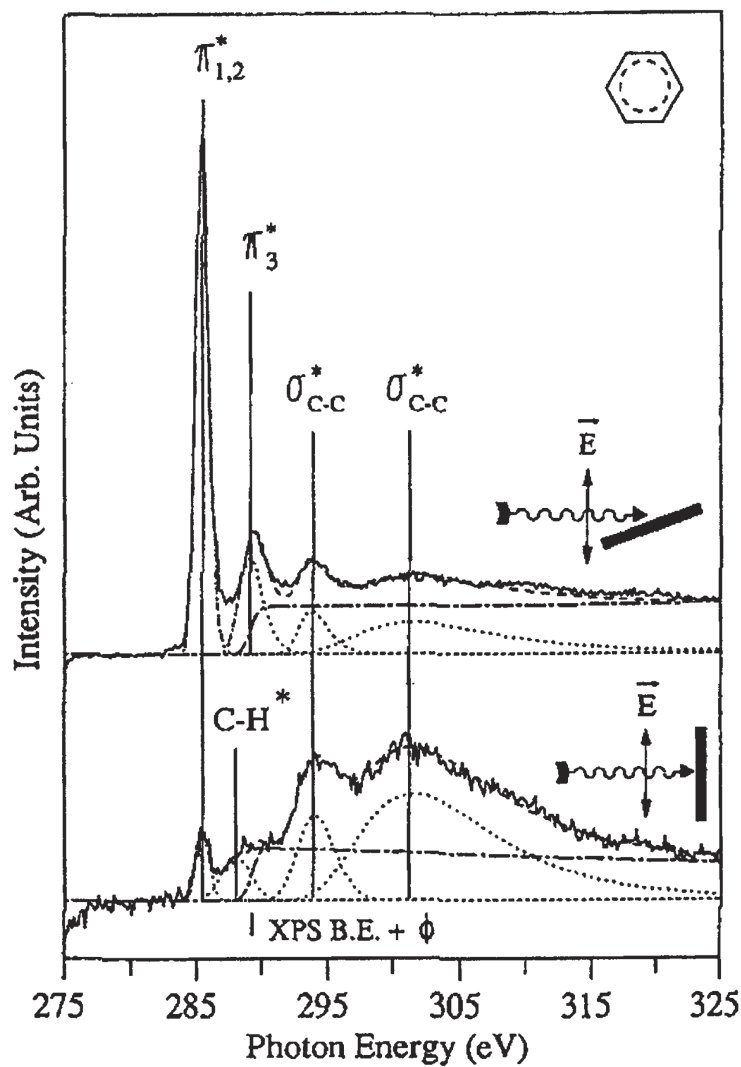


Figure 1.8 – NEXAFS spectrum of benzene

Adapted from [32]. The top panel shows the NEXAFS spectrum of a monolayer of benzene on Ag(110). The top panel shows NEXAFS spectra with incident E-field perpendicular to the plane of the substrate (*p-pol*), and bottom panel shows the spectrum with E-field perpendicular (*s-pol*). The strong π^* resonance in the top panel (suppressed in *s-pol*) implies that benzene lies flat on the Ag(110) surface.

1.2.3 Resonant Photoemission Spectroscopy

Resonant photoemission spectroscopy (RPES) combines the advantages of XPS and NEXAFS into a single measurement technique. It is similar to the NEXAFS technique in that a variable photon energy source is used, except that instead of counting total electron yield using an electron multiplier tube, an electron analyzer (similar to XPS) is used to measure the intensity of electron emission as a function of kinetic energy. Another way to see this measurement is as a series of XPS scans at each point of a NEXAFS scan.

A schematic of this process is shown in Figure 1.9c-f. The depicted scheme in Figure 1.9c is a carbon K-edge transition, where a photon of \sim 284 eV energy interacts with a carbon atom, resulting in a C1s \rightarrow LUMO transition. This excited state then decays through a variety of radiative and non-radiative decay channels. We focus on non-radiative Auger electron decay processes, two of which are shown in Figure 1.9d and e.

At the incident photon energy corresponding to the C1s \rightarrow LUMO transition, certain Auger electrons exiting from the K-edge absorption processes (such as Figure 1.9d-e) have the same kinetic energy as directly photoemitted valence band photoelectrons (Figure 1.9b). Since these are coherent processes, they can interfere constructively to provide a large enhancement in the photoemission signal[33, 34, 35]. This enhanced photoemission signal allows the accurate determination of the occupied orbitals involved in Auger transitions and the orbital energies of valence levels.

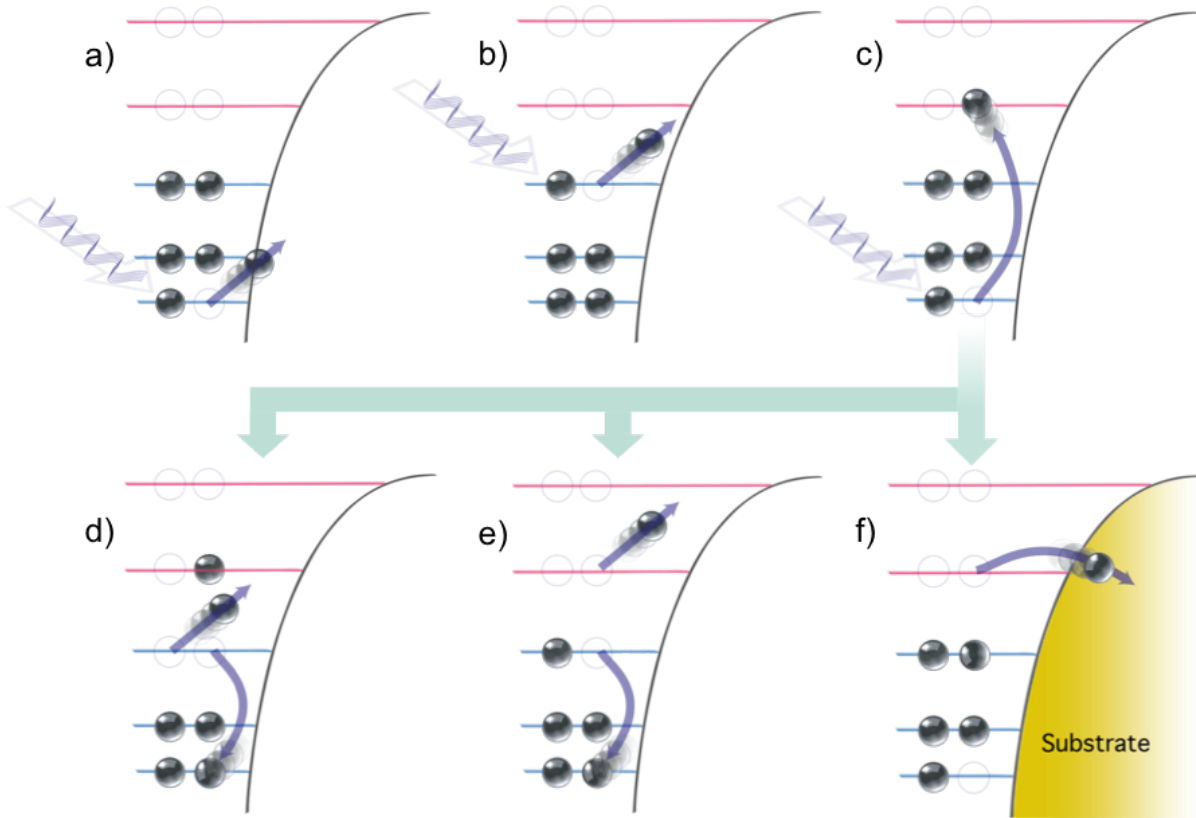


Figure 1.9 – Schematic representation of various photoexcitation processes.

Adapted from Reference [36] **a** X-Ray Photoemission (XPS), involving direct photoemission processes from core atomic levels **b** Valence Band (VB) photoemission **c** X-ray absorption induced transition from Core Level to Lowest Unoccupied Level. From c), three possible core-hole decay paths are shown, **d** Resonant Auger or Spectator decay, **e** Resonant Photoemission or Participator Decay, and **f** Delocalization of excited electron to the conduction band of an Au substrate coupled to the molecule.

An additional non-radiative decay channel is available for molecules that interact with their environments, e.g. molecules deposited on metal substrates (Figure 1.9f). Here, the electron excited into LUMO escapes into the unoccupied continuum states of the metal. If this electron escape occurs within the lifetime of the core-hole, participator Auger yield is reduced. Therefore, the differences in Auger electron yield between molecules on metal (coupled systems allowing electron escape) and isolated molecules (decoupled system) can be used to determine the probability of electron escape, and thus a 'charge transfer time'

between molecule and metal. This method is called the *core-hole clock* implementation of RPES (see [35] for an excellent review).

1.2.4 Outline

This thesis is divided into four chapters, with the first being an introduction and background materials. Chapter 2 focuses on the study of organic molecules that couple to metal electrodes via weak ‘through-space’ interactions. Section 2.1 focuses on an X-Ray spectroscopy study of the role of intra-molecular coupling on through-space charge transfer. Section 2.2 builds on this understanding by using through-space coupling to enable rectification in single-molecule junctions at high biases. Chapter 3 discusses the electronic properties of the gold-carbon bond, a strongly coupled covalent bond formed using molecules containing trimethyltin leaving groups. Section 3.1 presents a study that uses synchrotron spectroscopies to provide the first evidence for the formation of this bond, and show that the chemical and electronic nature of this bond is dependent on the reactivity of the underlying gold surface. Section 3.2 describes results from STM studies on molecular junctions containing gold-carbon bonds, which show that the presence of these strongly-coupled bonds results in unique high-bias conductance properties. Finally, Chapter 4 addresses the problem of molecular self-assembly. This chapter probes the self-assembly of anthracene-based molecules into graphene nanoribbons on gold surfaces through dehalogenation and subsequent polymerization, and describes the interaction between the self-assembled structures and the underlying gold substrate.

Chapter 2

Through-Space Interactions

2.1 Quantifying Through-Space Charge Transfer Dynamics in π -Coupled Molecular Systems

2.1.1 Preface

This chapter is based on a manuscript entitled *Quantifying Through-Space Charge Transfer Dynamics in π -Coupled Molecular Systems*, by Arunabh Batra[†], Gregor Kladnik[†], Héctor Vázquez, Jeffrey S. Meisner, Luca Floreano, Colin Nuckolls, Dean Cvetko, Alberto Morgante and Latha Venkataraman published in *Nature Communications*[36] ([†] equal contributors). The experimental work was conducted at the ALOISA Beamline at the Elettra Synchrotron in Trieste, Italy, in collaboration with Dr. Gregor Kladnik, Dr. Luca Floreano, Prof. Dean Cvetko, and Prof. Alberto Morgante. Chemical synthesis was performed by Dr. Jeffrey S. Meisner from Prof. Colin Nuckolls' group. Theoretical work was conducted in collaboration with Dr. Héctor Vázquez in Prof. Latha Venkataraman's group.

2.1.2 Abstract

Understanding the role of inter-molecular interaction on through-space charge transfer characteristics in π -stacked molecular systems is central to the rational design of electronic materials. However, a quantitative study of charge transfer in such systems is often difficult due to poor control over molecular morphology. Here, we use the core-hole clock implementation of resonant photoemission spectroscopy to study the femtosecond charge-transfer dynamics in cyclophanes, which consist of two precisely stacked π -systems held together by aliphatic chains. We study two such systems, [2,2]paracyclophe (22PCP) and [4,4]paracyclophane (44PCP), with inter-ring separations of 3.0 Å and 4.0 Å respectively, and find that charge transfer across the π -coupled system of 44PCP is 20 times slower than in 22PCP. We attribute this difference to the much poorer inter-ring coupling in 44PCP, and show the adequacy of the core-hole clock method as a general tool for quantifying through-space coupling in π -stacked systems.

2.1.3 Introduction

Electron transport in conjugated molecules can broadly be characterized as through-space or through-bond in character[37]. Through-space transport is central to many applications of π -stacked systems, such as organic electronics and photovoltaics[38, 39], DNA molecular wires[40], redox active biocomplexes[41], and multilayer graphene devices[42]. Such π -stacked systems are also relevant to single-molecule electronics. For example, strained paracyclophanes have been shown to behave as molecular ‘linkers’ to connect molecules to metal electrodes in single-molecule circuits[43]. Cyclophanes have also led to a new wave of research into molecular non-linear optical phenomena in donor-acceptor complexes[44]. In the case of organic photovoltaics and light emitting devices, optimizing the π -stacking of conjugated molecules is essential to tuning transport properties and exciton lifetimes[45, 46].

Most studies in this field have focused on optimizing bulk device characteristics by altering molecular substituents[47], post-growth annealing[48, 49], or other processing steps[50], or have used scanning tunneling microscopy and spectroscopy to measure charge transport across multilayer stacks of conjugated molecules[51]. However, these studies have not provided direct information on charge-delocalization dynamics in these coupled π - systems. Here, we make use of X-ray photoemission spectroscopy (XPS), near-edge X-ray absorption fine-structure spectroscopy (NEXAFS), and the resonant photoemission spectroscopy (RPES) core-hole clock (CHC) method[35, 52, 53, 54], illustrated in Figure 2.1, to characterize π - π interaction in conjugated, stacked systems. Core-hole clock spectroscopy has previously been used to measure femtosecond charge-transfer times between molecule-metal interfaces like C60[35, 55], aromatic thiols[56, 57], amines[58] and donor-acceptor complexes[59] on Au(111).

We now apply this technique to quantifying through-space charge transfer from two paracyclophane molecules with distinct intra-molecular π -couplings, to underlying Au(111) substrates. The basic premise of the core-hole clock method is summarized in Figure 2.1c-f:. Synchrotron radiation is used to induce the transition of a carbon 1s electron to the lowest unoccupied molecular orbital (LUMO) (Figure 2.1c), generating an excited electron in the LUMO and a core-hole in the 1s level. In an isolated molecule such an excited state can decay via one of two processes: resonant photoelectron decay, also known as participant decay (Figure 2.1d), or a resonant auger decay, also known as spectator decay (Figure 2.1e). In either case, a measurable photoelectron intensity results. However, if the molecule is placed on a metal substrate with the LUMO strongly hybridized with the metal substrate's wavefunctions (Figure 2.1f), there is a high probability for the excited electron to delocalize into the continuum electronic states of the metal within the lifetime of the core-hole. In this case, both spectator and participant processes are strongly

quenched, yielding low or almost no photoelectron intensity. By comparing the intensities of these processes between monolayer and multilayer films of the molecules, it is possible to determine a quenching ratio for each molecular system (see Methods for details). This quenching can be directly related with the delocalization time for the originally excited electron, with strong quenching representing fast delocalization (and vice versa).

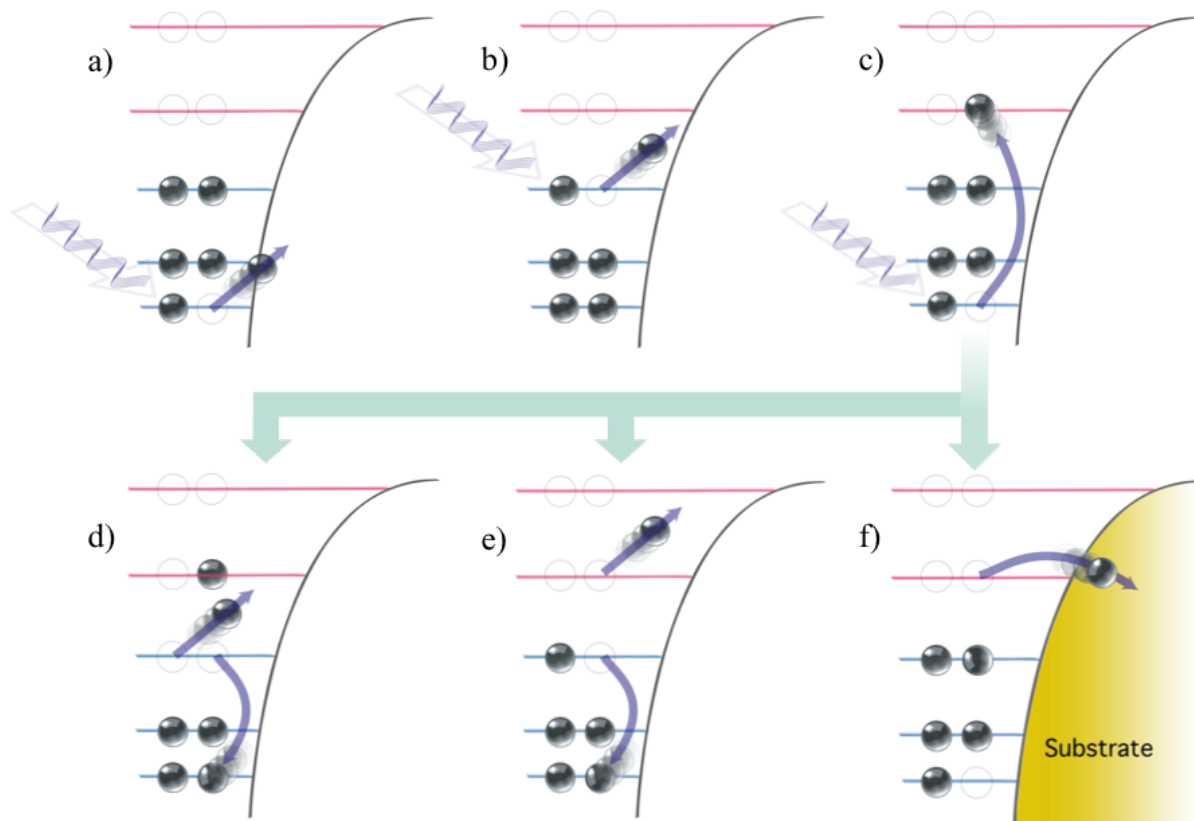


Figure 2.1 – Schematic representation of different photoexcitation processes
a Direct photoemission from core level (XPS) **b** Direct photoemission from occupied valence states (VB). **c** X-ray absorption induced transition from core level to lowest unoccupied level; from this excited state, three possible decay paths are shown. **d** Resonant Auger or spectator decay, **e** Resonant photoemission or participator decay, and **f** Delocalization of excited electron to the unoccupied electronic states of an Au substrate coupled to the molecule.

In this work, we probe the relation between charge transfer dynamics and π - π coupling by comparing two molecules, [2,2]paracyclophane (**22PCP**) and [4,4]paracyclophane

(**44PCP**) adsorbed on Au(111) (see Figure 2.2 for structures). **22PCP** and **44PCP** can be represented as two benzene rings joined together as eclipsed ‘bilayers’ using a scaffold of two or four aliphatic carbon chains respectively. **22PCP** is a strained system with an average inter-ring distance of 3.0 Å, while **44PCP** has an inter-ring separation of 4.0 Å[60]. By comparing these two ‘bilayer like’ systems with well-defined, but dissimilar inter-ring distances, we are able to study the effect of inter-ring coupling on through-space charge transport in π -stacked systems[61, 37].

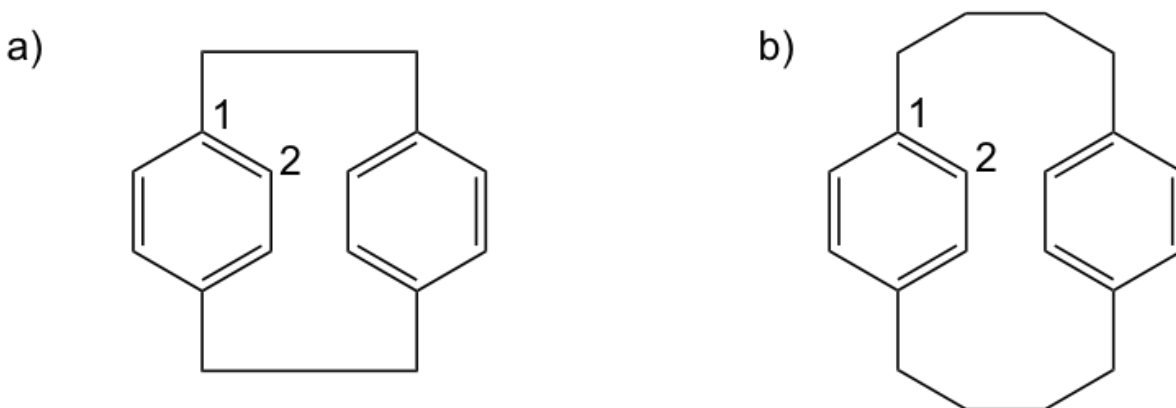


Figure 2.2 – Chemical Structures
Chemical structures for **a** [2,2]Paracyclophane (**22PCP**) and **b** [4,4]Paracyclophane (**44PCP**)

We find that, despite their very similar interaction with Au(111), resonant photoemission processes are significantly more quenched in monolayers of **22PCP** than in those of **44PCP**, indicating a much faster delocalization from **22PCP**. We develop a model to convert these quenching ratios to charge-transfer times, and are able to distinguish charge transfer from individual rings of each molecule. We find that the charge transfer time across the π -system of **44PCP** is about 20 times slower than across that of **22PCP**, and attribute this longer charge transfer time to poor through-space coupling between the

rings of the molecule. These measurements allow us to quantitatively probe the relation between π - π coupling and charge transfer.

2.1.4 Results

2.1.4.1 Comparison of Monolayer Films

We first use XPS, NEXAFS, and first-principles density function theory (DFT) calculations to establish that our two systems, **22PCP**//Au(111) and **44PCP**//Au(111), have similar adsorption configurations, molecule-metal adsorption energies and molecule-metal adsorption distances.

Figure 2.3a and 2.3b show XPS spectra for monolayer and multilayer films of **22PCP** and **44PCP**. Both molecules show a systematic shift of the C1s peak towards higher binding energy with increasing coverage, as expected due to core-hole screening by the substrate image charge[62, 63]. We note that both monolayers show the same screening-induced shift to lower binding energy by 0.4 eV relative to the multilayer phase. The C1s peaks for both molecules display similarly broad and asymmetric shapes due to initial state differences between the sp^2 C and sp^3 C atoms in the molecules[64]. The similarity in XPS peak positions, shapes, and screening-induced shifts for both molecules suggests that there is no large difference in the adsorption energies of the two systems. Temperature desorption spectroscopy shows that both **22PCP** and **44PCP** monolayers desorb at temperatures between 400K-420K, also indicating similar adsorption energies to the Au(111) surface. These experimental findings are corroborated by DFT calculations for a model system (see Supplementary Information, Calculation Details Section), which show that the adsorption energies of **22PCP** and **44PCP** to an Au-dimer are similar (0.72 eV and 0.61 eV respectively) in agreement with previously published results⁷. The optimized adsorption geometries for the dimer-molecule systems are also similar; **22PCP**

is bound to the dimer at the 1 position, (Figure 2.2), with a minimum Au-C bond length of 2.44 Å while **44PCP** is bound between the 1 and 2 positions, with a minimum Au-C bond distance of 2.48 Å. These calculations do not reflect the true adsorption energies of these molecules to a Au(111) surface, but do show that no significant difference in the adsorption of **22PCP** and **44PCP** should be expected.

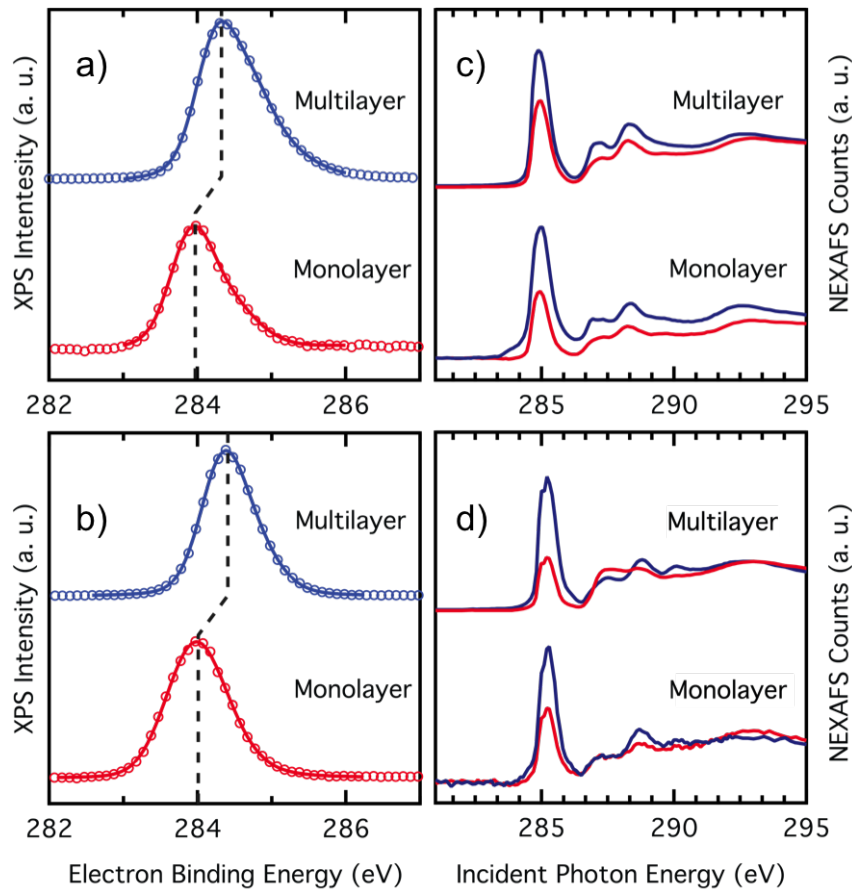


Figure 2.3 – Comparison of XPS and NEXAFS Spectra

a Multilayer (Blue) and Monolayer (Red) XPS spectra for C1s for **22PCP** and **b) 44PCP**, respectively. Solid lines are fits to data (open circles). **c** Carbon K-edge NEXAFS measurements for **22PCP** and **d) 44PCP**. Measurements for multilayer and monolayer depositions are shown. The blue (red) curve represents incident E-field polarized perpendicular (parallel) to the Au(111) surface.

In order to isolate the effect of inter-ring coupling on charge transfer, it is important to ensure that **22PCP** and **44PCP** monolayers have similar morphologies on the Au(111)

surface. To determine molecular orientation, we carried out NEXAFS dichroism[65] studies on the two systems. Figure 2.3c and 2.3d show the partial electron yield spectrum collected from the C K-edge of the two samples. To assign peaks, we compared experimental data to simulated NEXAFS spectra using the half-core-hole approximation, following Nilsson et al[66]. We find that the sharp feature at 285 eV is comprised of a doublet, attributed to $\text{C}1\text{s} \rightarrow \pi^*$ transitions localized on inequivalent carbon atoms on the benzene rings. The intensity of this peak depends on the orientation of the π^* orbital (and thus the benzene rings) relative to the polarization of incident light. We determine an average tilt angle for the benzene rings with respect to the surface by comparing the ratio of intensities of the peak with incident electric field perpendicular (p-pol) to the sample and parallel (s-pol) to the sample[65]. We find that the average tilt angle for the molecular aromatic rings with respect to the Au(111) surface in monolayer films is $47^\circ \pm 5^\circ$ for **22PCP** and $45^\circ \pm 5^\circ$ for **44PCP**. This angle is consistent with binding near the 1 or 2 carbon positions on the ring and indicates comparable adsorption geometries for both monolayers.

2.1.4.2 Resonant Photoemission Measurements

Having established the adsorption characteristics, we now analyze the charge-transfer characteristics of the two systems. We measure RPES spectra, which comprised of XPS measurements taken at a series of incident photon energies across the carbon K absorption edge, on multilayer and monolayer phases of both molecules. Two-dimensional photon-energy versus electron binding energy RPES maps are shown in Figure 2.4. These spectra have been normalized for total Auger intensity. Direct photoemission and Auger electron emission have been subtracted from the RPES images (see Supplementary Information RPES Analysis Procedure Section), leaving only the photoemission from participator decay. In this figure, we present the region between 284 and 286 eV in photon energy, which contains resonant excitations from C1s to the LUMO and LUMO+1 for both molecules.

In both monolayer and multilayer RPES images, high intensity bands corresponding to these orbital energies are clearly visible.

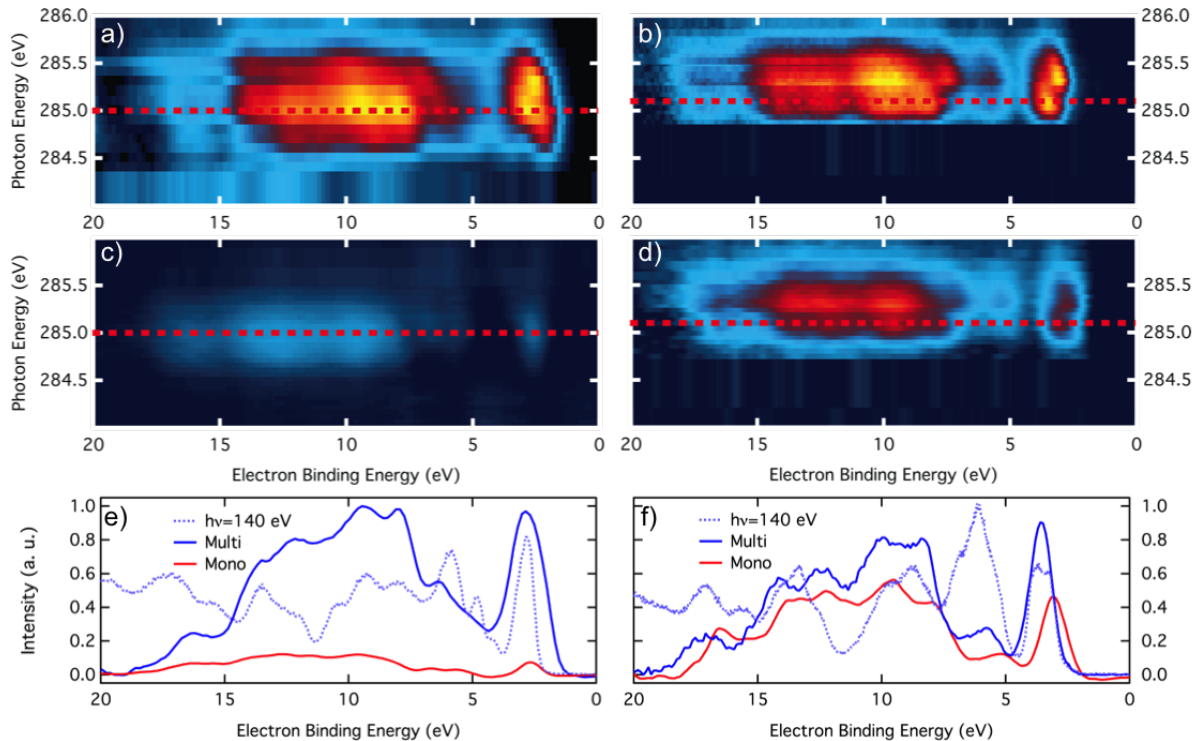


Figure 2.4 – Resonant Photoemission (RPES) Intensity Maps

Resonant Photoemission (RPES) intensity map of LUMO and LUMO+1 resonances of **a-b** Multilayers of **22PCP** and **44PCP**, and **c-d** Monolayers of **22PCP** and **44PCP** respectively. The dashed red lines represent the positions of the LUMO, at 285.0 eV and 285.1 eV for **22PCP** and **44PCP** respectively. **e-f:** Line profiles of LUMO resonances for monolayer and multilayer **22PCP** and **44PCP**, with Valence Band (140 eV incident light) spectra of multilayers for comparison. The intensities of both Valence Band spectra have been scaled for clarity.

Line profiles of the resonant photoemission from the LUMO of **22PCP** (285.0 eV) in the multilayer and monolayer phases are taken along the dashed lines in Figure 2.4a and b, and are plotted in Figure 2.4c together with the multilayer valence band (VB) photoemission spectrum for **44PCP** taken separately with a photon energy of 140 eV.

Similar profiles are taken for the LUMO of **44PCP** (285.1 eV) in Figure 2.4d and e, and plotted in Figure 2.4f with its VB spectrum. The VB spectra show direct photoemission from the occupied molecular orbitals of each molecule. Each resonant peak in the RPES line profiles corresponds with a peak in the VB spectrum, and thus represents a participator decay process involving distinct occupied-unoccupied orbital pair. It is evident from Figure 2.4b and e that the RPES intensity for both molecular monolayers is reduced when compared with the intensity from the corresponding multilayer phases. This decrease in intensity is due to electron transfer from the LUMO to the substrate on a time scale that is comparable to the lifetime of the core-hole. The ratio of integrated intensity between monolayer and multilayer films gives us an average quenching ratio, $\langle q \rangle$ for each molecular system. For **22PCP**, this average quenching ratio $\langle q_{22} \rangle$ is found to be 0.19 ± 0.02 , while for **44PCP** $\langle q_{44} \rangle$ is 0.50 ± 0.02 , indicating that participator processes in the **22PCP** monolayer are strongly suppressed compared to the **44PCP** monolayer.

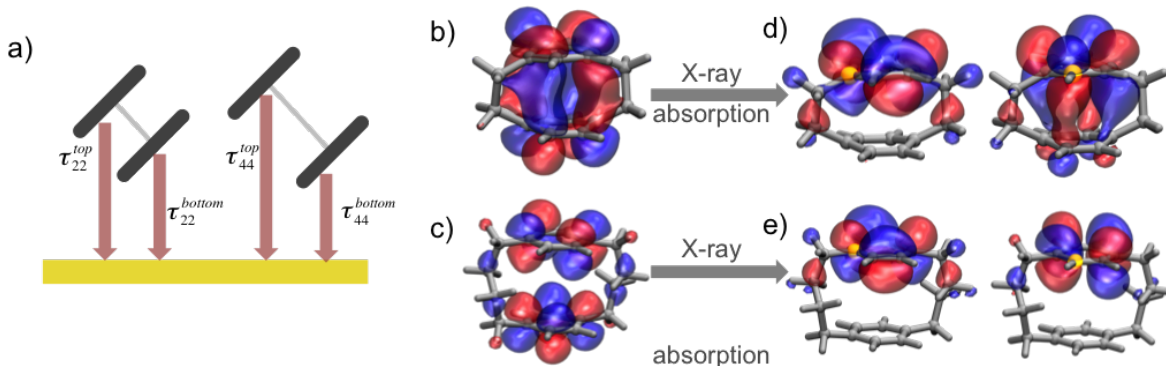


Figure 2.5 – The Charge Transfer Model

a A schematic of the charge transfer times calculated by the model. **b** Isosurfaces for LUMO for molecules in the ground state (left) and core-hole excited states for **22PCP** and **c** **44PCP**. Core-hole excitations on the two inequivalent carbons in the rings (positions 1 and 2 in Figure 2.2) are indicated in yellow. Isosurface values for all plots are set to $0.06 |e|/\text{\AA}^3$

As we have shown, the large difference in quenching between **22PCP** and **44PCP** occurs despite the very similar adsorption characteristics of both molecules on Au(111). While these quenching ratios suggest that molecule-metal charge transfer from **22PCP** is much faster than in **44PCP**, we can further quantify the efficiency of charge-transfer in each of these π -systems using a model to convert quenching ratios into charge-transfer times. Using our model, we find that the observed differences in through-space charge-transfer between the two molecular systems are a direct consequence of π - π interaction within the molecule.

2.1.4.3 Determining Charge Transfer Times

We convert the quenching ratios determined above to overall charge transfer times τ_{CT} using equation 2.1 below, following the method outlined by Bruhwiler et al.[35]:

$$\tau_{CT} = \tau_{CH} \frac{I_{coupled}}{I_{isolated} - I_{coupled}} \quad (2.1)$$

Here, $\tau_{CH} = 6$ fs is the core-hole lifetime of C1s, $I_{isolated}$ is the integrated participator intensity from resonant HOMOs for an isolated molecular system (as approximated by the multilayer), and $I_{coupled}$ is the corresponding intensity for a monolayer film coupled to Au(111). If we simply assume all aromatic carbon atoms in each molecular system to be equally coupled to the substrate (and thus equally quenched), we can calculate an average charge transfer time for each molecular monolayer, $\langle\tau_{22}\rangle = 1.4 \pm 0.5$ fs and $\langle\tau_{44}\rangle = 6.0 \pm 0.6$ fs, for **22PCP** and **44PCP** respectively. Within this approximation, our results are consistent with those reported in literature for aromatic molecules adsorbed on metallic substrates. For example, our value of $\langle\tau_{44}\rangle = 6$ fs for **44PCP**//Au(111) is the same as that reported for C60 on Au (110)[67]. Similarly, $\langle\tau_{22}\rangle = 1.4$ fs is within the upper bounds reported for charge transfer times from small, planar aromatics, e.g. <3 fs

for tetracene on HOPG(0 0 0 1)[62].

These differences in average charge transfer times provide clues into the relation between through-space charge transfer and inter-ring coupling. But given the symmetries in our system, we are able to go beyond this simple approximation, and calculate individual charge transfer times for the top (further from substrate) and bottom (closer to substrate) rings of these molecules (Figure 2.5a). We first consider the processes involved during photoemission. Since a charge from the C1s core is transferred to the LUMO of the molecule, we compare the calculated LUMOs for both systems with and without a core-hole present. We see, in Figure 2.5b and c, that the ground state LUMO for both molecules is delocalized over both top and bottom rings. However, when a ring atom C1s→LUMO transition occurs, the partially occupied LUMO localizes strongly near the core-hole on the same ring (Figure 2.5d, e).[63] It is therefore evident that molecule-to-metal charge transfer will depend strongly on the site of the core-hole, and excitations in the top ring of a molecule will likely result in slower molecule-to-metal charge transfer than excitations in the bottom ring. Furthermore, comparing Figure 2.5d and 2.5e, we find that the LUMO in the excited state of **44PCP** is much more confined to one ring, which hinders through-space coupling significantly. This comparatively weaker inter-ring coupling in **44PCP** results in the lower charge transfer rate we observe. We also note that Figures 2.5d and e show that the core-hole does not significantly destroy the conjugation within a single aromatic ring. Thus, electronic excitations from any core-site on a ring would delocalize very quickly across the LUMO, which is spread across the whole ring. We assume the timescale for this delocalization to be much faster than that of electron delocalization from one ring to another. Thus, the major contribution to differences in charge delocalization is electronic density in between the rings and not differences within a single ring.

To model the charge transfer in these systems, we note that the top and bottom rings

of the molecules are simultaneously illuminated, and core-holes can be excited in either ring. Since we have established that monolayers for **44PCP** and **22PCP** have similar adsorption geometry, for the rest of this analysis, we assume that the bottom rings of both molecules couple equivalently to the substrate. Therefore, the difference in charge transfer between these two molecules is due to photoexcitation in the inequivalent top rings, where excited electrons must couple across the inter-ring region to delocalize to the substrate.

To quantify the above analysis, we develop a one-parameter model for charge transfer times from top and bottom rings of both monolayers to the substrate (see Methods). Our model assumes that 1) charge transfer times from the bottom rings both **22PCP** and **44PCP** monolayers are equivalent, and 2) charge transfer times from the bottom rings must be at least as fast as the top rings. With this, we find that the molecule-to-metal charge transfer from the bottom rings of both molecular monolayers is $\tau_{bottom} = 0.7 \pm 0.3$ fs while that from the top ring of **22PCP** is $\tau_{22}^{top} = 2.3 \pm 0.6$ fs. We also find that the charge transfer time from the top ring of **44PCP**, i.e. $\tau_{44}^{top} \geq 50$ fs. An upper bound for τ_{44}^{top} would be beyond the experimental limitations of the core-hole clock technique (~ 10 times the core-hole lifetime). Our model shows that charge transfer from the top ring of **22PCP** is ~ 20 times faster than that from **44PCP**.

We can now compare this measured charge transfer rate difference to the inter-ring coupling in these systems. The molecular orbitals of these compounds can be approximated as bonding and antibonding linear combinations of the molecular orbitals of each individual ring (analogous to a xylene). The energy splitting between the bonding and antibonding combinations provides a measure of the electronic coupling between the two rings in the ground state. Focusing on the LUMO orbitals, we see that this energy splitting is 1.3 eV for **22PCP**, compared with 0.21 eV for **44PCP** (see Supplementary Figure 2.6). Since the charge transfer rate is proportional to the square of this energy splitting[64], we would

predict the inter-ring electron transfer rate for **22PCP** to be \sim 40 times higher than that for **44PCP**, which is quite close to our experimental result given that we do not include the effect of the underlying substrate or that of the core-hole in calculating the coupling.

2.1.5 Conclusion

In conclusion, we have determined three distinct charge transfer regimes in paracyclophanes: τ_{bottom} in the sub-fs regime, τ_{22}^{top} in the 1-2 fs regime, and an extremely long $\tau_{44}^{top} \geq 50$ fs, at the experimental limit of the core-hole clock technique. These results present the first measure of through-space charge-transfer time as function of inter-ring distance in a π -stacked system. By our choice of molecules and our experimental and theoretical analysis, we are able to quantitatively relate these charge-transfer times to π - π coupling by controlling both inter-ring distance (and hence coupling) and the interaction of molecule to metal. We consider our methods and results with cyclophanes to be generalizable to many other π -stacked materials. Further, such RPES studies would not be limited to monolayer films, but could also be used to probe inter-molecular charge transfer in π -stacked thick films.

2.1.6 Methods

2.1.6.1 Experimental Methods

Our experiments were conducted on the ALOISA/HASPES beamline at the Elettra Synchrotron in Trieste, Italy[65, 68, 66]. The Au(111) substrate was first cleaned using a 1 keV beam of Ar1+ from a sputtering source, followed by a rapid anneal to 900K. Reflection high energy electron diffraction (RHEED) was then used to confirm the characteristic herringbone reconstruction of Au(111). XPS measurements were made to ensure no contamination on the sample. The operational pressure for the measurement chamber was

maintained at 10-11 mbar and the sample preparation chamber at 10^{-10} mbar.

Both **22PCP** and **44PCP** were obtained in powder form from Sigma-Aldrich (>97% purity) and used without further purification. Deposition techniques for both molecules were similar. The molecule was placed in a valved, quartz Knudsen-type cell in line-of-sight with the sample preparation chamber. For monolayer deposition, the Au(111) substrate was maintained at room temperature, and the Knudsen cell was heated to 340K. The molecules were deposited at a chamber pressure of 10-8 mbar for 3 minutes. Maintaining the substrate at room temperature during deposition resulted in a monolayer film for both compounds, as determined by Helium angle scattering (HAS) and XPS measurements. After the chamber recovered to base pressure, the sample was cooled to 230K before exposure to synchrotron radiation to avoid beam-induced damage. For multilayer deposition, the substrate was first cooled to 230K, and molecules were deposited at 10-8 mbar for 5 minutes. Multilayer films created this way were at least 2 nm thick. After each deposition, XPS spectra of Oxygen 1s and Nitrogen 1s were checked to ensure no contamination. The films were then characterized using XPS, valence band spectroscopy, and NEXAFS, before conducting RPES measurements.

For XPS measurements (Figure 2.3a and b), X-rays with electric field perpendicular to the sample (p-pol) of energy 400 eV (**22PCP**) and 500 eV (**44PCP**) was used at grazing-incidence (4°) to the sample. Photoelectrons were collected normal to the sample using a hemispherical electron analyzer with an acceptance angle of 1° . The energy scale for XPS spectra was calibrated by aligning the Au $4f_{7/2}$ peak to a binding energy of 84 eV. Valence band measurements were also carried out under similar beam conditions, except at an incident energy of 140 eV.

NEXAFS measurements were conducted on the C K-edge, with incident photon energy between 280 eV and 295 eV, and incidence angle of 6° . Spectra were acquired in partial

electron yield mode, with a high pass filter set to 250eV, and normalized to the beam current measured on the last aperture of the beam path. The spectra were collected with electric field polarization parallel to the sample (s-pol) and perpendicular (p-pol) to the sample (Figure 2.3c and 2.3d).

Resonant photoemission (RPES) was conducted by taking XPS scans at a series of incident photon energies between 280 eV and 295 eV. The sample was moved to a new position after each XPS measurement to ensure that the entire RPES spectrum was taken on a fresh sample. For all RPES measurements presented in this study, incident light was polarized at 54.7° with respect to the surface normal, which resulted in a RPES signal independent of molecular orientation[68]. The electron analyzer for RPES was placed at 54.7° from the surface normal and along the photon electric field.

2.1.6.2 Charge Transfer Model

Charge transfer times from the top rings of both **22PCP** and **44PCP** monolayers are determined using a one-parameter model assuming that the bottom rings of both monolayers couple equivalently to the underlying substrate. This assumption is validated by our experimental results which find similar adsorption energies and geometries of both monolayers on Au(111). The molecule-to-metal charge transfer time for the bottom rings is thus taken to be equal:

$$\tau_{22}^{bottom} \approx \tau_{44}^{bottom} \equiv \tau^{bottom} \quad (2.2)$$

To apply Equation 2.1, we must also know the participator intensity contributions from top and bottom rings of the monolayers without charge transfer processes. The top and bottom rings should each contribute half of the measured participator intensity, $I_{isolated}^{mono}$. However, electrons emitted from the bottom ring can scatter inelastically from the top ring, decreasing the effective contribution from the bottom ring to 0.475 (see Supplementary

Information Charge-transfer model section). Applying Equation 2.2 we get:

$$\tau^{bottom} = \tau_{CH} \frac{\langle I_{coupled}^{bottom} \rangle}{\langle I_{isolated}^{bottom} - I_{coupled}^{bottom} \rangle} = \tau_{CH} \frac{q^{bottom}}{0.475 - q^{bottom}} \quad (2.3)$$

where $I_{coupled}^{bottom}$ is the participator intensity for a coupled monolayer due to the bottom ring, $I_{isolated}^{bottom}$ is the corresponding intensity for an uncoupled monolayer, and

$$q^{bottom} = \frac{\langle I_{coupled}^{bottom} \rangle}{\langle I_{isolated}^{mono} \rangle}$$

is the quenching ratio due to charge transfer from the bottom ring to the substrate. A similar procedure is applied to calculate τ_{22}^{top} and τ_{44}^{top} , the charge transfer times from the top rings of **22PCP** and **44PCP**:

$$\tau_{22}^{top} = \tau_{CH} \frac{\langle q_{22} \rangle - q^{bottom}}{.525 - (\langle q_{22} \rangle - q^{bottom})} \quad (2.4)$$

$$\tau_{44}^{top} = \tau_{CH} \frac{\langle q_{44} \rangle - q^{bottom}}{.525 - (\langle q_{44} \rangle - q^{bottom})} \quad (2.5)$$

where $\langle q_{22} \rangle$ and $\langle q_{44} \rangle$ are the average quenching ratios for **22PCP** and **44PCP** (as defined in the Results section). The only free parameter within this model is q^{bottom} , the quenching due to charge transfer from the bottom ring to the substrate. We establish bounds for this value by noting that $0 < \tau^{bottom} \leq \tau_{22}^{top}, \tau_{44}^{top}$, i.e. that charge transfer from the bottom ring must be faster than from the top rings.

2.1.6.3 Supplementary Information

Details of Resonant Photoemission Spectroscopy Measurement For resonant photoemission (RPES) measurements, the incident photon energy was scanned across the carbon 1s absorption edge with a photon energy step of 0.1 eV. For each photon energy, a

90 eV photoemission spectrum was measured. This measurement window contained the whole valence band spectrum as well as the Au 4f_{5/2} and Au 4f_{7/2} peaks which served to calibrate the binding energy. During this measurement, the electron current due to X-ray absorption on the last mirror of the beamline optical system was measured. This current signal was used for initial photon energy calibration and intensity normalization. The measurements were performed in magic angle conditions, i.e. the polarization as well as the electron analyzer were at 54.7° with respect to the sample normal, thus yielding a signal independent of the molecular orientation on the sample.

The RPES spectra were first normalized to the separately measured absorption on a clean Au(111) substrate. Next, all valence band (VB) scans were aligned using the Au 4f photoemission peaks, which yielded the final correction to the photon energy calibration. The binding energy of the Au 4f_{7/2} peaks in each scan was set to 84 eV. For both types of films, monolayer and multilayer, we used the second-order light C1s peak in RPES to perform a further correction for any charging effects. The non-resonant signal was measured in the pre-edge region at $h\nu=283$ eV and subtracted from each scan in the 2D RPES map.

To separate the different core-hole decay channels, we first measured the normal Auger peak shape at higher photon energy far above the edge at $h\nu=310$ eV. The subtraction of the Auger peak signal was done in the kinetic energy scale. For each photon energy, the intensity (multiplicative factor) and possible spectator shift of the Auger peak was assessed. With a best fit procedure, the Auger peak intensity and energy shift due to spectator electron was obtained, and was further subtracted from the spectra to leave only the resonant photoemission intensity (participator intensity). The intensity of the subtracted Auger signal closely resembles the NEXAFS intensity throughout the absorption edge, and spectator energy shifts of the order of 2-4 eV were found for photon energies between

284-288 eV (i.e below the ionization edge). This non-resonant and Auger subtraction procedure was employed to the monolayer as well as multilayer RPES data. The intensity of the RPES was further normalized to the overall intensity (Auger + participator).

The core hole clock method was then used to determine the charge transfer times in monolayer systems. In a well-coupled molecule-metal system, charge transfer (CT) to the substrate suppresses the resonant photoemission signal. The intensity of the suppressed signal, obtained from the RPES map is then compared to the reference multilayer signal intensity where we assume no CT channel is available, i.e. the RPES signal is unquenched. Before measuring the quenching of the RPES signal, the monolayer data has to be normalized to the multilayer (for the coverage, photon illumination due to absorption etc.). Here we assume that, for each photon energy scan, the probability of core-hole decay should be 1. This means that the sum of all decay channels (i.e. total integrated intensity) should be equal for both mono- and multilayer systems. The charge transfer time is then determined using Equation 2.1 in the main text.

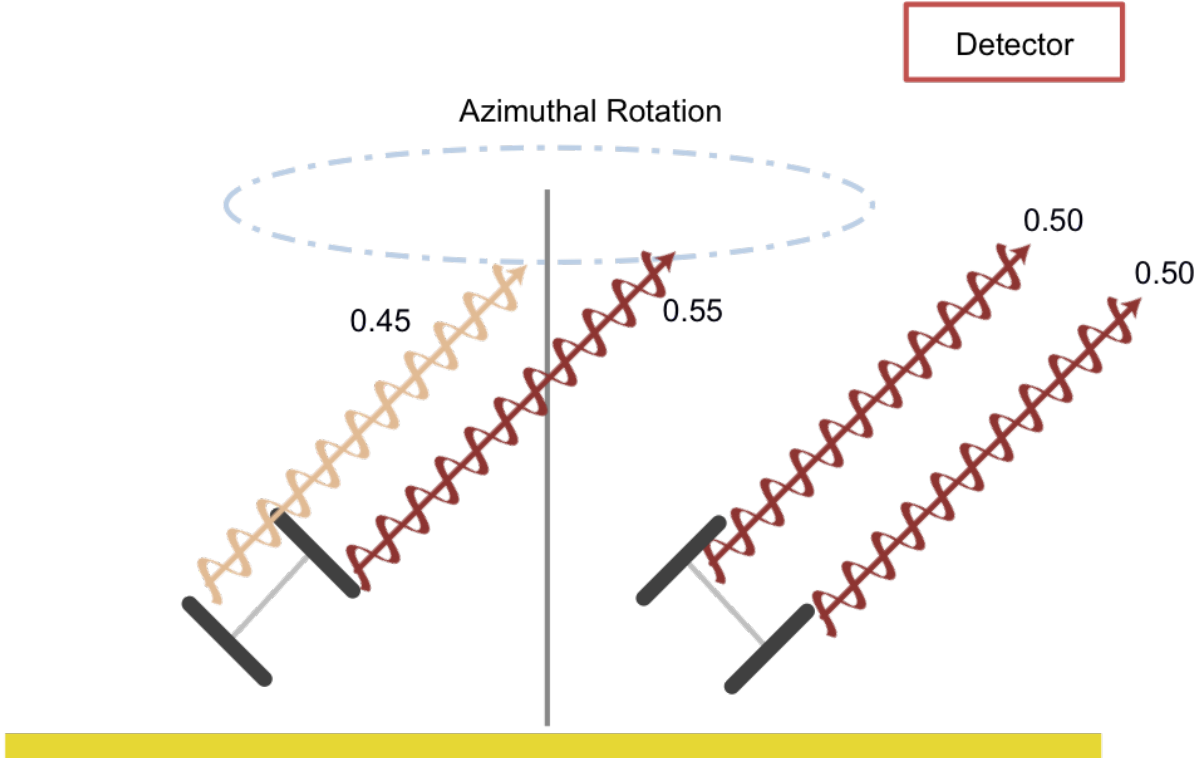


Figure 2.6 – Effect of Azimuthal orientation on shadowing

The molecular orientation on the right corresponds to no shadowing, and thus equal contribution of top and bottom rings (0.5) to total intensity (1.0). The molecule on the left shows the case of maximum shadowing of the bottom ring, resulting in a higher contribution from the top ring (0.55) than the bottom (0.45).

Charge Transfer Model We measure the CT dynamics from the LUMO, which is, according to our DFT ground state calculations, distributed across the benzene rings of both molecules. The probability to create a core-hole on either ring is thus equal to $1/2$. It is however important to note that the signal coming from the lower ring is shadowed by the upper ring due to inelastic electron scattering. We use the measured attenuation of the Au 4f electrons that pass through the entire paracyclophane monolayer as a reference and scale it by half of the layer thickness to obtain the signal attenuation from the inner ring[69]. We find for the Au4f peak an attenuation of $\sim 40\%$ in a monolayer, which yields an attenuation of $\sim 20\%$ for the signal coming from the lower ring. We further note that our

electron detector is placed at 54° from the surface normal, and that the paracyclophane molecules adsorb with a tilt angle of 45° evenly around the surface normal. This indicates that not all paracyclophane molecules adopt a geometry in which the upper ring attenuates the signal from the lower ring.

Figure 2.6 illustrates two extreme orientations where the shadowing effects are either zero or maximal. The orientation shown on the left results in a maximal intensity difference due to shadowing with $I_{upper} = 0.55$ and $I_{lower} = 0.45$) while the one on the right has equal contribution from both rings with $I_{upper} = I_{lower} = 0.5$. In this latter case we consider that regardless of the azimuthal orientation, the entire molecular film thickness d equally attenuates the Au signal beneath $\exp(-\frac{d}{\lambda}) = 0.65$, λ being the elastic mean free path of electrons[69]). Therefore, the signal from the molecules in the right hand side of Figure 2.6 is thus equally attenuated by $\exp(-\frac{d}{\lambda}) = 0.8$ for both, lower and upper ring. By averaging over all molecular orientations, the ratio of the signal from the upper and lower rings is 0.525:0.475. We use attenuation ratios our core-hole clock analysis (Equations 2.1-2.2 in the main text).

Error estimates for CT times have been obtained from the intensity uncertainties of the $\delta\langle q_{22} \rangle = 0.02$ and $\delta\langle q_{44} \rangle = 0.02$ and by using these in Equations 2.1-2.2 to determine the spreads of the CT time values throughout the considered range ($0 < q^{bottom} < 0.85$, this upper limit is set by the $\tau^{bottom} < \tau_{22}$ constraint). For τ_{44} , the resolution of the CHC method is much poorer[68] and the reported value should serve as a lower bound.

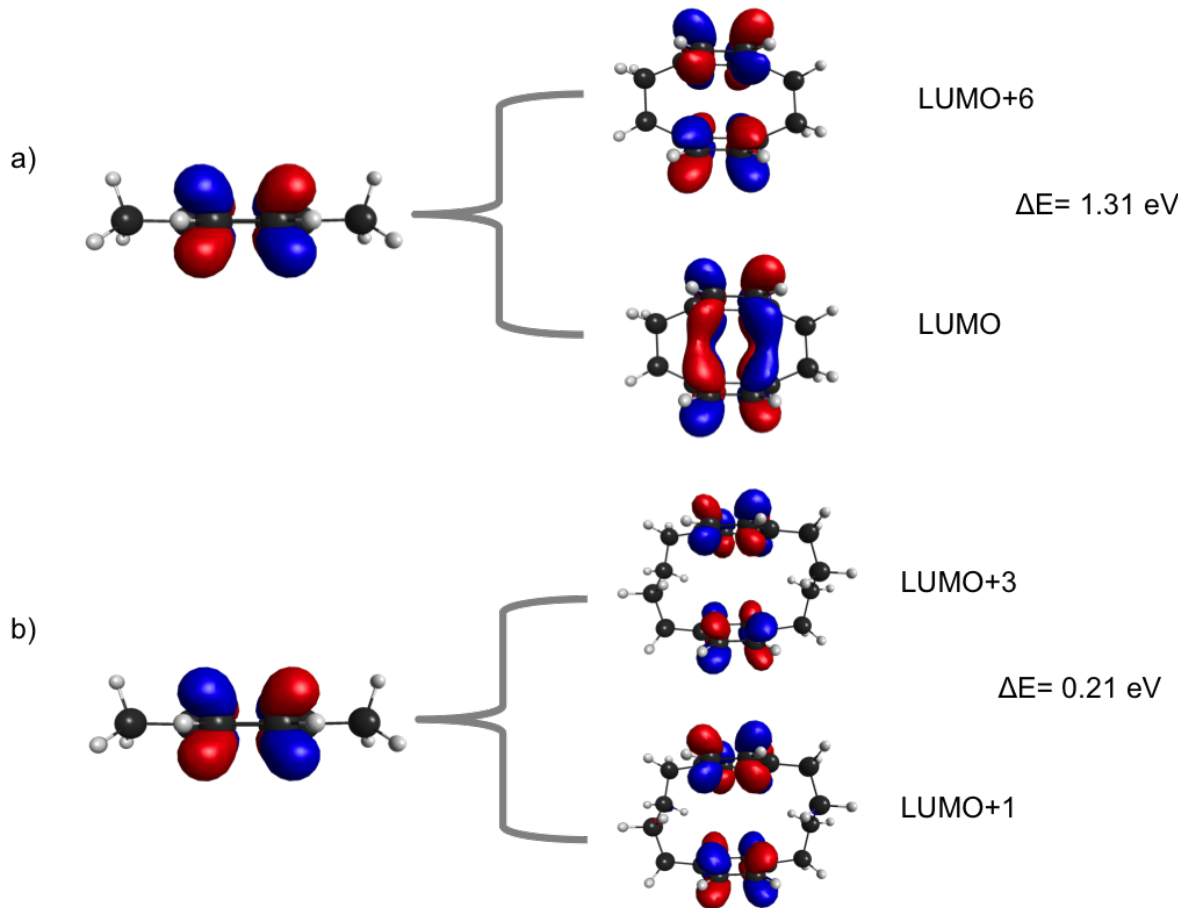


Figure 2.7 – Bonding and Antibonding combinations of xylene LUMO
a [2,2]paracyclophane and **b** [4,4]paracyclophane

Calculation Details Molecules were structurally relaxed by performing spin-unrestricted calculations using the B3LYP exchange-correlation functional and LACV3P** basis set using the Q-Chem software suite[70]. Default grids and convergence thresholds were used for relaxation. Subsequently, single-point calculations were carried out using B3LYP/LACV3P**++ to calculate molecular energy levels. Binding energies were calculated for both molecules with an Au-dimer, following the procedure outlined by Schneebeli, Kamenetska[43]. For NEXAFS Simulations and orbital isosurfaces of Carbon K-edge excited molecules, GPAW, a grid-based real-space projector-augmented-wave (PAW)

code was employed with the B3LYP exchange-correlation functional. Isolated molecules were first relaxed to their optimized geometries, before conducting single point calculations. Default grid spacings and convergence thresholds were employed. All NEXAFS calculations were performed using the half-core-hole approximation[71].

2.2 Molecular Diodes Enabled by Quantum Interference

2.2.1 Preface

This section is based on a manuscript entitled, *Molecular Diodes Enabled by Quantum Interference* by Arunabh Batra, Jeffrey S. Meisner, Pierre Darancet, Qishui Chen, Michael Steigerwald, Colin Nuckolls and Latha Venkataraman (submitted for publication). Chemical synthesis was conducted by Dr. Jeffrey S. Meisner and Qishui Chen from Prof. Colin Nuckolls' group. Theoretical work was conducted in collaboration with Dr. Pierre Darancet and Dr. Michael Steigerwald.

2.2.2 Abstract

We use scanning tunneling microscope break-junction (STM-BJ) measurements to study the low-bias conductance and high-bias current-voltage (IV) characteristics of a series of asymmetric *para*-*meta* connected diphenyl-oligoenes. From tight-binding calculations, we determine that the quantum interference features inherent in our molecular design result in a ‘through-bond’ coupling on the *para* side, and through-space coupling on the *meta*-side. We show that these molecular junctions form single molecule diodes, and show that the rectification results from a difference in the voltage dependence of the coupling strength on the through-bond and the through-space side. The interplay between the applied voltage and the molecule-metal coupling results from the asymmetric polarizability of the conducting orbital under an external field.

2.2.3 Introduction

Molecular diodes are of great interest in the nanoscale electronics community because they are the simplest example of non-trivial electronic behavior in a molecular system, and

because they form the basis for more complicated device architectures.[72, 73] Despite the long-standing interest in the production of these devices, their experimental realization has been difficult, with only a handful of studies showing rectification at the single molecule level.[74, 75, 76] This is because most theoretical designs, such as the Aviram-Ratner model of rectification[77], rely on the complex interplay between many variables, such as the level alignments of the intra-molecular components group and the Fermi level of the metal electrodes.[78] This makes the behavior of such diodes difficult to predict[79, 80]. Simpler ‘unimolecular’ rectifier designs had been proposed[81, 82, 83], but have been demonstrated on thin-films, or many molecule junctions[84, 85, 86, 21]. Theoretical work has also focused on the role of the electronic contact[64] in defining rectification behavior, and recent experimental evidence[74] has shown the efficacy of such an approach in developing tunable rectifiers. Here, we show that quantum interference effects[87, 19] can be used to create asymmetrically coupled molecular junctions[88] that attribute the rectification to a novel mechanism that can in principle be applied to a variety of other molecular structures.

In this work, we measure conductance and current-voltage characteristics in a series of conjugated molecules of increasing length with linkers at the *para* position on one side and at the *meta* position on the other. Our measurements show that these molecular junctions rectify. From our experimental and theoretical results, we conclude that the quantum interference inherent in our molecular design effectively ensures that the molecule’s conducting orbital is strongly coupled to one electrode while allowing only weak electronic coupling to the other electrode. We show further that rectification results from a difference in the voltage dependence of the coupling strength between two sides of the molecule, an effect that depends on the molecular backbone length. The interplay between the applied voltage and the molecule-metal coupling results from the asymmetric polarizability of the conducting orbital under an external field.

2.2.4 Experimental Method

The molecules used in this work are based on diphenyl-oligoene backbones[88] (Figure 2.8A, molecules **1-5**) of lengths ranging from 1.2 nm to 2.3 nm. The backbones are functionalized with two methylsulfide (SMe) linkers[11, 89], in the *para* position on one phenyl ring and in the *meta* position on the other (see SI for synthesis details)[19, 88]. A simple tight-binding based theoretical model of molecular junctions formed using such *para-meta* linked molecules predicts negligible conductance due to an anti-resonance from destructive interference[19, 90, 17] at the Fermi energy (Figure 2.8B). We measure the conductance and current-voltage characteristics of this series of molecules in ambient, room-temperature conditions with a scanning tunneling microscope (STM) in break-junction mode[91, 92, 93, 26]. Conductance measurements under low-bias ($V_{\text{bias}} \sim 250$ mV) conditions are carried out first using 1 mM solutions of the compounds in 1,2,4-trichlorobenzene (Sigma-Aldrich, >99% purity). A gold STM tip is brought into contact with a solution covered gold-on-mica substrate until a junction conductance of $>5 G_0$ ($G_0 = 2e^2/h = 77.6 \mu\text{S}$) is measured. The tip is then withdrawn at a rate of 15 nm/s for 150 ms while current is measured at a constant bias. Inset of Figure 2.8C shows sample conductance traces showing a prominent molecular conductance feature for molecules **1**, **3** and **5**, in contrast with the negligible conductance predicted by tight-binding.

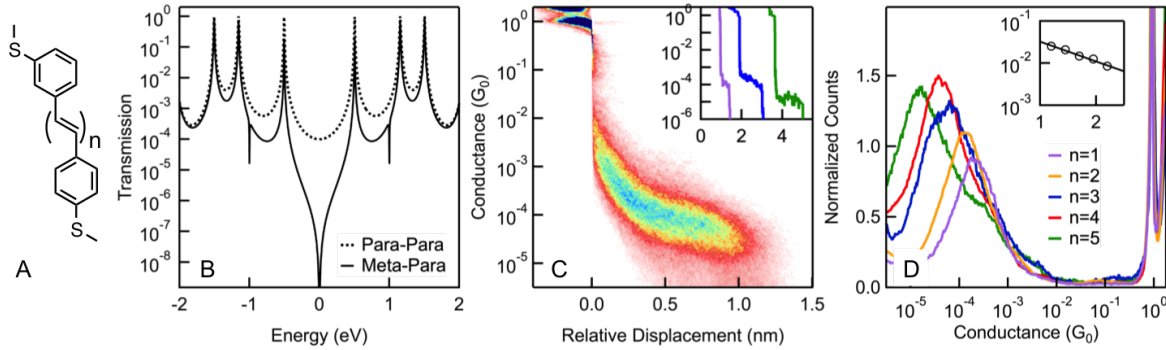


Figure 2.8 – Molecular Structures and Conductance Data

A Molecular structures for molecules with $n = 1\text{--}5$. **B** Tight-binding transmission functions for molecular junctions with molecule **1** (black); this *para*-*meta* system shows negligible transmission probability near E_{Fermi} (0 eV). A *para*-*para* (dashed black) connected version of molecule **1** shows higher transmission. **C Inset:** Sample conductance traces for molecules **1**, **3** and **5** showing molecular plateaus. Two dimensional (2D) conductance histogram for molecule **3**, showing characteristic downward slope in conductance with increasing relative displacement. **D** Conductance histograms for *para*-*meta* connected molecules **1**–**5** showing measurable conductance. Inset: Conductance versus molecule length obtained using S-S distances from DFT optimized structures of molecules **1**–**5** showing a decay constant $b = 0.25/\text{\AA}$.

2.2.5 Results

A two dimensional conductance histogram for these molecules formed by overlaying thousands of such conductance traces (Figure 2.8C) show that the molecular conductances decrease as electrode separation is increased, pointing to pi-Au interaction[94, 95] contributing significantly to molecular conductance. This is in contrast to symmetrically *para*-connected versions of the same molecules studied previously[88] which show a flatter conductance feature pointing to through-bond coupling. We conclude that the asymmetric functionalization allows for one side (*para*) to be electronically coupled ‘through-bond’, and other side (*meta*) to be coupled ‘through-space’[19, 88]. Figure 2.8D show logarithmically binned one-dimensional histograms of thousands of such traces for each molecule without data selection, which allows a characteristic conductance value to be statistically determined.

On going from the shortest molecule, **1**, through the series to the longest molecule, **5**, the conductance decays exponentially (inset Figure 2.8D), with a decay parameter $\beta=0.25 \pm 0.03/\text{\AA}$. This is a similar decay constant to previous studies on the oligoene molecular system[19, 88], and suggests that the pi-Au interaction occurs at end carbons on the phenyl ring near the *meta*-linker, rather than on the backbone.

We next measure the current-voltage (IV) characteristics of these molecules using procedures published previously[92]. Briefly, a gold STM tip is brought into contact with a gold-on-mica substrate. The tip is first withdrawn at a rate of 15 nm/s for 125 ms, and held at this displacement for 150 ms before being withdrawn for an additional 75 ms. During the ‘hold’ section, the voltage is ramped between $\pm 1\text{V}$, while current is measured (Figure 2.9A). The IV procedure is repeated tens of thousands of times, with $\sim 1\text{-}10\%$ of junctions showing a stable, unbroken, molecular conductance signature during the IV measurement. Due to the instability of molecular junctions at higher biases at room temperature, measurements beyond $\pm 1\text{V}$ do not yield sufficient number of traces to analyze statistically. For each molecule, the selected IV traces are binned logarithmically on the current axis, and added together to create a two-dimensional histogram of absolute current against voltage. We recover the inherent asymmetry of the junction by sorting our data into two sets, based on the magnitude of current in a range of positive biases (+0.75 to +0.80V) and corresponding negative voltages (-0.75V to -0.80V)[74]. Traces that show larger current at positive than negative voltages correspond to molecular junctions in the forward orientation; traces that show smaller current at positive than negative voltages correspond to molecular junctions in the reverse orientation.

As an illustration, sorted 2D histograms from **4** are shown in Figure 2.9B (reverse bias, top panel and forward bias, bottom panel). To make a quantitative comparison of the histograms, we fit each vertical slice of the histograms to a Gaussian distribution

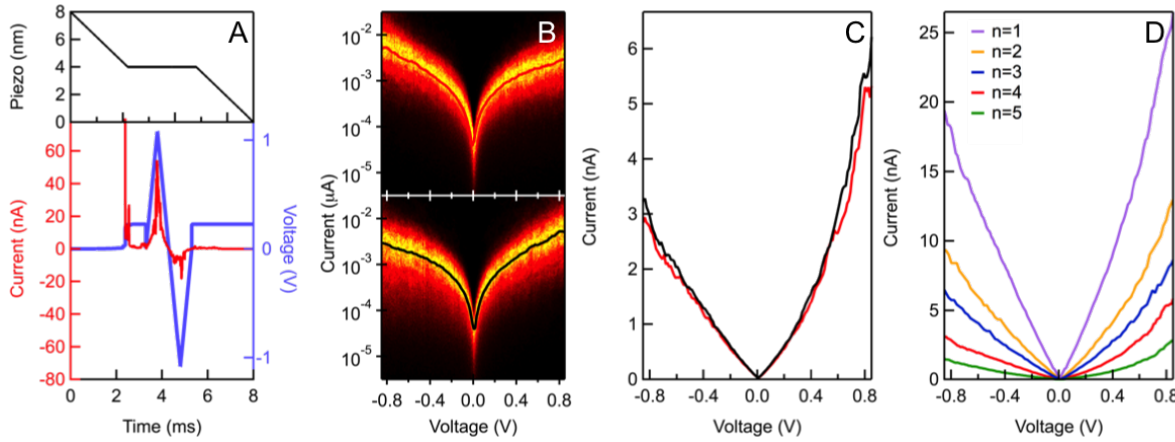


Figure 2.9 – Current-Voltage Measurement

A Representative current, voltage and displacement (piezo z-position) traces for a single break junction measurement for molecule **4**. The IV ramp is applied when z is held constant. **B** Two-dimensional histograms created from thousands of IV curves for molecule 4 that are either in reverse bias (top panel) or forward bias (bottom panel). Average IV curves are overlaid in red and black respectively. **C** Average IV curves from B shown on a linear scale with reverse-bias (red) reflected about the x-axis. **D** Averaged IV curves for molecules **1-5** analyzed following the same procedure detailed in panel B and C.

and extract the most frequently measured current at each voltage[92]. These values are plotted as the red and black IV curves overlaid in the top and bottom panels of Figure 2.9B respectively and are also shown on a linear scale in Figure 2.9C. The resulting curves represent the averaged IV curves for this molecule. The forward bias average IV (black curve, Figure 2.9C) overlays the reverse bias IV (red curve), which has been mirrored in the voltage axis. The near-identical shape of these curves indicates that sorting recovers the inherent structure in the IV curves without biasing the data. A similar sorting algorithm applied to fully symmetric molecules further confirms this conclusion: the separated 2D histograms for these control molecules are identical and do not show rectification[74]. Figure 2.9D compares statistically averaged IV curves for molecules **1-5**. We find that while the absolute current decreases with length, the rectifying behavior increases.

To understand the origin of rectification and its length dependence, we conduct Density

Functional Theory (DFT) calculations of molecules **1-5** (see SI for details) in which we include an electric field applied parallel to the molecular axis. Generally, the factors affecting rectification are voltage dependence in energy level alignment[96] (Stark shifts), or a voltage dependent coupling term Γ . For an applied voltage of $\pm 1\text{V}$, the HOMO of molecules **1-5** show negligible stark shifts ($< 0.1 \text{ eV}$, see SI), not enough to explain the rectification effects observed experimentally. We therefore concentrate on the voltage dependence of the coupling terms on the *para* and *meta* side Γ_{para} and Γ_{meta} . Figure 2.10A shows representative isosurface plots of the HOMO of molecule **5** under an applied field of $\pm 1\text{V}$. Note that the weight of the HOMO on the carbon atoms adjacent to the *para* and *meta* linkers (arrows, Figure 2.10A) changes significantly with field polarity. We can quantify this change in HOMO distribution using the projection of HOMO onto the p_z orbital of the *para* carbon of the ‘through-bond’ coupled side, and the projection of the p_z orbitals of all carbons on the phenyl ring of the ‘through-space’ *meta* connected side of the molecule. The coupling Γ is then proportional to the square of the projection[36, 64]. In Figure 2.10B we plot the fractional change in Γ of either side as a function of applied bias (constant bias for all molecules). Longer molecules have a larger fractional change, due to a higher polarizability. This trend is more pronounced for Γ_{meta} , leading us to attribute the rectification observed here to the asymmetric polarizability of the conducting orbital in this system.

To validate our hypothesis, we develop a tight binding model for conductance through this molecular system. Given the through-space nature of the conductance on the *meta* side of the junction, we use a simple single-Lorenzian[97] representing HOMO, coupled to the left and right electrodes with Γ_{para} and Γ_{meta} (Figure 2.10C, inset)[36, 64]. We can then include the effects of polarizability of HOMO discussed earlier (Figure 2.10A) by imposing a voltage dependence on Γ_{para} and Γ_{meta} corresponding to the calculations in Figure 2.10B.

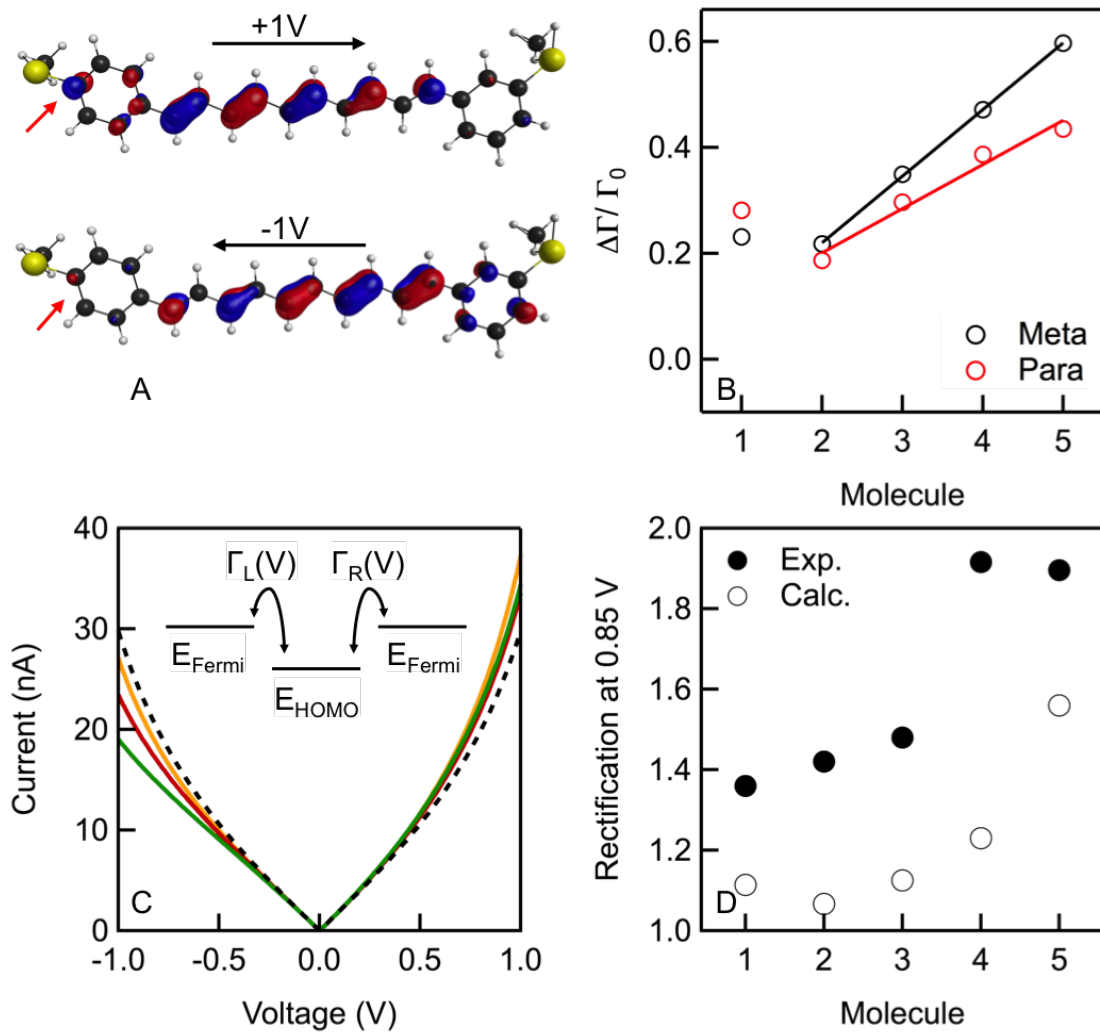


Figure 2.10 – Model for Rectification and Simulated IV Curves

A DFT calculated HOMO for molecule **5** with an applied potential of +1V (upper panel) and -1V (lower panel). Arrow highlights the HOMO orbital weight on the *para* carbon of the strongly coupled side. Isosurface value = 0.05/Å³ **B** Fractional change in coupling Γ_{meta} (black) and Γ_{para} (red), estimated as the square of projection of HOMO on the p_z atomic basis of the *para* atom (Γ_{para}) or the *meta*-connected phenyl ring (Γ_{meta}). **C** Calculated IV curves for a single-level model (Inset) with varying voltage dependence of Γ_{meta} and Γ_{para} . Yellow, red, and green curves show the effect of increasing differences in $\Delta\Gamma_{\text{para}}$ and $\Delta\Gamma_{\text{meta}}$ on IV lineshape. Dashed line shows a non-rectifying case where Γ_{meta} and Γ_{para} have the same voltage dependence. **D** Rectification ratio calculated (solid markers) from the ratios shown in B, compared with experimental data (open circles). Both ratios increases with increase in molecular length.

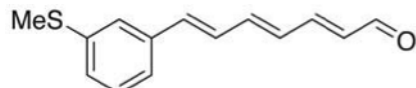
We calculate IV curves with varying voltage dependences of Γ_{para} and Γ_{meta} (Figure 2.10C) and find that rectification increases with difference in $\Delta\Gamma_{\text{para}}$ and $\Delta\Gamma_{\text{meta}}$ (Figure 2.10D). When $\Delta\Gamma_{\text{para}}$ and $\Delta\Gamma_{\text{meta}}$ are equal, no rectification occurs (dashed IV curve). Our model explains the length dependence of our data, and suggests that rectification occurs due not to a difference in Γ between the two sides, but due to a difference in $\Delta\Gamma$ which we attribute to the different nature of electronic coupling on the *para* (through-bond) and *meta* (through-space) sides. Further, our model shows that increasing the length of the molecule can enhance rectification by increasing the asymmetric polarizability of the conducting orbital (in this case, HOMO).

In summary, we have used the unique properties of quantum interference to create a series of asymmetrically coupled molecular diodes. We find that rectification ratios increase with molecular length, and model this trend using a tight-binding model taking into account the asymmetric coupling in these molecular junctions. We show that the increase in rectification is due to differences in the voltage-dependence of ‘through-space’ and ‘through-bond’ coupling terms with molecular length.

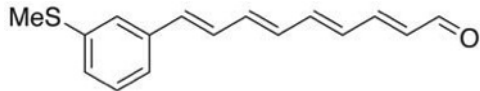
2.2.6 Supplementary Information

2.2.6.1 Synthesis

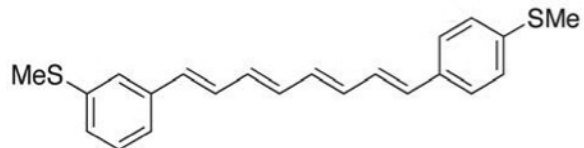
Preparation of molecules **1-3** has been described previously[20]. Here we describe procedures for preparing molecules **4-5**.



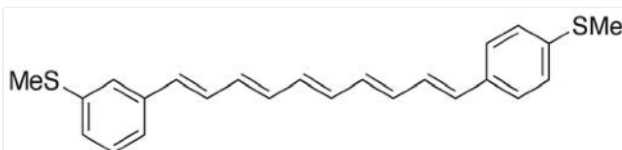
7-(3-(methylthio)phenyl)hepta-2,4,6-trienal: General Wittig homologation procedure.
 HR-MS: m/z calcd for (C₁₄H₁₄S): 230.0765, found: 230.0754.



9-(3-(methylthio)phenyl)nona-2,4,6,8-tetraenal: General Wittig homologation procedure. HR-MS: m/z calcd for (C₁₆H₁₆OS): 256.0922, found: 256.0922.



1-(3-(methylthio)phenyl)-8-(4-(methylthio)phenyl)-octa-1,3,5,7-tetraene: A General HWE procedure was followed. The product was prepared from the corresponding trienal and dimethyl 4-(methylthio)benzyl phosphonate and was isolated by recrystallization from CH₂Cl₂/MeOH as a yellow solid in 49% yield. ¹H NMR (500 MHz, C₂D₂Cl₄): δ 7.35 (d, J = 8.4 Hz, 2H), 7.28 (bs, 1H), 7.26 (d, J = 7.7 Hz, 1H), 7.21 (m, 3H), 7.12 (d, J = 7.7 Hz, 1H), 6.94-6.78 (m, 2H), 6.56 (d, J = 15.5 Hz, 1H), 6.55 (d, J = 15.5 Hz, 1H), 6.47 (m, 4H), 2.52 (s, 3H), 2.51 (s, 3H); ¹³C NMR (500 MHz, C₂D₂Cl₄): δ 138.21, 137.43, 137.29, 133.66, 133.54, 133.33, 132.74, 132.69, 131.67, 131.35, 129.38, 128.64, 128.08, 126.30, 125.95, 124.93, 123.66, 122.68, 15.24, 15.17; HR-MS: m/z calcd for (C₂₂H₂₂S₂): 350.1163, found: 350.1169.



1-(3-(methylthio)phenyl)-10-(4-(methylthio)phenyl)-deca-1,3,5,9-pentaene : General HWE procedure was followed. The product was prepared from the corresponding trienal and dimethyl 4-(methylthio)benzyl phosphonate and was isolated by recrystallization from

CH2Cl2/MeOH as a light orange solid in 40% yield. ^1H NMR (500 MHz, C2D2Cl4): δ 7.34 (d, $J = 8.3$ Hz, 2H), 7.28 (bs, 1H), 7.25 (d, $J = 87.7$ Hz, 1H), 7.20 (m, 3H), 7.12 (d, $J = 7.7$ Hz, 1H), 6.91-6.79 (m, 2H), 6.54 (d, $J = 15.5$ Hz, 1H), 6.53 (d, $J = 15.5$ Hz, 1H), 6.49-6.37 (m, 6H), 2.51 (s, 3H), 2.50 (s, 3H); ^{13}C NMR (500 MHz, C2D2Cl4): d 138.21, 137.44, 137.26, 133.69, 133.63, 133.31, 133.23, 132.90, 132.79, 131.73, 131.59, 131.35, 129.41, 128.64, 128.14, 126.29, 125.95, 124.94, 123.66, 122.68, 15.24, 15.18; HRMS could not be obtained due to insolubility in methanol

DFT Calculation Details Molecules were structurally relaxed by performing spin-unrestricted calculations using the B3LYP exchange-correlation functional and 6-31G* basis set using the Q-Chem software suite[70]. Default grids and convergence thresholds were used for relaxation. Subsequently, single-point calculations were carried out using B3LYP/6-311G** either without field, or with a monopole field applied along the long axis of the molecule. For molecules **1-5**, projections of HOMO onto p_z atomic orbitals of the six ring carbons on the weakly coupled (*meta*) side and single carbon on the strongly coupled (*para*) sides were calculated (see Figure 2.10b in the main text). Figure 2.11A and B show the change projection onto the six carbon atoms on the *meta* side and a single carbon atom on the *para* side as a function of molecular length. Γ is assumed to be proportional to the square of the projections shown in Figure 2.11. A voltage dependence on Γ is incorporated using $\Gamma_i = \Gamma_0 \cdot (1 + \nu_i \cdot V)$, where Γ is the zero-field Γ and ν_i is calculated from the slope of the trend-lines plotted in Figure 2.11.

The single-level model described in Figure 2.10c results in a transmission function of the form:

$$T(E, V) = \frac{\Gamma_{para}\Gamma_{meta}(1 + \nu_{para}V) \cdot (1 + \nu_{meta}V)}{(E - E_0)^2 - \frac{1}{4}(\Gamma_{para} \cdot (1 + \nu_{para}V) + \Gamma_{meta} \cdot (1 + \nu_{para}V))^2}$$

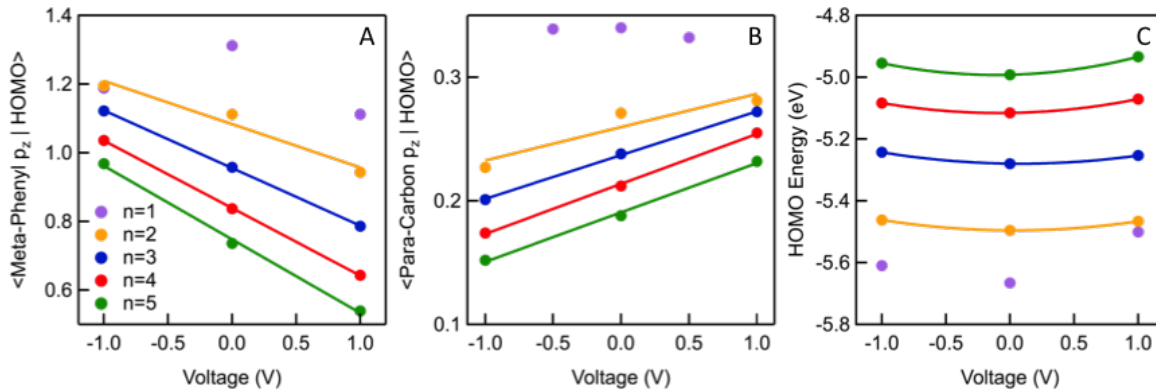


Figure 2.11 – Effect of electric field on orbital projections and energies

Projection of HOMO on the p_z orbitals of six ring carbons on the *meta* side (**A**) and carbon attached to the sulfur on the *para* side (**B**) of the molecule for constant voltage of $\pm 1\text{V}$ (for **1-5**). Molecules **2-5** (purple, yellow, blue, red, and green respectively) all show a linear dependence of projection on voltage. molecule **1** shows nonlinearities associated with a dipole moment along the length of the backbone. **C** Stark shifts for HOMO as a function of constant field (voltage scaled with molecular length, with $\pm 1\text{V}$ applied to molecule **5**). Molecules **2-5** show quadratic dependence on field, as expected for molecules without significant dipoles. molecule **1** shows a slight stark shift due to a dipole moment along the length of the molecule.

Next, IV curves are generated using the Landauer formula:

$$I(V) = \frac{2e}{h} \int dE T(E, V) \left[f(E + \frac{eV}{2}) - f(E - \frac{eV}{2}) \right]$$

where f is the Fermi distribution function. We take the temperature to be 0K, although results from using T=300K will not be very different.

Chapter 3

The Covalent Gold-Carbon Bond

3.1 Trimethyltin mediated gold-carbon bond formation

3.1.1 Preface

This chapter is based on a manuscript entitled *Trimethyltin mediated gold-carbon bond formation*, by Arunabh Batra, Gregor Kladnik, Narjes Gorjizadeh, Michael Steigerwald, Colin Nuckolls, Su Ying Quek, Dean Cvetko, Alberto Morgante and Latha Venkataraman (submitted for publication). The experimental work was conducted at the ALOISA Beamline at the Elettra Synchrotron in Trieste, Italy, in collaboration with Prof. Dean Cvetko, Dr. Gregor Kladnik and Prof. Alberto Morgante. Theoretical work was conducted in collaboration with Dr. Narjes Gorjizadeh and Prof. Su Ying Quek at the Department of Physics, National University of Singapore.

3.1.2 Abstract

We study the formation of covalent gold-carbon bonds in benzyltrimethylstannane ($C_{10}H_{16}Sn$) deposited on gold in ultra high vacuum conditions. Through X-ray Photoemission Spectroscopy (XPS) and X-ray absorption measurements, we find that the molecule fragments at the Sn-Benzyl bond when exposed to gold surfaces at temperatures as low as -110C. We show that the resulting benzyl species is stabilized by the presence of Au(111), but only forms covalent Au-C bonds on more reactive Au surfaces like Au(110). In addition, we present spectroscopic proof for the existence of an electronic ‘gateway’ state localized on the Au-C bond that is responsible for the unique electronic properties of this bond. Finally, we use Density Functional Theory based Nudged Elastic Band methods to find reaction pathways and energy barriers for this reaction, and elucidate the crucial role played by pi-Au interaction in the formation of Au-C bonds.

3.1.3 Introduction

A well-defined, robust, metal-organic contact is a fundamental ingredient in most organic electronics systems. Such contacts not only offer mechanical anchoring of organic components, but also define and enhance the electronic characteristics of devices. A popular method of achieving such contacts is the gold-thiol bond[98]; the covalent nature of the gold-sulfur bond provides superior mechanical stability and high electronic transparency[99]. Additionally, these bonds form well-packed, uniform self-assembled monolayers[100, 101] making experimental studies on thin films convenient. However, the non-specific nature of the gold-sulfur bond formation[102, 103] means that well-defined molecule-metal geometries, and consequently electronic properties[104], are difficult to obtain[105]. Additionally, problems with thermal stability and degradation due to oxidation[106] have led researchers to explore alternatives such as a variety of donor-acceptor bonds[107] and recently, covalent

gold–carbon bonds[108]. Direct gold–carbon bonds are often formed electrochemically, by the reduction of aryldiazonium salts in solution[109, 110]. Covalent sigma gold–carbon also been formed using terminal alkynes[111], organomercury salts[112], trimethylsilyl linkers[113], and trimethyltin leaving groups[108].

Recently, Chen and coworkers[114] have demonstrated the use of benzyltrimethyltin molecules to achieve gold–carbon bonds which are pi-coupled to the orbitals of the conjugated molecular backbone. In single-molecule experiments, they have shown near-resonant molecular conductance, nearly 100 times that of molecules with conventional linker groups[114]. The electronic properties of these pi-coupled Au-C bonds have also been shown to facilitate desirable thermoelectric characteristics[97], and have been integrated into tunable molecular diode designs[115]. Theoretical calculations[115, 114] suggest that a hybridized gold-molecule ‘gateway’ state that is localized on the Au-C bond is responsible for many of the unique electronic properties of these pi-coupled Au-C bonded systems, though there is no experimental evidence for the existence of such a state.

Here, we study the formation of Au-C bonds using benzyltrimethylstannane ($C_{10}H_{16}Sn$) molecules on a variety of gold surfaces in ultra high vacuum (UHV) conditions. In contrast with studies[108, 114] conducted on similar systems in organic solvent solutions in ambient conditions, this UHV study allows us to isolate the role played by gold in such reactions. Through X-Ray Photoemission Spectroscopy (XPS) measurements, we show that, even at temperatures as low as -110C in the presence of a gold substrate, $C_{10}H_{16}Sn$ cleaves at the Sn-C bond to form trimethyltin (C_3H_9Sn) and benzyl (C_7H_7) species. The resulting trimethyltin fragments readily form Sn-Au bonds on all surfaces, while the fate of the benzyl species is determined by the reactivity of the gold surface. On Au(111), XPS core level shifts point to the formation of a surface-stabilized benzyl species. In contrast, XPS on Au(110) shows no such shift; instead, Near-Edge X-Ray Absorption Fine Structure

Spectroscopy (NEXAFS) on this surface shows the formation of an Au-C bond with a well-hybridized electronic ‘gap’ state. Finally, through Density Functional Theory (DFT) based implementations of Nudged Elastic Band calculations[116], we determine a mechanism for Au-C bond formation and understand the essential role played by pi-Au interaction and the under-coordinated gold surface in catalyzing these reactions.

3.1.4 Experimental Methods

We characterize the cleavage of benzyltrimethylstannane (Figure 3.1a) using XPS measurements of monolayer films of the molecule deposited on Au(111), Au(110), and sputtered Au surfaces. These measurements are carried out at the ALOISA/HASPES beamline[65] (Elettra Synchrotron, Trieste). The Au substrates are first cleaned by repeated cycles of Ar sputtering and annealing to 800K. XPS measurements of the Au are made to ensure no contamination on the sample. The base pressure for the measurement chamber is maintained at 10^{-11} mbar and the sample preparation chamber at 10^{-10} mbar. Benzyltrimethylstannane is synthesized using previously reported methods[117] is deposited on this substrate from a quartz Knudsen-type cell in line-of-sight with the sample preparation chamber. For monolayer and multilayer depositions, the Au substrate is cooled to -110C and the Knudsen cell is heated to 50C. Deposition of monolayers is controlled by monitoring XPS core level positions for C1s, along with C1s to Au4f intensity ratios. The molecule is deposited at a chamber pressure of 10^{-8} mbar with a typical rates of $\sim 2 \text{ \AA/min.}$

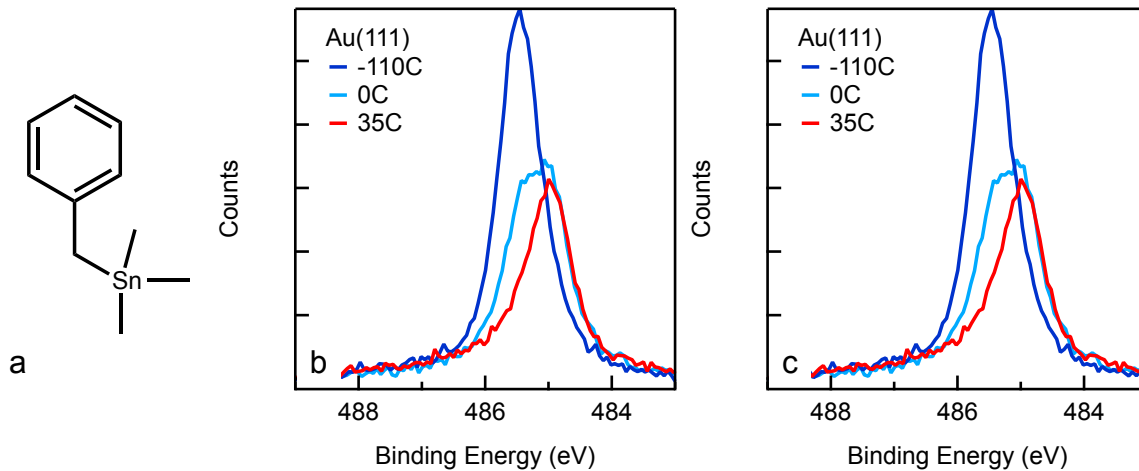


Figure 3.1 – Molecular Structure and Tin XPS Measurement

a) Trimethylstannane ($C_{10}H_{16}Sn$) molecular structure **b)** XPS of $Sn3d_{5/2}$ for a monolayer of Trimethylstannane on Au(111) at three temperatures, -110C (dark blue), 0C (light blue), and 35C (red). **c)** XPS of $Sn3d_{5/2}$ for a monolayer of Trimethylstannane on Au(110) at -110C (dark blue) and 35C (red).

We first compare the XPS signal of $Sn3d$ core levels (Figure 3.1b-c) as a function of substrate temperature on Au(111) and Au(110). In the case of Au(111) at -110C (dark blue, Figure 3.1b), the $Sn3d_{5/2}$ peak is a broad feature centered at 485.4 eV. As the substrate temperature is raised to 0C (light blue), the $Sn3d_{5/2}$ signal decreases dramatically, and a second lower binding component arises at 485.0 eV. As the substrate is heated further to 35C (red, Figure 3.1b), the lower binding component dominates. A similar trend is seen in Au(110) (Figure 3.1c), with a shift of 0.4 eV in $Sn3d$, and an even more dramatic loss of Sn. The downward core-level shift of 0.4 eV between the original and new peaks corresponds to the chemical shift between Sn-C and Sn-Au bonds[118, 119], pointing to the conversion of trimethyltin fragments into gold-bound trimethyltin upon heating on both Au(111) and Au(110).

Figure 3.2a and b compare the C1s peaks for the Au(111) and Au(110) surfaces. For Au(111) (Figure 3.2a), we see a broad C1s peak at 283.8 eV when with the substrate at

-110C (dark blue). As substrate temperature is raised to 0C (light blue), some carbon signal is lost from the original peak and a ‘lower-binding’ peak emerges as a shoulder at 282.9 eV. As the temperature is raised to 35C the 282.9 eV peak in C1s becomes more prominent. This 0.9 eV core level shift between the two C1s peaks is consistent with calculations[120] of XPS shifts for a surface-stabilized benzyl radical on Au(111). In addition, we find that the XPS ratio for the two carbon species (283.8 eV C1s to 282.9 eV C1s peak) at 35C corresponds to a stoichiometric ratio of 8:1, which is consistent with the expected ratio for a surface stabilized benzyl radical once the desorption of trimethyltin is accounted for (see SI for details). On Au(110) (Figure 3.2b) we find that while there is a loss of carbon, there is no new peak with a 0.9 eV shift. This suggests that a surface-stabilized radical is likely not forming on Au(110) as it does on Au(111), but instead, a covalent Au-C bond is formed, which, based on previous studies shows a very minimal XPS shift.[112, 121]. Further evidence for the formation of covalent Au-C bonds on Au(110) is presented later in the paper.

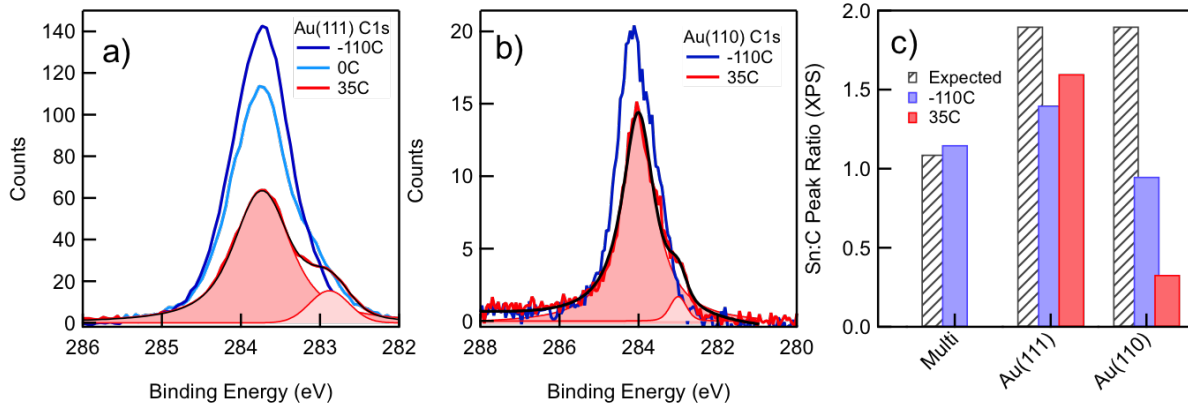


Figure 3.2 – Carbon XPS and Stoichiometric Ratios

Carbon 1s XPS of a monolayer of Benzyltin on **a)** Au(111) at -110C (dark blue), 0C (light blue), and 35C (red). **b)** C1s XPS for monolayer on Au(110) at -110C and 35C. Black lines represent a best fit of the 35C XPS signal using two Voigt functions (filled red). **c)** Ratio of XPS peak areas for Sn:C at -110C (blue bars) and 35C (red bars) for multilayer, Au(111), and Au(110). Shaded white bars represent the expected ratio of Sn:C.

We now examine overall Sn:C signal ratio in Figure 3.2c, which shows calculated (shaded bars, see SI for details) Sn:C XPS signal ratios against measured values for multilayer films and monolayers on Au(111) and Au(110). In contrast with the multilayer where measured and expected Sn:C ratios agree well, monolayers on Au(111) and Au(110) both show less Sn than expected at all temperatures. These data together point to fragmentation of the original molecule into a purely carbon-containing benzyl fragment and a trimethyltin fragment, both of which have different affinities for the gold surfaces. The proportionally lower Sn signal on under-coordinated surfaces like Au(110) is in agreement with previous theoretical studies[108] showing that trimethyltin prefers to bind on flat gold.

We turn next to NEXAFS spectra of the Carbon K-edge to study the unoccupied energy levels of the cleaved molecular fragments on Au(111) and Au(110). NEXAFS spectra are collected with incident photon energy between 280 eV and 310 eV with the electric field polarization either parallel (s-pol) or perpendicular (p-pol) to the sample, and with the beam incidence angle of 6°.

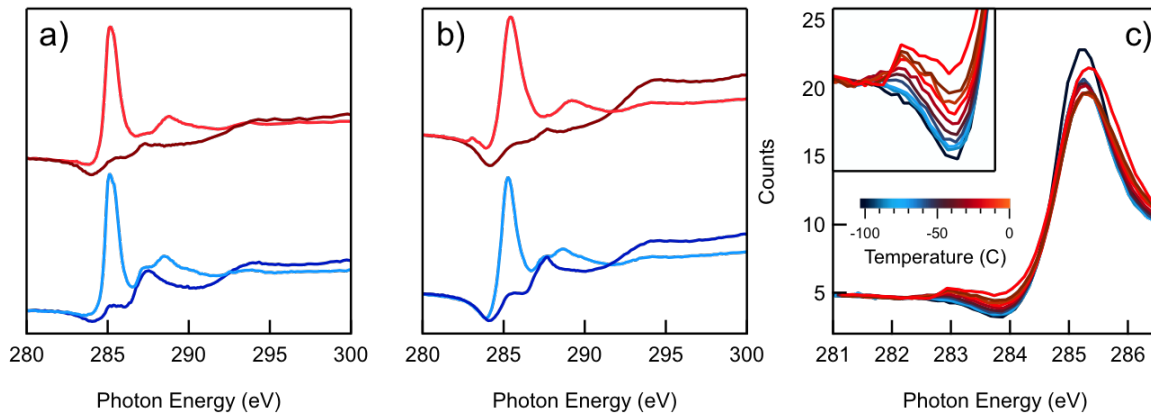


Figure 3.3 – NEXAFS Measurements

Carbon K-edge NEXAFS taken in s-pol (dark colors) and p-pol (light colors) of a monolayer of on **a)** Au(111) at -110C (blue) and 30C (red) **b)** Au(110) at -100C (blue) and 20C (red) **c)** NEXAFS taken in p-pol on a sputtered gold surface, as a function of temperature.

Figures 3.3a and 3.3b show NEXAFS measurements for monolayers of benzyltrimethyl-

stannane on Au(111) and Au(110) respectively. At -110C (blue curves), the NEXAFS spectra are dominated by a prominent π^* peak[32] at 285 eV in p-pol (light colors). This ‘dichroism’ in NEXAFS indicates that the molecules lie with the benzene rings relatively flat on both substrates. At 35C (red curves) on both surfaces, the π^* peaks broaden along with significant loss of signal at 288 eV. The peak at 288 eV corresponds to the C-H sigma*[32] mode, and the loss of intensity here at 35C is consistent with a loss of trimethyltin on both surfaces. The NEXAFS spectra on both Au(110) is quite different from that of Au(111) in that we see a significantly broadened π^* peak as the monolayer is heated on Au(110) and we find an additional prominent peak emerges around 283 eV in the pre-edge region (arrow, Figure 3.3b). Simulated NEXAFS calculations on an $\text{Au}_1\text{-Benzyl}$ molecule (See SI for details) show that the pre-edge feature occurs due to the excitation of a core-level electron from the C atom bound to Au to the lowest unoccupied molecular orbital (LUMO) of the $\text{Au}_1\text{-Benzyl}$ species. This LUMO orbital, now singly occupied, extends spatially to the benzyl carbon and the Au-C bond, and suggests that the covalent Au-C bond is well hybridized with the LUMO of the benzyl. Additionally, theory shows that this state is oriented along the Au-C bond direction; this theoretical evidence along with the fact that the pre-edge feature is absent in s-pol (dark red, Figure 3.3b), shows that the Au-C bond points out of the surface.

The pre-edge peak corresponding to the ‘gap state’ seen in carbon K-edge NEXAFS is absent in Au(111) indicating that covalent Au-C bonds form preferentially on under-coordinated surfaces. To test the dependence of this feature on surface coordination, molecules were deposited on a cold sputtered Au surface, prepared by Ar sputtering of an Au(111) substrate maintained at -100C. After molecular deposition, rapid NEXAFS scans in p-pol were measured as a function of increasing substrate temperature (Figure 3.3c). Figure 3.3c shows a gradual increase of both the width of the π^* peak, and a conspicuous

emergence of the pre-edge ‘gap state’ (Figure 3.3c, inset). These trends as a function of temperature coincide with the shifting of the XPS core-level shifts in carbon and tin shown in Figure 3.1 and 3.2, and point to interaction of the benzyl fragment with Au as the origin. Taken together, the evidence obtained from XPS and NEXAFS reveals a consistent picture of the reaction on gold surfaces: benzyltrimethylstannane cleaves to form benzyl and trimethyltin fragments on both Au(111) and Au(110) surfaces. Upon thermal activation, trimethyltin radicals readily form Au-Sn bonds on both surfaces, resulting in XPS chemical shifts (Figures 3.1b and 3.1c). In contrast, the fate of the benzyl counterpart is substrate dependent: it forms a surface stabilized radical on Au(111) with a significant chemical shift in XPS (Figure 3.2a), while on Au(110) it forms a Au-C bond with a well coupled gap state near the Fermi level of gold, and localized on the bond (Figure 3.3b). The fact that this state is so close to the Fermi level and is so well hybridized with the pi-orbitals generally attributed to charge transport suggests that the gap state seen in our NEXAFS measurements is, in fact, the ‘gateway’ state theorized to explain the special electronic properties of Au-C bonded molecular electronic devices[108, 117].

3.1.4.1 Theoretical Methods

To understand the role of under-coordinated gold in this process that results in the formation of an Au-C bond, we turn to DFT based nudged elastic band (NEB) calculations for this molecule on an Au(111) surface with an adatom to serve as the under-coordinated gold site. To find the preferred binding sites of the cleaved fragments on Au, we relax benzyl and trimethyltin near the adatom using the plane-wave pseudopotential method as implemented in the VASP 5.2 code[122] with projector-augmented-wave (PAW) pseudopotentials,[123] and the local density approximation (LDA)[124] for the exchange-correlation energy. The van der Waals density functional[125, 126] method with optB86b functional is included for calculating the non-local vdW interactions between the molecule and the surface (See

SI for details).

To compute the minimum energy path (MEP) starting with the intact molecule on surface geometry and ending with the fragments bound on the surface, we use the climbing-image nudged elastic band (CI-NEB) method as implemented in VASP.[127] This CI-NEB method guarantees that the maximum energy in the MEP is a saddle point in the energy surface. In Figure 3.4a we show the reaction mechanism for the dissociation of the intact molecule on the Au (111) surface with an Au adatom, as obtained using the CI-NEB method. For the initial configuration (image 0), we relax the intact molecule starting at different positions relative to the Au adatom, and choose the one with the lowest energy. The lowest energy geometry has the smallest Sn-Au distance of all relaxed initial position guesses (see SI Fig. 2). Despite this, charge density difference plots (Figure 3.4b) show that the majority of charge reorganization occurs at the C nearest to Sn, which we label as C1 (circled in image 0, Figure 3.4a). This indicates that Sn does not participate in binding between the intact molecule and the Au adatom; initial interaction is between the Au adatom and C1. For the final configuration (image 6), we compared the total energies of the system with both benzyl and trimethyltin bound to different sites (adatom and flat Au surface; SI Fig. 3). We found that in the final state, benzyl strongly prefers binding to the adatom site rather than the flat surface (by ~ 0.6 eV). Trimethyltin can co-adsorb on the adatom or bind to the flat surface, the former being favored slightly (~ 0.04 eV). Since the undercoordinated Au adatom is likely to be a reactive site in Au, we consider a final configuration where both trimethyltin and benzyl are bonded to the Au adatom. After obtaining the initial and final configurations, images 1-5 are generated by linear interpolation between them.

The optimized energy path (Figure 3.4a) shows that the intact molecule drifts so that the Au adatom moves closer to C1 and away from Sn. From the initial state to the

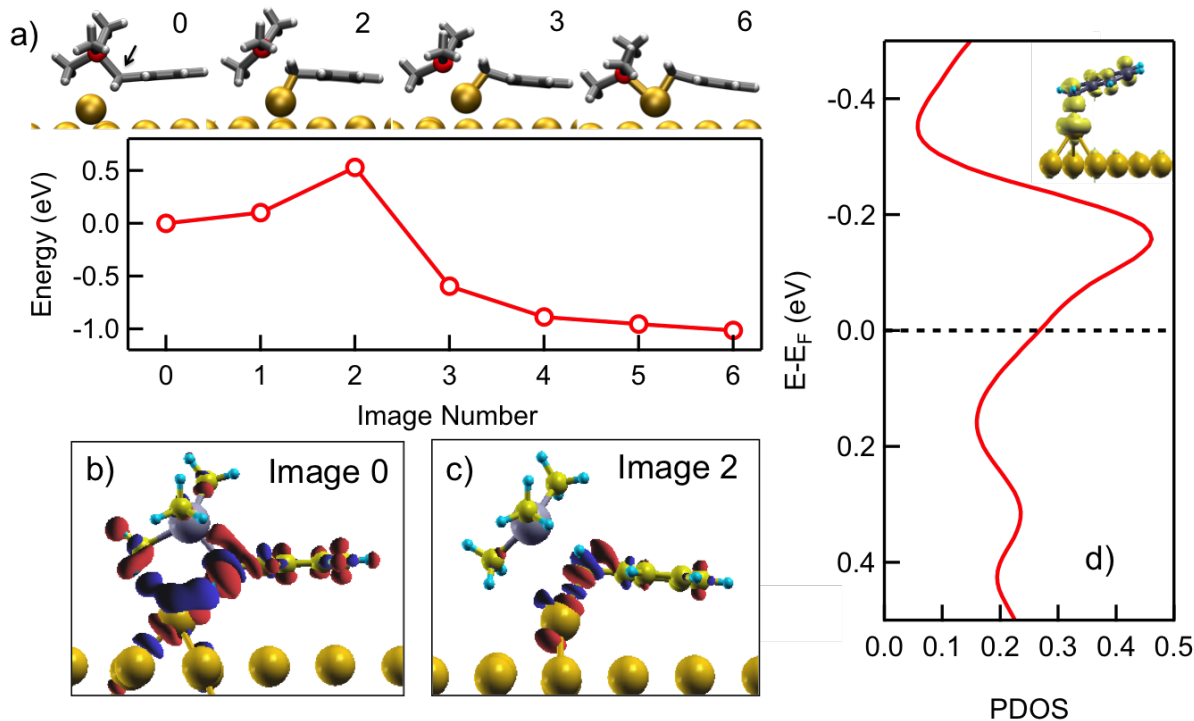


Figure 3.4 – Calculated Trajectories and Density of States

Nudged Elastic Band Calculations on Au(111)+adatom surface. a) Minimum energy path for dissociation of the intact molecule on Au(111) with an adatom obtained from climbing image nudged elastic band (CI-NEB) calculations. Arrow points to atom C1 in Image 0 b) Charge density difference plot calculated for Image 0 relative to isolated Au slab and isolated molecule c) Charge density difference plot for the transition state, Image 2. d) Partial density of states (PDOS) on atom C1.

transition state the C1-Au bond reduces from 2.8 Å to 2.1 Å, while C1-Sn bond increases from 2.2 Å to 2.7 Å. In image 0 before the transition state, the hydrogens attached to C1 point downwards away from Sn and toward Au, indicating that C1 is sp^3 coordinated with a carbon, two hydrogens, and the tin. At the transition state, however, the hydrogens attached to C1 point away from Au indicating that the sp^3 coordination for C1 now involves Au instead of Sn. Therefore, the C1-Sn bond weakens while a C1-Au bond forms at the transition state. This calculated trajectory emphasizes the fact that Au attacks the benzylic carbon (C1) and not the Sn atom. The fact that the C1-Sn bond is cleaved rather than any of the three methyl carbons is likely due to the energy gained due to resonance stabilization due to the aromaticity of the benzylic fragment. Calculation of charge density difference (Figure 3.4c) of the transition state, image 2, shows Au-C1 bonding in the transition state by hybridization of d_{z^2} orbital of Au adatom with p_z orbital of C1. The fact that C1 is the active site in the reaction is consistent with our observation that binding between the intact molecule and the Au adatom takes place between Au and C1 (instead of Au and Sn). This is in contrast to previous reports of Au-Sn bond formation[128] in solution-phase chemistry carried out in ambient conditions. Finally, an analysis of the projected density of states (PDOS) on atom C1 (Figure 3.4d) shows a significant density around E_{Fermi} , which is consistent with NEXAFS results showing a new hybridized state close to the Fermi edge.

This NEB calculation predicts the reaction barrier to be 0.53 eV; the relatively low barrier to this reaction is a consequence not only of the favorable interaction of C1-Au, but also of energy gained due to pi-Au interaction. This can be seen in the significant tilt of the benzene ring towards the Au surface as we go from Image 2 to 6 in Figure 3.4a. This tilt also allows the C1-Au bond to achieve the distance and angle necessary for its sp^3 configuration. In contrast, on an Au(111) surface without the adatom, the pi-system of

the benzene ring lies flat on Au, and cannot tilt towards the surface due to repulsive forces. This restricts the orientation of the C1 carbon relative to the Au surface, and prevents the formation of the covalent bond on Au(111).

3.1.5 Conclusion

In summary, we have shown that Sn-C bonds in benzyltrimethylstannane are cleaved by Au surfaces. We show through XPS and NEXAFS studies that Au-C bonds are only formed on under-coordinated Au surfaces. Importantly, we find direct evidence for a new electronic state near the Fermi energy, which is similar to the gateway states hypothesized in previous literature[108]. Finally, we use DFT-NEB to gather a detailed understanding of the reaction pathway for the formation of Au-C bonds on gold surfaces. These results together provide a general understanding of this reaction that can be used to engineer new molecule-metal interfaces and molecular devices incorporating direct gold-carbon bonds.

3.1.6 Supplementary Information

3.1.6.1 Reaction Pathway Calculations

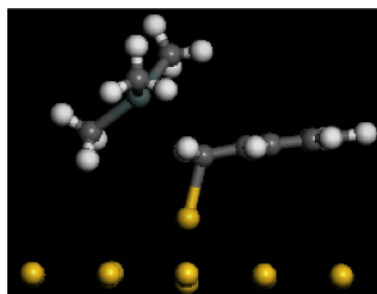


Figure 3.5 – Transition state for NEB

Transition state (TS) for dissociation of molecule on Au adatom obtained from constrained relaxation technique. The TS obtained from constrained relaxation is similar to the one obtained from NEB (Figure 3.4).

To find the preferred binding sites of the cleaved fragments on Au, we relax benzyl and trimethyltin on the Au(111)+adatom using the plane-wave pseudopotential method as implemented in the VASP 5.2 code[122] with projector-augmented-wave (PAW) pseudopotentials[123], and the local density approximation (LDA)[124] for the exchange-correlation energy. The van der Waals density functional method with optB86b functional is included for calculating the non-local vdW interactions between the molecule and the surface. The vdW_optB86b functional predicts the lattice constant of Au 1% smaller than the experimental value (4.08 Å), which is the closest value compared to other functionals, such as vdW_revPBE, vdW_optB88 and vdW-DF2, in agreement with Klimes, Bowler and Michaelides[126]. Using this vdW functional, the relaxed intact molecule on Au(111) has a tilt angle of 83° between the plane of the phenyl ring and the surface normal, in excellent agreement with experiment.

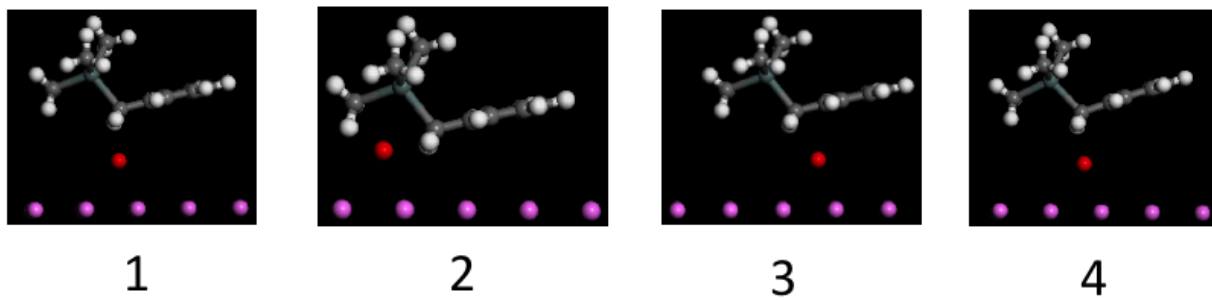


Figure 3.6 – Intact molecule on Au(111) surface with adatom

Relaxed structures of intact molecule on Au adatom on Au(111) with different positions relative to adatom. Structure 1 is the most favorable structure.

Benzyl and trimethyltin are relaxed on Au(111) flat surface on atop, bridge, hollow FCC and hollow HCP sites, and also on adatom on Au (111) surface. Six layers of Au with a 4x4 supercell (16 atoms per layer) are considered, where the three bottom layers are fixed and the rest are allowed to relax. A Monkhorst-Pack 2x2x1 k-point mesh is used for

the relaxations and a 4x4x1 mesh is used to calculate the total energies. The cut-off energy for the plane-wave expansion is set to 400 eV. Calculation of binding energies of benzyl and trimethyltin on Au on different binding sites shows that trimethyltin strongly favors binding to the flat Au(111) surface, being ~0.4 eV more stable on Au(111) than on the Au adatom (the different binding sites on flat surface have very similar binding energies; see Table 3.1. On the other hand, the binding energy for benzyl on the Au adatom is only ~0.1 eV less stable than on the favored (atop) binding site on Au(111). These results indicate that there is a larger probability for benzyl to bind to adatom sites compared to trimethyltin.

Molecular Fragment	Au adatom //Au(111)	Au(111)-atop	Au(111)-bridge	Au(111)-hollowFCC	Au(111)-hollowHCP
SnMe₃	-2.18	-2.60	-2.61	-2.59	-2.63
Benzyl	-1.75	-1.87	-1.74	-1.13	-1.22

Table 3.1 – Binding Energies with vdW-optB86b functional

Binding energies (eV) ($E_b = E_{\text{Au+molecule}} - E_{\text{Au}} - E_{\text{molecule}}$) of benzyl and SnMe₃ on Au on different binding sites using vdW-optB86b functional. Total energy of molecule fragment is obtained by spin-polarized calculations.

Molecular Fragment	Au adatom //Au(111)	Au(111)-atop	Au(111)-bridge	Au(111)-hollowFCC	Au(111)-hollowHCP
SnMe₃	-1.85	-1.70	-1.66	-1.62	-1.67
Benzyl	-1.29	-0.51	-0.59	-0.58	-0.52

Table 3.2 – Binding Energies with PBE functional (no van der Waals)

Binding energies (eV) ($E_b = E_{\text{Au+molecule}} - E_{\text{Au}} - E_{\text{molecule}}$) of benzyl and SnMe₃ on Au on different binding sites using vdW-optB86b functional. Total energy of molecule fragment is obtained by spin-polarized calculations.

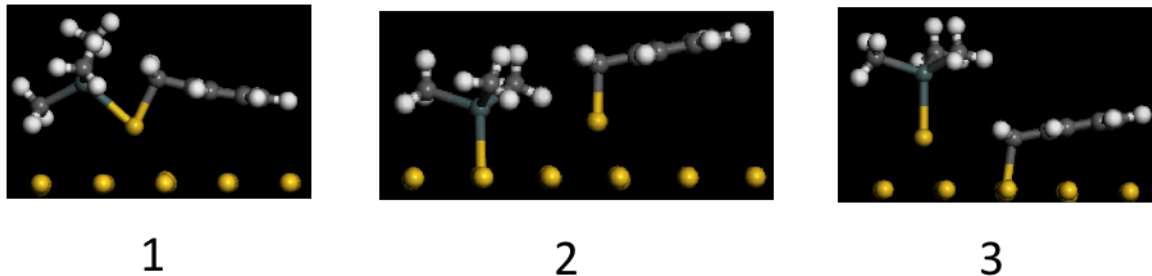


Figure 3.7 – Benzyl and trimethyltin configurations

Final configurations of benzyl and SnMe_3 bound to different sites (adatom on Au surface). Structures 1-2 are more stable than structure 3 by ~ 0.6 eV. Structure 1 is the most favorable, being ~ 0.04 eV more stable than structure 2.

To compute the minimum energy path (MEP) for the dissociation of the intact molecule on flat $\text{Au}(111)$ and $\text{Au}(111)$ with Au adatoms, we used a larger 6x6 supercell and included 4 fully-relaxed Au layers in the calculations. We have checked that the relative binding energies for the molecular fragments are essentially the same when using 4 fully-relaxed Au layers instead of 6 Au layers. For the MEP with Au adatoms, we used the climbing-image nudged elastic band (CI-NEB) method as implemented in VASP[122]. This CI-NEB method guarantees that the maximum energy in the MEP is a saddle point in the energy surface.

3.1.6.2 NEXAFS Calculations

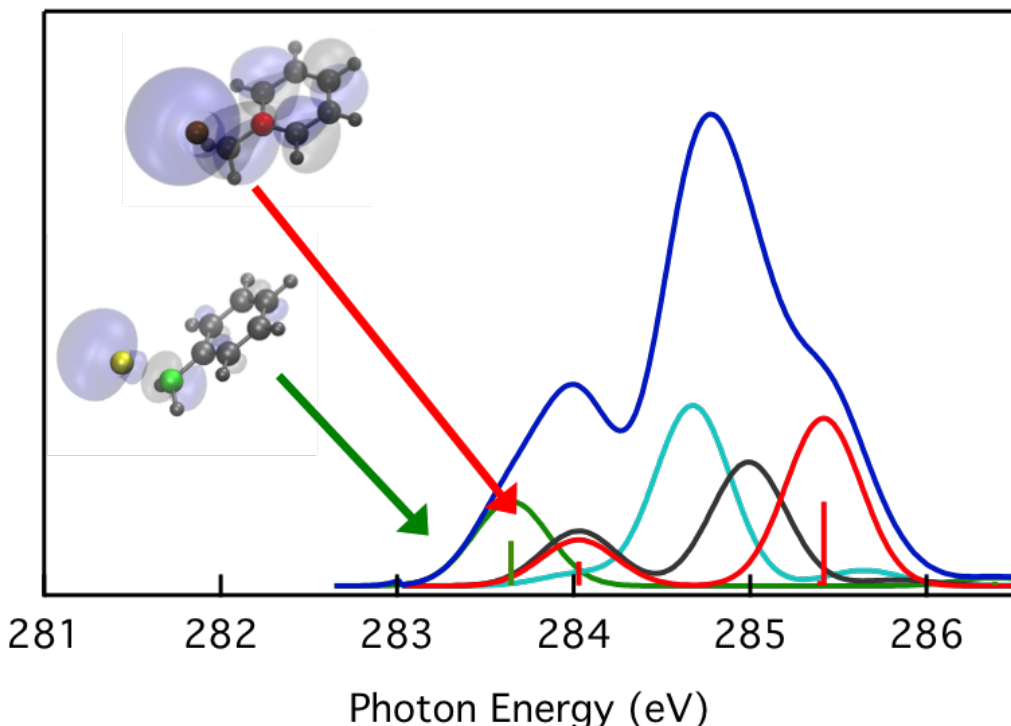


Figure 3.8 – Calculated NEXAFS spectra for Au₁-Benzyl

The main peak at 285 eV corresponds to excitation on carbon atoms on the benzene ring. The peak centered at 284 eV is a result of excitations on the benzyl carbon (green) or its nearest carbon neighbor (red).

Molecules were structurally relaxed by performing spin-unrestricted calculations using the B3LYP exchange-correlation functional and LACVP basis set using the Q-Chem software suite[70]. Default grids and convergence thresholds were used for relaxation. Subsequently, single-point calculations were carried out using B3LYP/LACVP* to calculate molecular energy levels. For NEXAFS Simulations and orbital isosurfaces of Carbon K-edge excited molecules, GPAW, a grid-based real-space projector-augmented-wave (PAW) code was employed with the B3LYP exchange-correlation functional[129]. Isolated molecules were

first relaxed to their optimized geometries, before conducting single point calculations. Default grid spacings and convergence thresholds were employed. All NEXAFS calculations were performed using the half-core-hole approximation[71].

3.1.6.3 Calculation of Stoichiometric ratios from XPS

The expected XPS signal ratio for carbon to tin is given by:

$$\frac{I_{expected,C1s}}{I_{expected,Sn3d}} = \frac{\sigma_{C1s} \cdot N_C \cdot \int_0^d \exp\left(\frac{-x}{\lambda_{C1s}}\right) dx}{\sigma_{Sn3d} \cdot N_{Sn} \cdot \int_0^d \exp\left(\frac{-x}{\lambda_{Sn3d}}\right) dx}$$

where σ is the interaction cross section for incident X-rays at 650 eV, N is the number of atoms in a molecule, $I_{expected}$ is the expected XPS intensity calculated by taking the area under the XPS peak, d is the thickness of the film, and λ is the inelastic mean free path (IMFP) of outgoing electron signal (kinetic energy dependent) due to inelastic scattering with surrounding (and overlayer) molecules. Cross section data is obtained from Yeh and Lindau[130] The IMFP is calculated using the standard formula as discussed in Cumpson and Seah[69] A calculated density of 1.327 g/cm³ is used for trimethylbenzylstannane.

3.2 Tuning Rectification in Highly Conductive Single-Molecular Diodes

3.2.1 Preface

This chapter is adapted from a manuscript entitled *Tuning Rectification in Highly Conductive Single-Molecular Diodes*, Arunabh Batra[†], Pierre Darancet[†], Qishui Chen[†], Jeffrey S. Meisner, Jonathan R. Widawsky, Jeffrey B. Neaton, Colin Nuckolls and Latha Venkataraman published in *Nano Letters*[115] ([†]equal contributors). Chemical synthesis was conducted by Qishui Chen and Dr. Jeffrey S. Meisner from Prof. Colin Nuckolls' group. Theoretical work was conducted in collaboration with Dr. Pierre Darancet in Dr. Jeffrey B. Neaton's group at the Molecular Foundry, LBNL , Berkeley, CA.

3.2.2 Abstract

We demonstrate a new method of achieving rectification in single molecule devices using the high-bias properties of Au-C bonds. Our design for molecular rectifiers uses a symmetric, conjugated molecular backbone with a single methylsulfide group linking one end to an Au electrode and a covalent Au-carbon bond at the other end. The Au-C bond results in a hybrid gold-molecule ‘gateway’ state pinned close to the Fermi level of one electrode. Through non-equilibrium transport calculations, we show that the energy of this state shifts drastically with applied bias, resulting in rectification at surprisingly low voltages. We use this concept to design and synthesize a family of diodes, and demonstrate through single-molecule current-voltage measurements that the rectification ratio can be predictably and efficiently tuned. This result constitutes the first experimental demonstration of a rationally tunable system of single-molecule rectifiers. More generally, the results demonstrate that

the high-bias properties of ‘gateway’ states can be used to provide additional functionality to molecular electronic systems.

3.2.3 Introduction

The experimental demonstration of a single-molecule diode is a first step towards the goal of creating functional molecular electronic devices, and has generated substantial interest since Aviram and Ratner first proposed their elegant design for a molecular rectifier[131]. However, experimental realizations of this[75] and other diode schemes[132, 76] at the single-molecule level have been limited by poor predictability of performance and extreme sensitivity to molecular design[133, 73]. Over the past few decades, single-molecule electronics has made significant progress in relating the chemical structure of molecules to their electronic properties[134, 135, 136]. The ongoing challenge is to create higher electrical functionality through molecular design, thus going beyond the use of molecules as merely resistive elements. The earliest proposal for such a device is the Aviram-Ratner diode[2], which involves a donor- σ -acceptor molecule connected symmetrically to two metal termini. The conceptual simplicity of this design belies some fundamental limitations[132, 73, 80]. First, the characteristics of such donor-acceptor diodes are very sensitive to the energy level alignment of the molecular orbitals with each other, and with the connecting electrodes, making experimentally predictable designs difficult[133, 79]. Second, rectification in such diodes requires a σ bridge, which effectively adds a large tunnel barrier to the backbone and results in very large junction resistance. As a result, the few experiments that have demonstrated functional single-molecule diodes all have resistances greater than $10\text{ M}\Omega$ [75, 76, 137]. To date, the only experimentally realized alternatives to donor-acceptor type diodes have been ‘many-molecule’ devices where one linker group is eliminated[138, 21] or weakened[83, 139], creating an asymmetrically

contacted junction[17, 140, 141]. These junctions do not have well defined molecular geometries and show low conductances, making measurements at the single-molecule scale difficult[132, 141]. In addition, experimental realizations of molecular rectifiers have so far operated at relatively high biases[75, 76] of >1V. In these voltage regimes, the room-temperature stability of single-molecule junctions becomes a limiting factor. To overcome these shortcomings, we have explored a new method of achieving rectification, using the electronic properties of molecular junctions with highly conducting covalent gold-carbon bonds. We demonstrate that this new family of molecular diodes exhibits high electrical conductance and high rectification at low bias, and can be efficiently and predictably tuned.

3.2.4 Experimental Methods

Our proposed rectifier design (molecule **1**, Figure 3.9a) consists of a stilbene molecular backbone with a single methylsulfide linker[11] at the 4 position (red circle), and a covalent gold-carbon bond at the 4' position (green circle), formed in-situ through the benzylic trimethyltin functionality[114] (See Supplementary Information (SI)). We measure the conductance and current-voltage characteristics of this molecule in ambient, room-temperature conditions with a scanning tunneling microscope (STM) in break-junction mode[26, 92, 107] (See SI for details). Briefly, a gold STM tip is brought into contact with a gold-on-mica substrate until a junction conductance of $>5G_0$ ($G_0 = 2e^2/h = 77.6 \mu S$) is measured. The tip is then withdrawn at a rate of 15 nm/s for 125 ms, and held at this displacement for 150 ms before being withdrawn for an additional 75 ms. During the ‘hold’ section, the applied voltage is ramped between $\pm 1V$, while current and voltage are measured simultaneously (Figure 3.9b). Due to the instability of molecular junctions at high bias at room temperature, many traces cannot sustain a stable molecular plateau

during the entire ramp, making higher bias regimes impossible. The IV procedure is repeated tens of thousands of times, with ~4% of junctions (5250 out of 131,000 traces) showing a molecular conductance signature during the IV measurement. A ‘molecular conductance signature’ is defined as a junction that sustains an unbroken conductance plateau throughout the IV ramp, and exhibits the characteristic zero-bias conductance of the molecule in the low-bias regions of the IV ramp (see SI for details). These selected IV traces are added together to create a two-dimensional histogram of absolute current against applied voltage (Figure 3.9c).

Since junctions are equally likely to form with molecules bound in ‘forward’ or ‘reverse’ orientations relative to the applied bias, any rectification is washed out in Figure 3.9c. We recover the inherent asymmetry of the junction by sorting our data into two sets, based on the magnitude of current in a range of positive biases (+0.75 to +0.80V) and corresponding negative voltages (-0.75V to -0.80V). Traces that show larger (smaller) current at positive voltages than negative correspond to molecular junctions in the forward (reverse) orientation. 2D histograms from these sorted datasets are shown in Figures 3.9d (blue, forward bias) and 3.9e (orange, reverse bias). To make a quantitative comparison of the histograms, we fit each vertical slice of the histograms to a log-normal distribution and extract the maximum value of the best-fit. These values are plotted as the black and blue IV curves in Figure 3.9d (3.9e) respectively and are also shown overlaid in Figure 3.9f. The resulting curves represent the statistically most probable IV curves for this molecule. The forward bias average IV (blue curve, Figure 3.9f) overlays the reverse bias IV (black curve), which has been mirrored in the voltage axis. Both curves show a very linear reverse bias section and a non-linear forward bias section; the near-identical shape of these curves indicates that sorting recovers the inherent structure in the IV curves without introducing significant bias. A similar sorting algorithm applied to fully symmetric molecules further

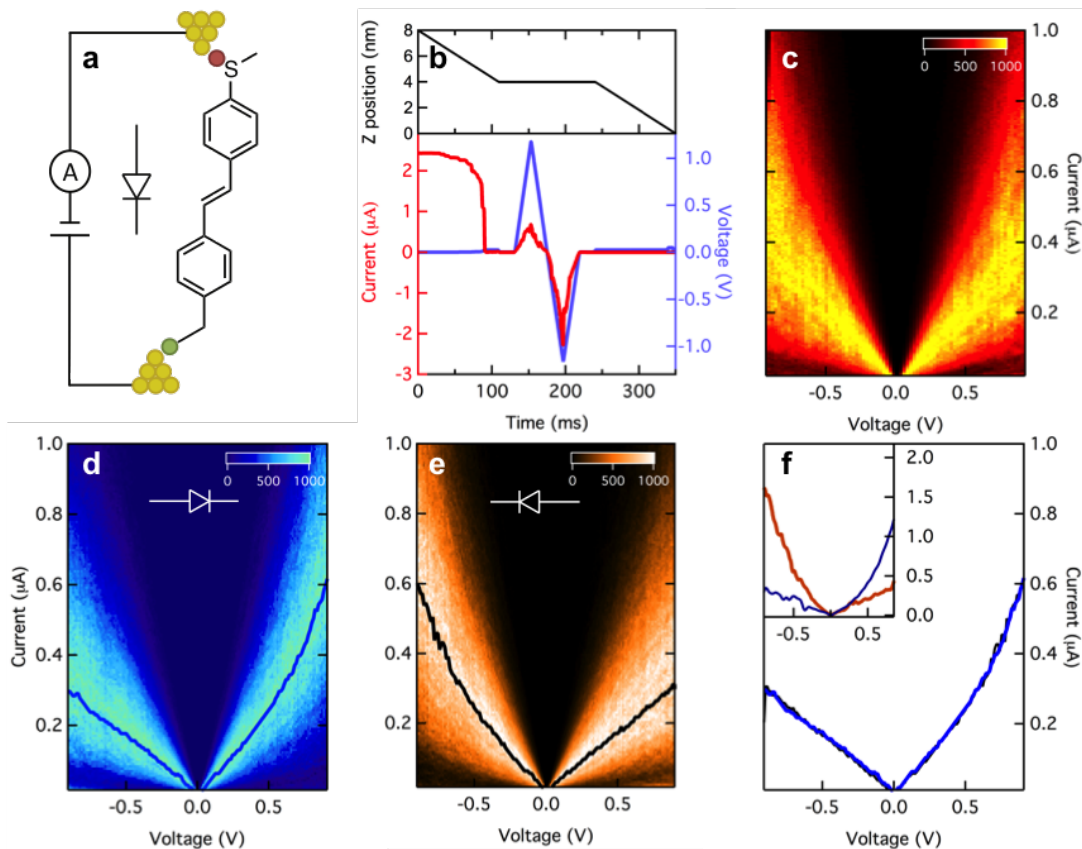


Figure 3.9 – Experimental and analytical method for current-voltage measurements
a Schematic for molecular circuit formed by molecule **1** between two gold electrodes, with the carbon-gold bond represented by a green circle and methylsulfide-gold bond represented by a red circle. A diode circuit element is shown to highlight the directional asymmetry of this circuit. **b** Representative current, voltage and displacement (z-position) traces for a single break junction measurement. The IV ramp is applied when z is held constant. **c** Two-dimensional histogram made up of thousands of traces similar to those shown in b, no asymmetry is seen because the orientation of molecule in junction is not controlled. **d** Forward bias and **e** Reverse bias two-dimensional histograms recovered from c, using trace sorting. Blue (forward) and black (reverse) line fits define average IV curves from the histogram distributions. **f** Average IV curves for d and e, overlaid with the reverse bias (black) curve mirrored across the vertical axis. Average rectification ratio is 1.7 at 0.85V. **Inset:** Example traces of highly rectifying forward bias (blue) and reverse bias (orange) junctions with rectification ratio of 3.5 and 3.3 respectively.

confirms this conclusion: the separated 2D histograms for these control molecules are identical and do not show rectification (see SI).

3.2.5 Results

Molecule **1** shows an average rectification ratio of 1.7 at an applied bias of 0.85V (Figure 3.9f), with rectification evident from ± 0.5 V and increasing linearly with increasing bias. Other reported results from single-molecule diodes[75, 76] have comparable rectification ratios, but at much higher operational voltages. We find that the maximum observed rectification in selected traces can be much higher than the statistically averaged value, as is shown in sample traces in the inset of Figure 3.9f. More evidence for junction-to-junction variation of conductance characteristics can be seen in the broad distribution of IV histograms, especially at high biases (Figure 3.9d and 3.9e). Such variability underscores the need for a statistical measure of rectification over thousands of measurements, to make a meaningful characterization of the high-bias properties of molecular junctions. Our results show that the binding orientation of a molecule in the junction can be ascertained on a trace-by-trace basis, and a statistical measure of rectification in molecules can be established despite the width of the current distributions. Molecule **1** also shows a zero-bias conductance of 5.4×10^{-3} G_0 , which is significantly higher than previously reported systems[76]; this suggests that this molecular design could be used as a basis for larger, more complex molecules (or multi-molecule circuits) that enhance functionality while maintaining an experimentally measurable current.

Next, we use ab-initio calculations to identify the mechanism behind the diode-like properties of molecule **1** when in a gold junction. We perform Density Functional Theory (DFT) based calculations with a gradient-corrected exchange correlation functional[142] and a non-equilibrium Greens' function approach[143] to optimize the molecular geometry,

the details of which have been discussed previously[114, 144]. The DFT optimized geometry for molecule **1** bound to gold electrodes with trimer tips (shown in SI) agrees well with published geometries for symmetric gold-carbon and methylsulfide linked molecular backbones[114, 145]. Bias-dependent steady-state density matrices are then calculated self-consistently using DFT by integration of the left- and right-moving scattering-states up to their respective chemical potentials, following a standard first-principles approach[146]. At zero applied bias, the left and right chemical potentials are fixed in the three outermost layers of each electrode to their bulk values. As a bias voltage V is applied to the junction, these fixed values are shifted corresponding to the opening of a symmetric bias window ($\pm eV/2$). The potential and density are computed under these constraints, and are allowed to relax in a central region including the molecule and four layers of gold on each side. The resulting potential profile across the junction is plotted in the SI. IV characteristics are calculated using the Landauer formula by integrating the bias-dependent transmission functions $T(E,V)$. The zero-bias transmission function for this junction, $T(E, V = 0)$ shown in Figure 3.10a shows a broad feature at 0.5 eV below the Fermi energy (E_F , dashed line) on the tail of the highest occupied molecular orbital (HOMO) which peaks at -1.4 eV from E_F . The lowest unoccupied molecular orbital (LUMO) is far from E_F (1.8 eV) and is not important to conduction within the experimentally accessible bias window. Although resonance energies are expected to be underestimated relative to experiment[147], we find that DFT is a sufficient level of theory for understanding rectification in these systems.

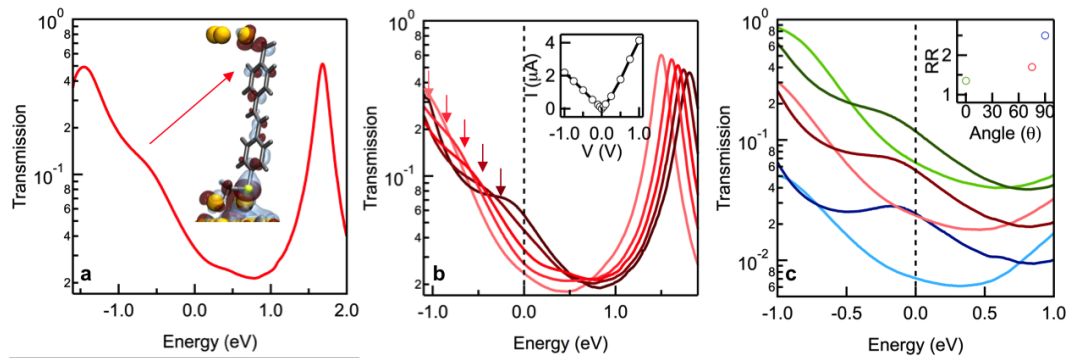


Figure 3.10 – Calculated transmission functions and IV curves

a DFT calculated transmission function at zero bias, $T(E,V=0)$ for molecule **1**. Arrow indicates position of eigenchannel corresponding to gold-carbon gateway state at -0.5 eV. Dashed line at 0 eV indicated zero-bias Fermi energy for both electrodes. Inset: isosurface plot of the upward moving scattering for the gateway state, showing significant contribution on the carbon-gold bond. **b** Transmission for molecule **1** as a function of applied bias of -1V (light red) to +1V (dark red) in increments of 0.5V. Arrows point to the gateway state positions at each bias. Dashed line at 0 eV indicates average of left and right chemical potentials. **Inset:** IV curve obtained by integrating $T(E,V)$, showing a rectification ratio of 1.8 at 0.85V. **c** Transmission at -1V (dark) and +1V (light) for analogs of molecule **1** with methylsulfide torsional angle $\theta=0^\circ$ (green) and $\theta=90^\circ$ (blue) compared to equilibrium geometry (red) which has $\theta=73^\circ$. **Inset:** DFT-calculated rectification ratio as a function of methylsulfide torsion angle.

An isosurface plot of the eigenchannel wavefunction at -0.5 eV (inset of Figure 3.10a) shows a ‘gateway’ state derived from the molecular orbital on the gold-carbon bond that is strongly hybridized with molecular π backbone and gold electrode[114, 97]. A comparison of transmission functions under an applied bias of -1V to +1V in steps of 0.5 V is shown in Figure 3.10b. We see that the gateway state moves with the chemical potential of the electrode towards E_F under positive bias (dark red curve) and away from E_F for negative bias (light red curve). At every applied bias, the gateway state is largely ‘pinned’ to E_F and moves by 75% of the shift in chemical potential of its adjacent electrode. This shift is not observed for intrinsic molecular resonances, such as the LUMO, which only shifts by 20% of the electrode potential. The high degree of tunability of the pinned gateway state with bias compared to intrinsic molecular orbitals suggests that efficient rectification at

low-bias is achieved by bringing a density of states into or out of the bias window. The large shift seen for the gateway state is a result of strong gold-carbon hybridization, which leads to a high polarizability and relatively flat potential profile near the gold-carbon bond under bias (see SI). The calculated IV curve for this junction (inset, Figure 3.10b) is asymmetric with a rectification ratio of 1.8 at 0.85V, very close to the experimental value of 1.7. While the magnitude of computed current is somewhat overestimated (as expected from DFT-based transport calculations)[144], the much smaller error in the position of the gateway state due to its relatively strong coupling to the electrodes[97] leads to striking agreement between the experimental and theoretical rectification ratio. Our calculations indicate that rectification in molecule **1** is a consequence of the gateway modulation, and suggests that higher rectification ratios can be achieved by tuning the response of this state to bias.

3.2.6 Tuning Rectification

To explore the tunability of this molecular diode design, we develop a tight-binding model to identify parameters that govern rectification ratio (see SI). A similar theoretical approach has previously been used to explain negative differential resistances in atomic wire junctions using carbon-nanotube electrodes[148]. Our model suggests that the coupling between the two sides of the molecule plays an important role in the shape and high-bias shift of the gateway state. In particular, our model predicts that rectification ratio should increase as the coupling between the backbone π -system and the methylsulfide linker decreases (see SI). We explore the possibility of tuning the coupling by varying the carbon-sulfur-gold torsional angle ϑ between the backbone π -system and the methylsulfide linker of molecule **1**[89]. We perform DFT calculations on two analogs of molecule **1**, with the methylsulfide linker constrained parallel ($\vartheta=0^\circ$) or perpendicular ($\vartheta=90^\circ$) to the plane of the stilbene backbone.

Figure 3.10c compares the resulting high bias transmission functions, $T(E, V=+1V)$ and $T(E, V=-1V)$ for the three structures. All three clearly show the presence of a gateway state close to E_F , which moves under an applied bias. The structure with $\vartheta=0^\circ$, which yields the highest gateway-backbone coupling, has the lowest rectification (1.3); in contrast, the structure with $\vartheta=90^\circ$, which has the lowest intramolecular coupling, exhibits a significant rectification ratio of 2.6.

Having established the mechanism for rectification and a route for its optimization, we now design molecules to experimentally test these predictions. The methylsulfide linker in our original rectifier provides a convenient method of achieving this goal. The coupling of the π -system through the gold-sulfur donor-acceptor bond varies with their relative orientation[89], and control of this relative orientation should therefore result in tunable rectification. In Figure 3.2.6a, we show two molecules with better (**2**) or worse (**3**) π -gold-sulfur coupling than **1** based on their chemical structures. The methylsulfide group in **2** is locked in-plane with the molecular backbone through the saturated six-membered ring. This ring orients the methylsulfide group nearly parallel to the backbone's π -system and gives near maximal coupling of the gold-sulfur bond to the backbone, analogous to the $\vartheta=0^\circ$ structure discussed earlier. Molecule **3** has a phenylsulfide replacing the methylsulfide group, which decreases the electronic coupling across the sulfide linker when compared with **1**[89].

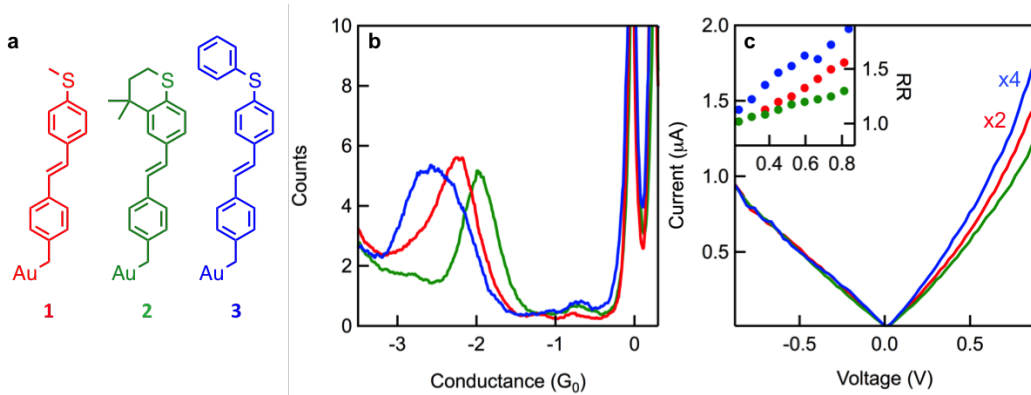


Figure 3.11 – Tuning rectification through molecular design

a Chemical structures for the original molecular rectifier design (molecule **1**), along with two modified designs, **2** and **3**. All three structures have the same backbone and gateway, and differ only the in geometry of the sulfide linker. **b** Log-binned conductance histograms for the three molecules. The decreasing conductance, **2** > **1** > **3** reflects the decreasing coupling between backbone and sulfur-gold bonds formed by the three sulfide linkers. **c** Scaled, statistically most probable IV curves for the three molecules. The curves are calculated from log-binned 2D histograms with bin sizes and histogram ranges kept constant. All curves have been scaled to zero-bias conductance of molecule **3**, with the red curve multiplied by 2 and the blue curve by 4. **Inset:** Rectification ratio as a function of bias.

Our measurements of the zero-bias conductance ($V_{\text{applied}} < 100 \text{ mV}$) show that molecules **2** and **3** conduct higher and lower than molecule **1** (Figure 3.2.6b), and confirm that we are able to tune coupling between the backbone and gold-sulfur bond through chemical modifications. The scaled IV curves for this family of molecules (Figure 3.2.6c) show a linear reverse bias regime for all three molecules, which results from a relatively flat transmission function within the integration window, consistent with the observation that the gateway is moving away from E_F . On the forward bias side, the curves are all nonlinear, with **3** (blue) showing the most curvature due to the influence of a more prominent gateway state. For each of these curves, we determine a rectification ratio as a function of applied bias by dividing forward bias current with the corresponding reverse bias current (inset, Figure 3.2.6c). For all three molecules, rectification increases linearly with applied bias, with significant asymmetry seen as low as $\pm 0.5 \text{ V}$. The molecule with

the poorest coupling, **3**, rectifies the most, while **2**, with the strongest coupling rectifies the least. More importantly, we have demonstrated that by increasing the methylsulfide torsion angle, we can increase the asymmetry in the measured IV curves by over a factor of 3. This is experimental verification of a rationally designed family of rectifiers whose asymmetry can be tuned by varying a single parameter through chemical design.

The results presented in this paper introduce a new mechanism for rectification based on the electrostatic modulation of a gold-carbon gateway state. The relative simplicity of this mechanism is highlighted by the fact that rectification can be tuned through molecular design. The tunability of this design combined with the low operational voltages and high zero-bias conductances achieved can facilitate future designs that optimize performance with larger, more complicated chemical structures. More broadly, our results establish localized gateway states as a design element whose unique high-bias properties can be integrated into existing molecular structures to create new functionality.

3.2.7 Supplementary Information

Experimental Methods and Data Selection For Synthesis details, see Reference [74].

Conductance and IV Measurements Molecular conductance is measured by repeatedly forming and breaking gold point contacts in a solution of molecules with a custom Scanning Tunneling Microscope (STM)[93]. A freshly cut gold wire (0.25 mm diameter, 99.999% purity, Alfa Aesar) is used as the tip, and UV/ozone cleaned gold substrate (mica with 100 nm gold, 99.999% purity, Alfa Aesar) is used as the substrate. The STM operates in ambient conditions at room temperature, and the junctions are broken in dilute (1mM to 10mM) solutions of molecules in 1,2,4-trichlorobenzene (Sigma-Aldrich, 99% purity). Before adding a molecular solution, 1,000 conductance traces are first collected to ensure that there are no contaminations in the STM set-up. Current-voltage (IV) measurements

are carried out using previously published methods[92]. Briefly, the STM tip is brought into contact with the substrate until a junction conductance of $>5G_0$ ($G_0 = 77.6 \mu\text{S}$) is measured. The tip is then withdrawn at a rate of 15 nm/s for 125 ms, and held at this displacement for 150 ms before being withdrawn for an additional 75 ms. During the ‘hold’ section, the applied voltage is ramped between $\pm 1\text{V}$, while current and voltage are measured simultaneously (Figure 3.9b in the main text). Traces that show a molecular signature through the entirety of the IV ramp are selected as successful IV traces. In general, 1-10% of measured junctions are selected from $\sim 50,000$ measured traces per experiment. Data from multiple experiments is added together to form the histograms shown in the main text, with each histogram containing >2000 successful IV traces.

Data Selection and Sorting The procedure for selection of successful IV traces is shown in Figure 3.12a. As mentioned in the main text, each recorded trace contains a 150 ms ‘hold’ section, where the tip-substrate separation is kept fixed while the tip-substrate voltage is ramped. Since not all recorded traces include a conductance plateau corresponding to the molecule, data selection is performed on select traces with a molecular conductance signature that is stable before and after the application of an IV ramp. Average conductance is calculated 25ms before (G_{pre}) and after (G_{post}) the IV ramp, and for 10ms at the middle of the ramp (G_{mid}). At these portions of the trace, the junction is in zero-bias conditions ($V_{\text{applied}} < 100 \text{ mV}$). Selected curves must have $G_{\text{pre}}, G_{\text{post}}$ and G_{mid} within the full-width at half maximum (FWHM) of the peak in the conductance histogram measured at low bias. This procedure typically selects between 1-10% of measured traces, which can then be used to make two-dimensional (2D) IV histograms using either linear or log binning. Figure 3.9c in the main text shows an example of such a 2D histogram using linear binning.

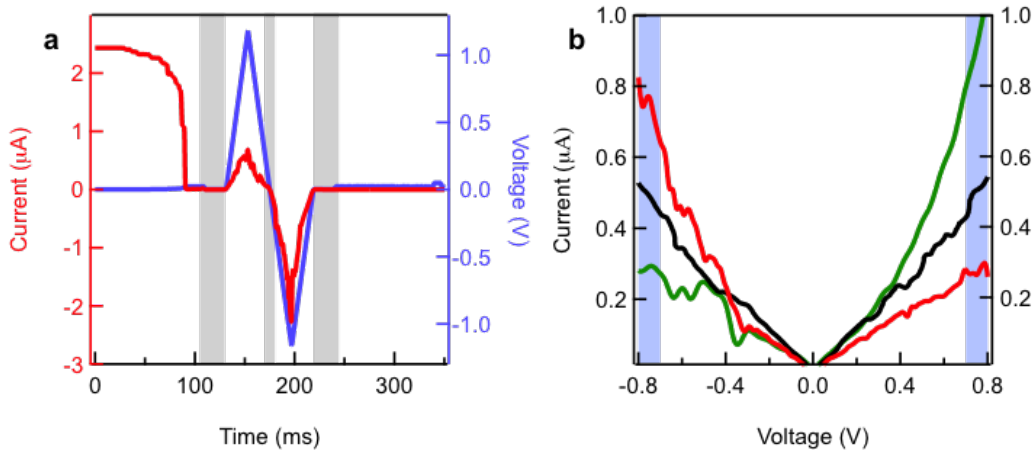


Figure 3.12 – Data selection and sorting methods

a Sample trace showing measured current (red) and applied voltage (blue) on a molecular junction. A trace is considered a stable molecular junction if measured conductances before, during and after voltage ramp (shaded regions) are at the characteristic zero-bias conductance of the molecule. **b** The presented sample IV curves are representative of the three types of IV curves, forward bias (green), reverse bias (red), and non-rectifying (black). IV curves are sorted by comparing magnitudes of average current (I) at positive and negative biases (blue shaded regions).

Selected data can be sorted (all selected traces are used) based on magnitude of current at positive and negative voltages, resulting in separated histograms shown in Figure 3.9d and 3.9e in the main text. The data sorting procedure is outlined in Figure 3.12b. Measured current is averaged between +0.75 V and +0.80 V (I_{pos}) and -0.75V to -0.80V (I_{neg}). If $abs(I_{pos}) > abs(I_{neg})$, the junction is considered to be in the forward bias condition, and vice versa. Based on this selection process, the data are sorted into two 2D histograms (such as Figure 3.9d and 3.9e) that are then used to obtain a ‘statistically most likely’ (hereafter called average IV curve) IV curve for forward and reverse bias conditions. The results of sorting do not change appreciably if the voltage selection window (blue shaded regions in Figure 3.12b) is widened or moved to slightly lower or higher ranges. The three example traces shown in Figure 3.12b are characteristic of IV curves observed

in experiments. In this case, the green curve and red curve are selected into forward and reverse bias histograms respectively. Symmetric IV curves like the black curve are also observed, where the rectification ratio is comparable to stochastic variability of junction conductance. These traces are equally likely to be in the forward or reverse bias histograms and do not significantly change the resulting 2D histograms.

Obtaining Statistically Most-Likely IV Curves ‘Average’ IV curves are obtained by fitting the distribution of currents at each voltage bin of a histogram (i.e. a vertical ‘voltage slice’ of a 2D IV histogram) to a log-normal (log-binned 2D histograms) or Gaussian (linear-binned 2D Histogram) curve; the peak of this curve represents the statistically most likely current for that voltage. This procedure is repeated for each voltage slice to generate an average IV curve (like those shown in Figure 3.9f). Whenever a comparison is made of IV curves between different molecules with varying conductances, it is preferable to bin current values on a logarithmic scale, while maintaining linear scaling for voltage bins. This binning scheme allows the histograms of all compared molecules to have the same ranges and bin-widths, making quantitative comparisons easier. IV curves shown in Figure 3.2.6 follow this logarithmic current binning procedure.

Control Molecules Molecules **S1**, **S2** and **S3** (Figure 3.13a) are symmetrically linked with methylsulfide linkers corresponding to the diodes **1**, **2** and **3**. The low-bias conductance histograms of the three molecules (Figure 3.13b), show that conductance of **S2 > S1 > S3**, similar to the trend observed in the corresponding asymmetric diodes. Figure 3.14a and 3.14b show IV histograms for molecule **S2** without and with the sorting procedure applied. We extract averaged IV curves for sorted molecules (red curves in Figure 3.14c), and compare with unsorted data (blue curve). The rectification ratios recovered is 1.2, which is much smaller than those found for asymmetric diode designs. The small rectification is

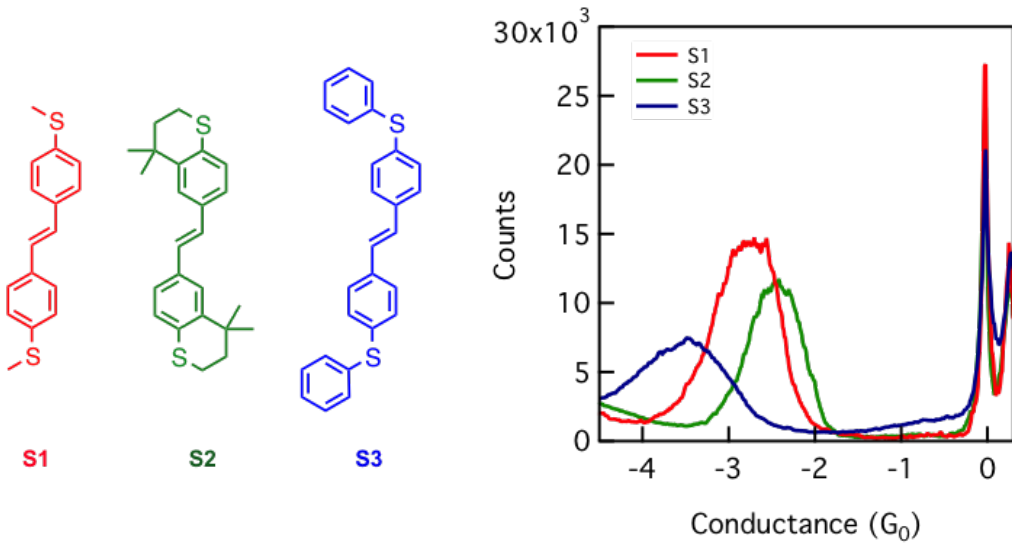


Figure 3.13 – Symmetric Control Molecules

a Chemical structures of symmetrically linked versions of rectifiers **1,2**, and **3** **b** Zero-bias conductance histograms of molecules **S1**, **S2**, and **S3**, showing that conductance of **S2**>**S1**>**S3**

possibly due to junction-to-junction variability in the asymmetry of the coupling of the molecule to the two electrodes.

3.2.7.1 Density Functional Theory

Calculation Details We use Density Functional Theory (DFT) as implemented in the SIESTA package[149, 150]. Self-consistent charge densities are obtained with localized numerical orbitals and a 300 Ry grid cutoff, a 0.05 eV electronic smearing, on a 4x4 k-point sampling in directions perpendicular to the junction. Hellmann-Feynman forces on the atoms are reduced to 0.04 eV/Å or less using a GGA-PBE[142] functional using a double- ζ -basis set. We use a motif consisting of 3 gold adatoms (trimer) on both sides connected to 7 layers of 16 gold atoms on either side, the last 4 layers being constrained to the bulk (PBE) geometry. Initial junction geometries for molecule **1** are chosen from previous work on carbon-gold bonded[114] and methylsulfide-bonded[89] molecules linked to under-coordinated gold. Angular dependence of the analogs of molecule **1** (Figure 3.15)

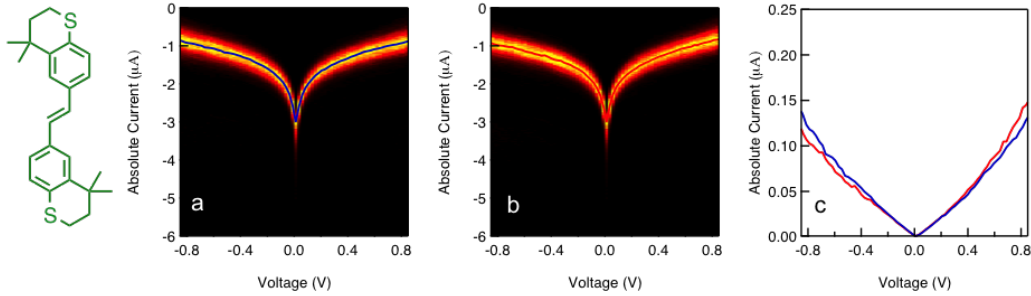


Figure 3.14 – Curves for Symmetric Control Molecules

a Log-binned two dimensional IV curve histograms for molecule **S2** (drawn in green) as measured (unsorted). The blue line is a best fit, representing the statistically most likely IV curve. **b** The same data as Figure 3.15a, now sorted by rectification direction of each trace. Traces showing higher current at negative biases are reflected about the y-axis. The red curve shows the statistically most likely IV curve after sorting. **c** Comparison of unreflected (blue) and reflected (red) curves for molecule **S2** on a linear scale, showing that neither red nor blue curves show much rectification (< 1.2 at 0.85 V), as expected for a symmetric molecule.

are obtained by fixing the dihedral angle of gold-carbon-phenyl to the desired values, and, and then repeating the optimization procedure. Obtained geometries are shown in Figure 3.15.

Procedures for Density matrices and Transmission We obtain the zero- and finite-bias density matrices using a parameter-free scattering-state approach based on DFT as implemented in the SCARLET package[146]. Isosurface plots of the eigenchannel wavefunctions corresponding to the major maxima in the transmission function are shown in Figure 3.16. Following previous works[144, 151, 152], we determine the zero-bias conductance and IV characteristics from the Landauer formula. Junction geometries consist of 7 layers of 16 gold atoms on both sides. Densities and potentials are fixed to their bulk values in the 4 outermost layers on each side, and allowed to vary elsewhere. We obtain the self-consistent steady-state density matrix from DFT-PBE[142] as described in Darancet, et al. [144] using an 8×8 k_{\parallel} -mesh. For finite bias calculations, the density

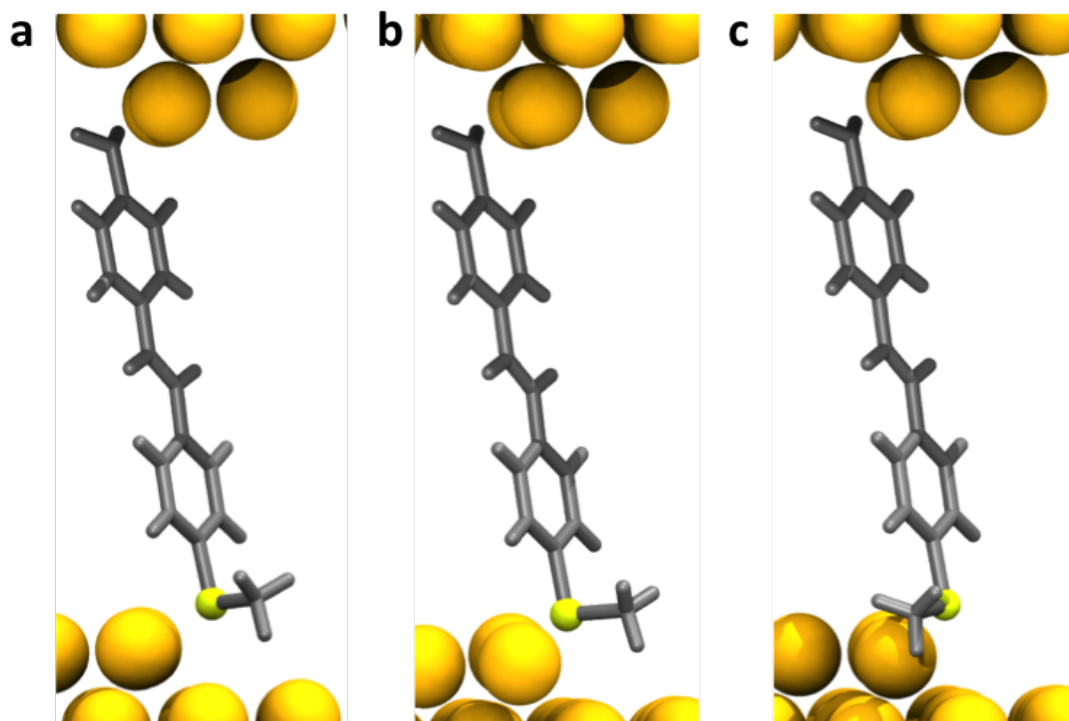


Figure 3.15 – DFT Optimized Geometries

a Equilibrium geometry for molecule **1** connected in a junction with trimer tips. The torsional angle for the methyl-S-C-C bond is $\theta=73^\circ$. **b** constrained geometry with methyl group on the methylsulfide linker pointing out of the plane of the stilbene backbone ($\theta=90^\circ$) **c** methyl group constrained to be in plane ($\theta=0^\circ$)

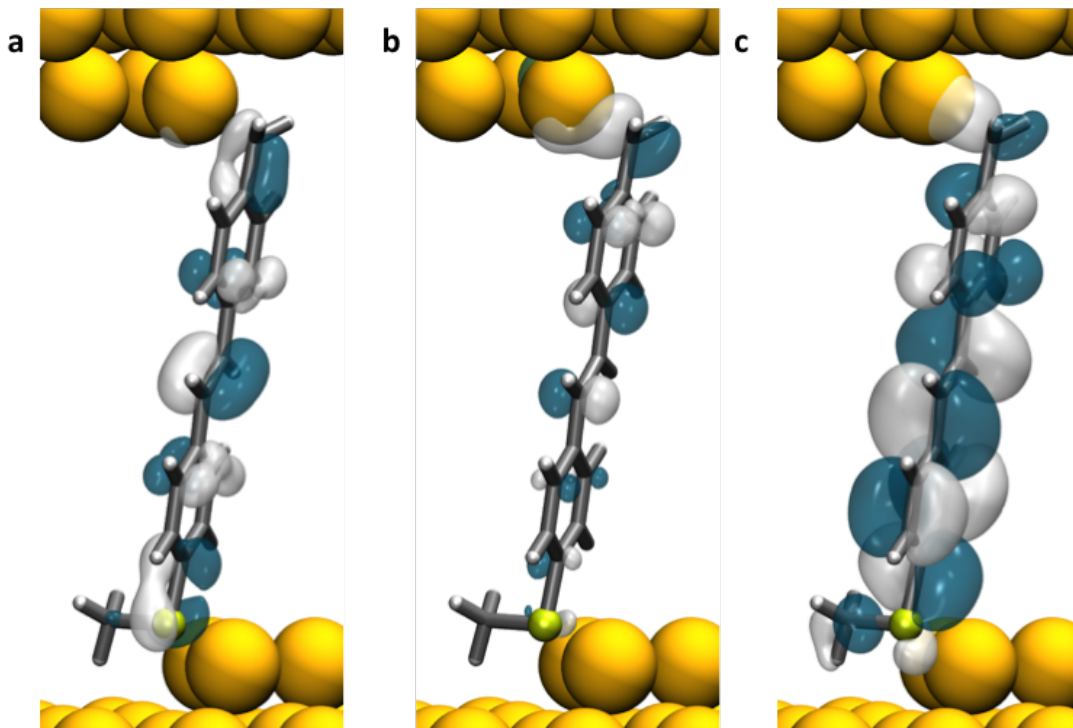


Figure 3.16 – Scattering states for molecule 1

Iisosurface plots of eigenchannel wavefunctions for molecule **1** at **a** -1.4 eV (HOMO), **b** E_F , and **c** 1.8 eV (LUMO). The scattering state at E_F has both ‘gateway’ state character and molecular orbital character, indicating the strong coupling between the gold-carbon bond and the backbone.

matrix includes a real axis integration of the scattering-states in the bias window on an adaptive energy grid with a resolution of up to 10^{-7} eV in the vicinity of the molecular resonances. For all junctions and biases, the bias-dependent transmission functions are subsequently calculated using a $16 \times 16 k_{\parallel}$ -mesh and an 800-point energy grid in the energy range ($E_F - 2$ eV, $E_F + 2$ eV). The current at a given bias is obtained through integration of the corresponding transmission function between the leads’ chemical potentials. Changes in the geometries upon application of bias are neglected.

The Hartree potential for the junctions under bias is calculated by solving a Laplace equation with boundary conditions given by the Hartree potential of the bulk shifted by $\pm V/2$. The potential profile is obtained by subtracting the finite-bias Hartree potential

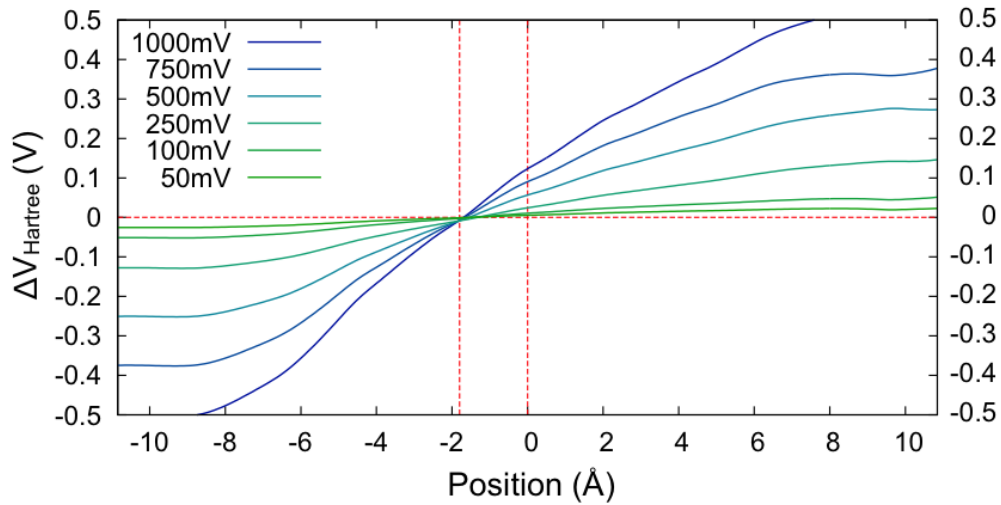


Figure 3.17 – Potential profile for molecule **1** at 50mV to 1V

The potential drop in the molecular region -6\AA to 6\AA is non-linear and inhomogeneous at all biases. These profiles are calculated taking the differences in the self-consistent Hartree potentials at finite bias with respect to the zero-bias case, and averaging them in the x and y directions. The two vertical dashed lines point to asymmetry in junction The position along the z-direction is indicated with respect to the mid-point of the gold electrodes' first layers.

from its zero-bias counterpart. Figure 3.17 shows such potential profiles averaged in the x and y directions for different biases for a junction involving with molecule **1**, where the potential drop across the junction is non-linear and asymmetric in the molecular region (position from -6\AA to 6\AA). As shown in Figure 3.17, the lineshape of the potential drop is bias-independent (50mV to 1V) and is a consequence of a relatively large and inhomogeneous dielectric response function of the molecule in the junction.

Figure 3.18 shows the potential profile at 750mV as compared with the structure of the junction. 60% of the potential drops on the methylsulfide moiety while the potential is essentially flat in the carbon-gold region (10% decrease at this contact, 23% at the methylsulfide contact). This indicates a relatively higher local polarizability of the carbon-gold moiety. It is worth noting that such non-linearities and inhomogeneity in the potential drop do not appear when the molecule is in the gas-phase and are a consequence of strong

hybridization of the molecule with the gold electrode through the carbon-gold bond.

3.2.7.2 Tight Binding Model

All tight-binding calculations are conducted using a bias dependent two-site model Hamiltonian H of the form

$$H(V) = \begin{bmatrix} \varepsilon_0 + \alpha_0 eV & \tau \\ \tau & (\varepsilon_1 + \alpha_1 eV) \end{bmatrix}$$

, where ε_0 is the on-site energy of the molecular orbital connected to the electrode via the carbon-gold bond , and ε_1 is the on-site energy of the orbital coupled to gold through the sulfur-gold bond. Due to the very good coupling between the gold-carbon and π -system (shown in the scattering states of the main text and SI), state 0 can be understood as a linear combination of orbitals lying on the π -system (backbone) and the gateway on the gold-carbon bond, while state 1 corresponds to the methylsulfide group. α_0 and α_1 are the corresponding dimensionless constants controlling the change in the on-site energy upon application of a bias. Following Darancet, et al. [144], for orbitals breaking inversion symmetry, we approximate this change by its first order variation (linear stark shift) with applied bias. τ represents the coupling between states 0 and 1 and is therefore seen as the coupling between the left and right side of the junction.

A schematic representation of the model is shown in Figure 3.18a. Retarded Green's functions, i.e. $G(E, V) = [E - H(V) - \Sigma_L - \Sigma_R]^{-1}$ are generated from this Hamiltonian, where $\Sigma_{L,R}$ are the self-energies of the left and right electrodes. We simplify our system by assuming that the self-energy matrices are energy independent, and that the real parts

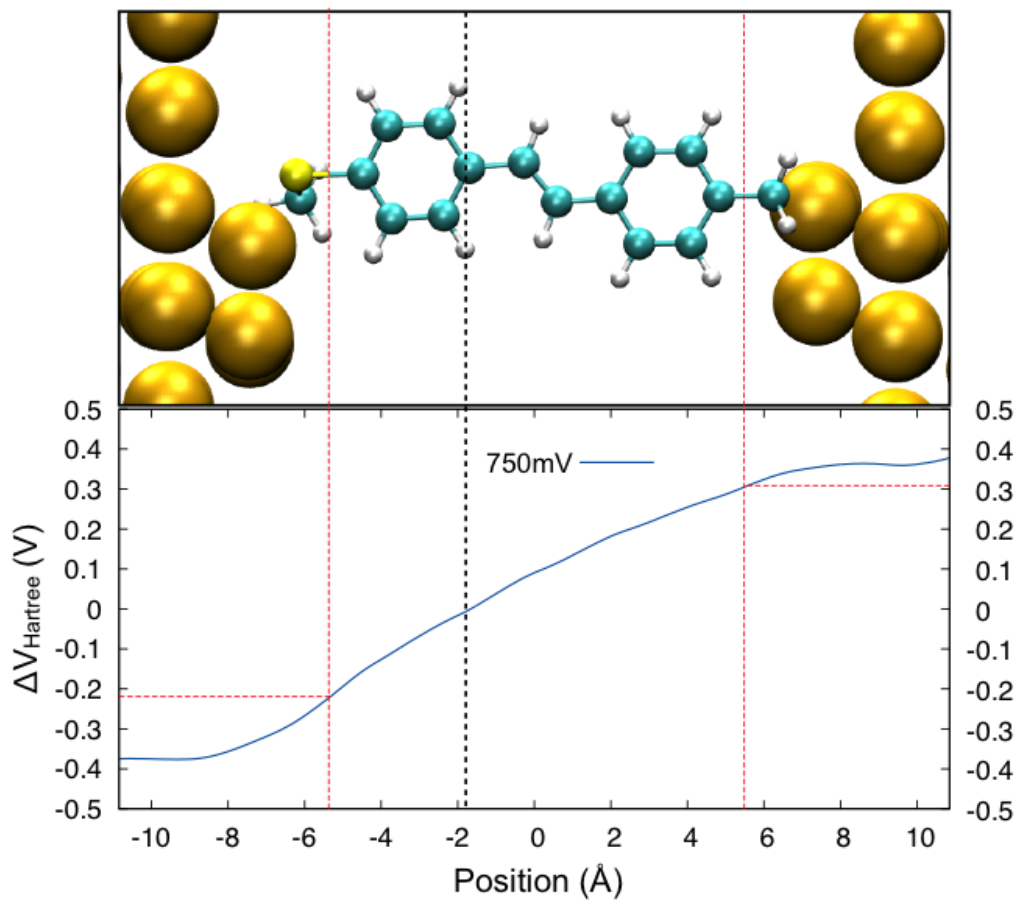


Figure 3.18 – Potential profile across molecular diode

The potential profile is shown for molecule **1** in a junction with 750 mV bias. The red dashed lines indicate midpoints of sulfur carbon-bond and carbon-carbon bonds. The voltage drop at the midpoint of the sulfur-gold bond is over two times more than that at the midpoint of carbon-carbon bond on the carbon-gold bound side. The black dashed line near the center of the plot shows the zero potential point, which is shifted towards the methylsulfide side of the molecule

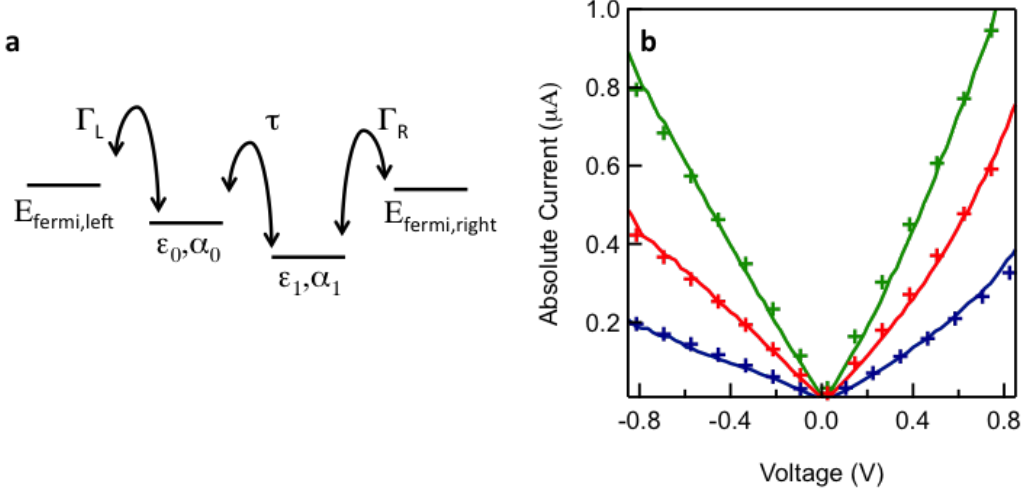


Figure 3.19 – Tight binding model for rectifiers

a Two site tight-binding model to identify parameters controlling rectification. See text for parameter definitions **b** IV curves for molecules **1, 2** and **3** (solid lines). Overlaid markers represent model IV curves that show good agreement with the data. Parameters for the model curves are listed in Table 3.3.

of the self-energies are negligible[6]. The effective Green's function then becomes:

$$G(E, V) = \begin{bmatrix} E - \varepsilon_0 - \alpha_0 eV + i\frac{\Gamma_1}{2} & \tau \\ \tau & E - \varepsilon_1 - \alpha_1 eV + i\frac{\Gamma_2}{2} \end{bmatrix}^{-1}$$

where Γ_L and Γ_R are the coupling strengths of the molecular levels to left and right Au electrodes, respectively. The transmission is then given by $T(E, V) = [\Gamma_L G(E, V) \Gamma_R G(E, V)^\dagger]$. Initial guesses for the parameters are taken from previous work on modeling gold-carbon bond linkers[114, 97], methylsulfide-gold contacts[89], and DFT based transmission calculations presented for molecule **1** in the main text. The parameters are then optimized to match the zero bias conductance for molecule **1**; see Table 3.3 for parameters used in this work. Next, IV curves are generated using the Landauer formula, $I(V) = \frac{2e}{h} \int dE \cdot T(E, V) \cdot [f(E + eV/2) - f(E - eV/2)]$ where f is the Fermi distribution function. Further parameter optimization is performed to match $\frac{dI}{dV}$ and $\frac{d^2I}{dV^2}$ characteristics of the

experimental IV curve from molecule **1**. The resulting fit (red markers, Figure 3.18b) show that the model captures the essential features of the experimental IV, including the linearity of the reverse bias region and the nonlinearity of forward bias. Varying the model parameters suggested that τ , the coupling between the left and right side of the molecule, is a critical parameter in controlling rectification ratio. This understanding allowed us to develop synthetic methods of achieving this goal, resulting in designs for molecules **2** and **3**. The experimental results from IV measurements on molecules **2** and **3**, are also well captured by changing three parameters, using the zero-bias conductance and $\frac{dI}{dV}$ and $\frac{d^2I}{dV^2}$ of experimental IV curves as fitting parameters. The resulting fits to the IV curves are shown in Figure 3.18b, with tight-binding calculated transmission functions shown in Figure 3.19. The parameters used for these results are tabulated in Table 3.3.

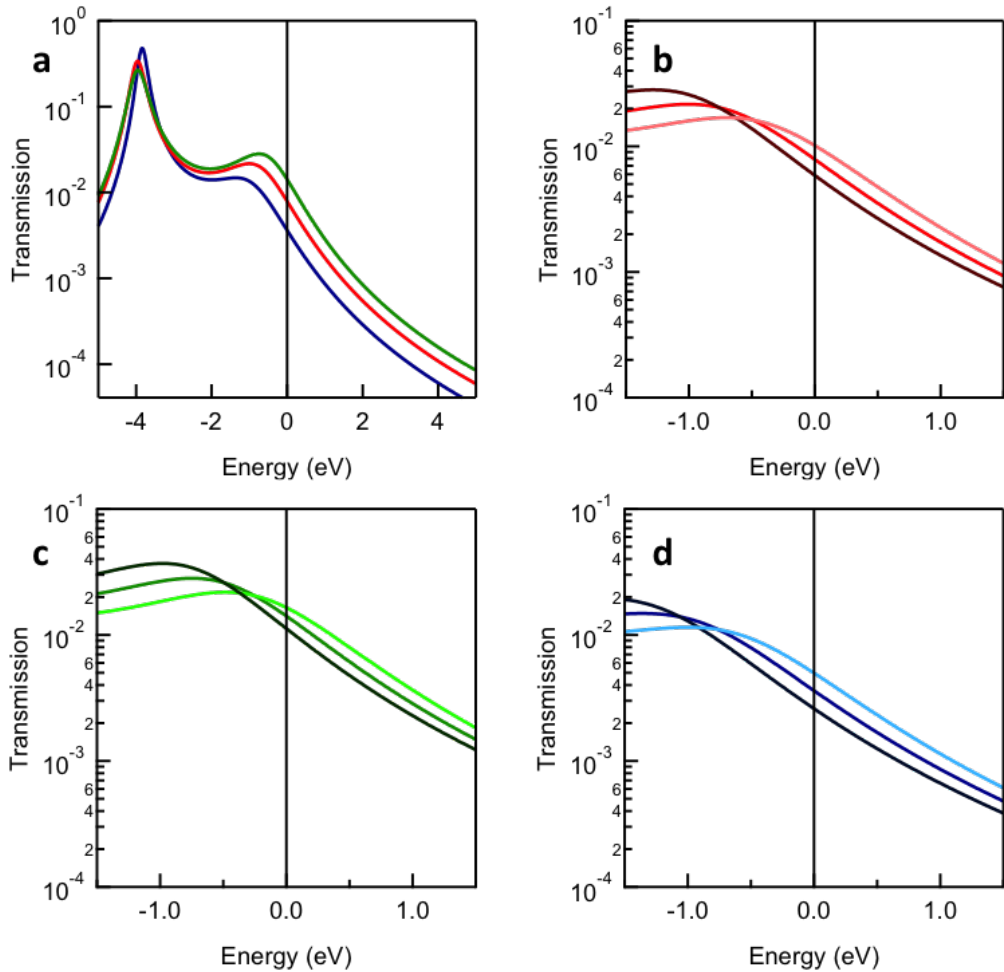


Figure 3.20 – Transmission Curves from Tight Binding

a Zero-bias transmission functions, $T(E, V=0V)$ calculated from the tight binding model described in Figure 3.15. Red, green and blue curves represented transmission functions calculated for molecules **1**, **2**, **3** respectively. **b,c,d** show a zoomed in view of $T(E,0V)$, along with $T(E,+1V)$ (lighter color) and $T(E,-1V)$ (darker color). The gateway is seen to move with bias for all three biases, but is most prominent for d, which corresponds to molecule **3**. Thus, the model predicts highest rectification for this molecule

Variable	Molecule 1	Molecule 2	Molecule 3
Γ_L	2.1	2.1	2.1
ε_0	-1.3	-1.3	-1.3
τ	1.3	1.5	1.0
ε_1	-3.4	-3.2	-3.5
Γ_R	.045	.045	.045
α_0	-0.35	-0.35	-0.35
α_1	0.05	0.10	0.00

Table 3.3 – Parameters for tight binding model

Parameters are defined in the text. Shaded cells show parameters that have been varied across molecules **1**, **2**, and **3**. ε_1 , τ , α_1 are assumed to change systematically with coupling, with ε_0 coming closer to E_F with increasing coupling, and τ and α_1 increasing with increasing coupling.

Chapter 4

Self-Assembly of Molecular Electronic Components

4.1 Probing the Mechanism for Graphene Nanoribbon Formation on Gold Surfaces through X-ray Spectroscopy

4.1.1 Preface

This chapter is adapted from a manuscript entitled, *Probing the Mechanism for Graphene Nanoribbon Formation on Gold Surfaces through X-ray Spectroscopy*, by Arunabh Batra[†], Dean Cvetko[†], Gregor Kladnik, Olgun Adak, Claudia Cardoso, Andrea Ferretti, Deborah Prezzi, Elisa Molinari, Alberto Morgante and Latha Venkataraman ([†]equal contributors). The experimental work was conducted at the ALOISA Beamline at the Elettra Synchrotron in Trieste, Italy, in collaboration with Prof. Dean Cvetko, Dr. Gregor Kladnik, and Prof. Alberto Morgante. Theoretical work was conducted in collaboration with Dr. Claudia

Cardoso, Dr. Andrea Ferretti, Dr. Deborah Prezzi and Dr. Elisa Molinari at the University of Modena, Modena, Italy.

4.1.2 Abstract

We study the formation of graphene nanoribbons (GNRs) via the self-assembly of 10,10'-dibromo-9,9'-bianthryl precursor molecules on gold surfaces with synchrotron spectroscopies. Through x-ray photoemission spectroscopy core-level shifts, we follow each step of the synthesis process, and show that Br-C bonds on the precursors cleave at temperatures as low as 100 C on both Au(111) and Au(110). We establish that the resulting radicals bind to Au, forming Au-C and Au-Br bonds. We show that polymerization of precursors follows Br desorption from Au, suggesting that the presence of halogens is the limiting factor in this step. Finally, with angle-resolved ultraviolet photoemission spectroscopy and Density Functional Theory we show that GNR/Au interaction results in an upshift of the Shockley surface state of Au(111) by ~ 0.14 eV, together with an increased electron effective mass.

4.1.3 Introduction

The creation of functional nanoscale electronic devices from molecular components requires a bottom-up approach based on synthetic chemical control to ensure reproducibility of structure and function. Graphene nano-ribbons (GNRs) have been proposed as ideal components for such devices[153]. The covalent self-assembly of GNRs on metal surfaces from molecular building blocks is a promising approach towards this goal[154], since it allows experimental control over the electronic structure by control of width[155], shape and chemical composition[156]. The chemical mechanism underlying this self-assembly process is the halogen-mediated Ullman coupling reaction[157]. GNRs are formed by

deposition and annealing of a halogen-bearing molecular precursor (Figure 4.1a) on a metal (Ag or Au) surface in ultra-high vacuum (UHV). The proposed mechanism[154, 120] for the ribbon formation breaks the reaction into three steps: first, the halogen (typically Br or I) cleaves leaving a surface-stabilized radical precursor. Next, driven by an annealing step, the radical precursors diffuse and polymerize. Finally, a high-temperature annealing step allows for cyclo-dehydrogenation resulting in the formation of C-C bonds and flat GNR structure.

Here, we focus on GNRs created using brominated precursor molecule, 10,10'-dibromo-9,9'-bianthryl (DBBA) on Au(111) and Au(110). We follow each step of the synthesis process in detail by using a combination of x-ray photoemission (XPS), near-edge x-ray absorption fine structure (NEXAFS) and angle resolved ultraviolet photoemission spectroscopies (ARUPS). Through XPS core-level shifts, we show that Br-C bond cleavage begins at temperatures as low as 100 C, and the resulting radicals bind to Au, forming Au-C and Au-Br bonds. We show that Br desorbs at about 240 C, lower than had previously been predicted[120] Importantly, we find that polymerization of precursors proceeds after removal of halogens from Au, showing that the presence of halogens is the limiting factor in this step. Upon further annealing to 400 C the polymerized layer continuously transforms into a layer of flat lying GNRs. Finally, we use ARUPS and ab-initio calculations to study the electronics of the GNR/Au interface and show that the GNR/Au interaction, though weak, results in a sizable upshift of the Shockley surface state of Au(111), and in a reduction of its band dispersion.

4.1.4 Experimental Methods

We characterize the debromination process using XPS measurements of mono-layer films of DBBA deposited on either Au(111) or Au(110) substrates. These measurements are

carried out at the ALOISA/HASPES beamline (Elettra Synchrotron, Trieste)[65]. The Au substrates are first cleaned by repeated cycles of Ar sputtering and annealing to 800K. XPS measurements of the Au are made to ensure no contamination on the sample. The base pressure for the measurement chamber is maintained at 10-11 mbar and the sample preparation chamber at 10-10 mbar. DBBA from AOKBIO (98+% purity) is deposited on this substrate from a quartz Knudsen-type cell in line-of-sight with the sample preparation chamber. To form a sub-monolayer film, the Au substrate is maintained at room temperature, and the Knudsen cell is heated to 490K. The molecule is deposited at a chamber pressure of 10-8 mbar with a typical rates of $\sim 2 \text{ \AA/min}$ for $\sim 2\text{-}5 \text{ min}$. DBBA coverages which resulted in full monolayer film formation have been monitored by HAS specular reflectivity, by UPS and by XPS (C1s and Br 3d) peak positions. (See SI for details)

4.1.5 Results

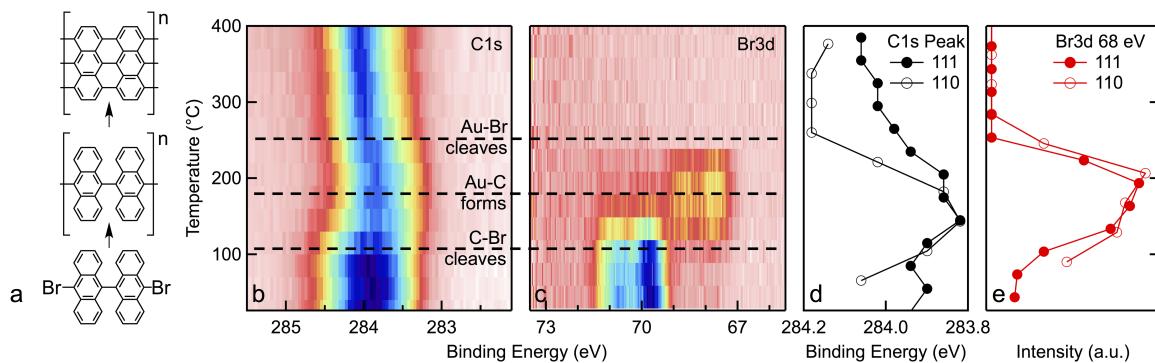


Figure 4.1 – Nanoribbon Formation Scheme and XPS Results

a Schematic of graphene nanoribbon (GNR) formation. Debromination and polymerization of the precursor DBBA molecules are followed by a cyclodehydrogenation step to create flat GNR.

b and **c** Temperature dependent XPS for C1s and Br3d for DBBA/Au(111) respectively. The three dashed lines correspond to three intermediate steps.

d and **e** Comparison of C1s peak position and Br3d 67-69 eV peak intensity against temperature for the Au(111) and Au(110) surfaces showing that Br desorbs as the C1s peak shifts to higher binding energy.

To probe the GNR formation process, we perform temperature-dependent XPS on C1s and Br3d core levels (Figure 4.1b and c) on a monolayer film of DBBA/Au(111) (data for the Au(110) surface is shown in SI Figure 4.7). This is done by slowly ramping the sample temperature at a rate of 10 K/min while conducting XPS scans. Comparisons of XPS on illuminated versus non-illuminated sample regions show that no change in the monolayer films occurs due to beam exposure. At temperatures below 100 C, the C1s core level is a broad peak centered at an electron binding energy of 284 eV, indicative of multiple carbon species, while the major Br3d peak is a spin-orbit split doublet at 70/71 eV. As temperature is increased above 100 C, an additional Br3d doublet appears at 68/69 eV indicating that there are two types of Br atoms with distinct chemical environments, while the C1s peak shifts gradually to lower binding energies. As substrate temperature is increased to 180 C, the Br3d doublet at 70/71 eV converts entirely to the 68/69 eV doublet while the C1s peak narrows and shifts to lower binding energy. The slight downshift (~0.3 eV) of the C1s XPS peak indicates the chemisorption of the dehalogenated bianthryl radicals on the underlying Au(111) substrate stabilized by the C-Au interaction, consistent with the theoretically predicted shift for the majority of the C atoms on the molecule[120]. The 2 eV shift in the Br 3d doublet agrees well with the core-level shift predicted due to Br-Au bond formation[120]. At 200 C, DBBA is entirely transformed into the chemisorbed bianthryl and Br radicals stabilized by the Au substrate. On further heating to temperatures above 250 C, all signatures of Br are lost, indicating a complete desorption of the halogen. The complete removal of halogens is crucial, since their presence can impact the dynamics of the self-assembly process, the defect density of the resulting GNRs and can electronically dope the GNR[158]. The temperature for complete desorption of Br on both Au(111) and Au(110) found here is significantly lower than calculated[120] or measured previously for similar systems[159, 160]. Furthermore, we see that as the Br desorbs, the C1s core level

energy shifts to higher binding energy (~ 0.4 eV) consistent with the shift expected for C-Au cleavage followed by polymerization (C-C formation)[120]. In Figure 4.1 d and e, we follow the position of the C1s peak and the integrated intensity of the Br3d 68/69 eV doublet. We see that the shift of the C1s peak correlates exactly with the intensity of the Br3d doublet on both Au(111) and Au(110) confirming that Br desorption precedes the bianthryl polymerization. This suggests that there is a weak Br-C interaction after bond scission that slows monomer diffusion and prevents polymerization. Similar interactions have been observed by STM for Iodine terminated cyclohexa-m-phenylene on Cu(111)[161].

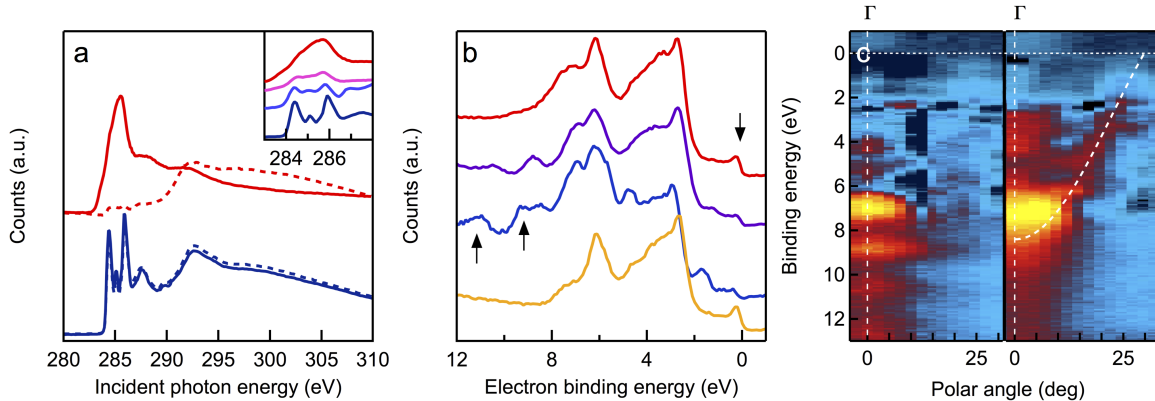


Figure 4.2 – NEXAFS and UPS Spectroscopy

a NEXAFS spectra with s-pol (dashed lines) or p-pol (solid lines) for films at 0 C (blue) and 400 C (red). **Inset:** π -resonance at 0 C, 120 C, 270 C, 400 C (blue to red). **b** UPS measurements of DBBA/Au(111). Clean Au (yellow) shows a prominent surface state at ~ 0.5 eV. DBBA deposition at 0C (blue) shows disappearance of surface state and appearance of molecular orbitals (up arrows). Molecular peaks diminish at 200 C (purple). Upon heating to 400 C (red), the surface state recovers entirely (down arrow). **c** ARUPS for DBBA/Au(111) at 200 C and 400 C. At 400 C a graphene-like band forms with a band minimum at -8.5 eV.

The XPS data clearly show Br desorption while C remains on the surface even at 400C. To better understand the morphology and electronic structure of the intermediate and final system formed, we turn to NEXAFS measurements and study their evolution as a function of temperature. NEXAFS spectra are collected with incident photon energy between 280 eV and 310 eV, an incidence angle of 6° and with the electric field polarization either

parallel (s-pol) or perpendicular (p-pol) to the sample. We start with measurements on a multilayer sample to ensure that the data is from an intact molecule. At 0 C, the C K-edge NEXAFS for DBBA/Au(111) is dominated by a C1s to π^* triple peak structure between 284-286 eV (Figure 4.2a, blue curves), reminiscent of the π system of anthracene[162]. The spectra are identical in s-pol (dark blue) and p-pol (light blue), which is expected in disordered multilayers[32]. Above room temperature, molecules desorb leaving a monolayer sample, as determined from the XPS C1s peak location and C1s to Au4f signal ratios[32]. Upon annealing to higher temperatures the π^* triple-peak structure broadens extending to lower energies (Figure 4.2a, inset), consistent with the formation of extended graphene-like systems[163]. Additionally, the final structure obtained after annealing to temperatures above 400 C is extremely dichroic (Figure 4.2a, red curves) with maximum C1s to π^* intensity observed in p-pol. This indicates that the resulting GNRs lie flat on the Au surface. Annealing also results in the recovery of the specular peak in HAS (See SI), showing that the GNRs are well ordered on the surface.

We now examine the evolution of the highest occupied (valence) states of the system for each annealing step. Ultraviolet Photoemission Spectroscopy (UPS) measurements of DBBA/Au(111) taken with 21.22 eV light in normal emission show photoemission peaks from ‘molecular’ occupied states (e.g. 11 eV and 9 eV) at substrate temperatures <100 C (Figure 4.2b, blue curve). Deposition at a higher temperature (200 C, purple) and subsequent anneal to 400 C (red curve) results in these features disappearing, indicating the formation of GNRs. We also follow the evolution of the Shockley surface state of Au(111)[164], at about 0.5 eV from the Fermi energy, E_F . The surface state is clearly visible for clean Au(111) (yellow curve, Figure 4.2b), but disappears when molecules are added. Annealing to 400 C (red curve) results in the reappearance of the state indicating that the interaction between the GNR and the Au surface is weak as found for other

π -conjugated molecules[164].

To better understand the electronic structure of the GNR and its interaction with Au, we measure the angular dependence of the valence band structure through angle resolved UPS using a He II UV source ($h\nu=40.8$ eV)[165, 166, 167, 168]. Figure 4.2c shows that at 200 C, DBBA/Au(111) has molecular-like occupied states that show no dispersion. Upon heating to 400 C, the final GNR film shows a graphene-like dispersion, with the bottom of the occupied band at 8.5 eV binding energy analogous to that of pristine graphene[169, 170], indicating that the GNR film is not doped by charge transfer from the substrate or Br. The relatively broad linewidth of the dispersion is likely due to the fact that Au(111), unlike the related vicinal surfaces, does not induce oriented growth of GNRs[168].

We further study the strength of the interaction between the GNR and Au by examining the Shockley surface state of Au(111) using ARUPS with incident light from the He I emission at 21.22 eV. Figure 4.3a shows the surface state of Au(111), with a band bottom at 0.44 eV and an effective mass $m^*=0.24 m_e$, consistent with previous experimental measurements at room temperature[171, 172]. The position of the band bottom is known to be sensitive to interactions with adsorbed molecules[164], and the state can disappear completely due to strongly chemisorbed systems or surface reconstruction. On depositing DBBA on pristine Au(111) at room temperature (Figure 4.3b), we no longer see the surface state, likely due to an interaction between the Br on the molecule and the underlying substrate. The substrate is then heated gradually beyond 240 C, when we see that the surface state reemerges. This indicates that the absence of the surface state in Figure 4.3b is the result of significant Br-Au and C-Au interaction. Annealing to 400 C results in a GNR film with a surface state that is shifted towards E_F by nearly 0.14 eV and made less dispersive with an effective mass $m^*=0.34 m_e$ (see Figure 4.3d).

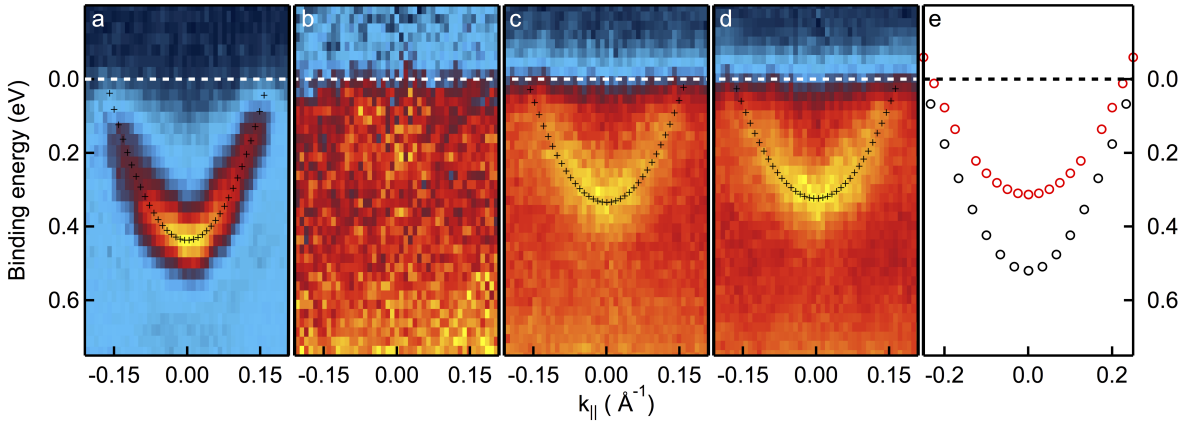


Figure 4.3 – Evolution of the Shockley Surface State via ARPES

Angle resolved photoemission intensity of the surface state of Au(111) for **a** clean Au(111) **b** a monolayer of DBBA precursor. The missing surface state points to strong interaction with the surface. **c** The surface state recovers at 270 C and **d** becomes stronger at 400 C. A best fit is shown in black markers. The surface state of the film in **d** is broadened shifted upwards by 0.14 eV compared with that of the Au(111) surface, **e** Calculated surface state for pristine Au(111) (black circles), and GNR film on Au(111) (red circles).

We perform Density Functional Theory (DFT) based calculations to understand this evolution of the surface state. Simulations were performed within the local density approximation (LDA) for the exchange-correlation potential, using a plane-wave basis set and ultrasoft pseudopotentials, as implemented in the Quantum-ESPRESSO package[173]. We considered both the pristine Au(111) and GNR/Au(111) surfaces. A 3x4 $\sqrt{3}$ surface cell of Au(111) was employed to accommodate two unit cells of the GNR in order to have a commensurate system (Figure S6, SI). The in-plane lattice parameter was set to the optimized parameter for bulk Au (4.05 Å), and the atomic positions within the cell were fully optimized, with a force threshold of 0.013 eV/Å. The GNR presents a residual 1.05% stretching along its main axis when compared to the free-standing optimized geometry. Brillouin zone sampling was done by using a 4x8x1 k-points grid and the kinetic energy cutoff for the wave functions (charge density) was set to 25 (300) Ry. The surfaces were modeled using a five-layers slab of Au(111) passivated with H atoms on one side. We have

checked that the surface-state position is fully converged with respect to the slab thickness (Figure S7, SI).

The calculated surface states for both clean Au(111) and GNR/Au(111) surfaces are reported in Figure 4.3e. In agreement with experimental findings, our calculations show an upward shift of the surface state band bottom by 0.2 eV and a decreased band dispersion ($m^*(\text{Au}) = 0.25 \text{ m}_e$; $m^*(\text{GNR}/\text{Au}) = 0.34 \text{ m}_e$) upon GNR adsorption. Calculations of graphene adsorbed on Au(111), a similar system, show an upward shift of the surface state onset at Γ of about 87 meV. As suggested by Ziroff and coworkers[164], such shifts correlate with the molecule-surface adsorption energy. We find an adsorption energy of 54 meV/carbon for the GNR/Au(111) system, larger than that calculated for graphene/Au (33 meV/carbon)[174, 175], which is also consistent with the trend for the calculated molecule-surface distance (3.35 Å for graphene against 3.13 Å for the GNR).

In summary, the results presented here show that GNR formation and dehalogenation on Au can occur at significantly lower temperatures than previously reported, opening new avenues for growth of such systems. Our work shows that the polymerization of precursor molecules is activated by desorption of halogens from the metal surface, a key insight in optimizing conditions for uniform growth of GNRs. Finally, comparing theory and experiments on the surface state of Au(111), we show that while the GNR/Au(111) is weakly coupled, the interaction is sizable and stronger than that of graphene/Au(111).

4.1.6 Supplementary Information

Details of Theoretical Calculations

We perform Density Functional Theory (DFT) based theoretical calculations to understand the electronic structure of the gold surface state with and without a graphene nano ribbons over layer. Simulations were performed within the local density approximation

(LDA) for the exchange-correlation potential, using a plane-wave basis set and ultrasoft pseudopotentials, as implemented in the Quantum-ESPRESSO package[173]. The kinetic energy cutoff for the wave functions (charge density) was set to 25 (300) Ry. We considered both the pristine Au(111) surface and Au(111) with the adsorbed GNR. The surfaces were modeled using a five-layer slab of Au(111); a $3\times4\sqrt{3}$ supercell was employed to accommodate the GNR. Slabs were passivated with H on one side to inhibit interaction between Au(111) surface states resulting from the finite thickness of the slab. Moreover, slab replicas were separated by a vacuum region of 12 Å in order avoid spurious interactions. The in-plane lattice parameter was set to the optimized parameter for bulk Au (4.05 Å), and the atomic positions within the cell were fully optimized, with a force threshold of 0.026 eV/Å. When studying a pristine Au(111) slab, the finite width of the slab model leads to a artificial interaction of the states located on the two surfaces, resulting in two non-degenerate surface states. Eventually, the energies of these states converge to the same value when the number of layers is increased. The interaction between these states can be prevented by passivating one of the surfaces with H atoms, thereby removing one of the two surface states. This allows one to model the Au slab with a smaller number of atomic layers. The convergence with respect to the number of layers was verified both for H passivated and non-passivated slabs, as shown in Figure 4.10. When considering the hydrogenated Au(111) slab, the onset of the surface states at Γ is found to be converged with 5 layers.

Sample Preparation

The Au substrates are first cleaned by repeated cycles of Ar sputtering and annealing to 800K. Helium atom scattering (HAS) is then used to confirm the characteristic herringbone reconstruction of Au(111) or the 1x2 missing-row reconstruction of the Au(110) substrate. XPS measurements of the Au are made to ensure no contamination on the sample. The operational pressure for the measurement chamber is maintained at 10^{-11} mbar and the

sample preparation chamber at 10^{-10} mbar. DBBA from AOKBIO (98+% purity) is deposited on this substrate from a quartz Knudsen-type cell in line-of-sight with the sample preparation chamber. For monolayer deposition, the Au substrate is maintained at room temperature, and the Knudsen cell is heated to 490K. The molecule is deposited at a chamber pressure of 10^{-8} mbar with a typical rates of 2 Å/min. DBBA deposition and coverage is controlled by Helium (He) reflectivity and XPS. As molecules cover the Au crystalline surface the He specular intensity attenuates strongly (Figure 4.5), and eventually disappears in the diffuse background as the Au surface is covered. Due to larger-than-geometrical cross section for diffuse He scattering, the HAS signal disappears well before the full molecular monolayer fully covers the substrate. Formation of any further layers of molecules beyond monolayer may be also witnessed by the shift of XPS peaks to higher binding energies, due to reduced screening of the core hole by the metal substrate. Helium Atom Scattering (HAS) measurements were carried out at the HASPES beamline at the Elettra Synchrotron, Trieste, Italy. Details can be found in previously published work[176]

Additional Data

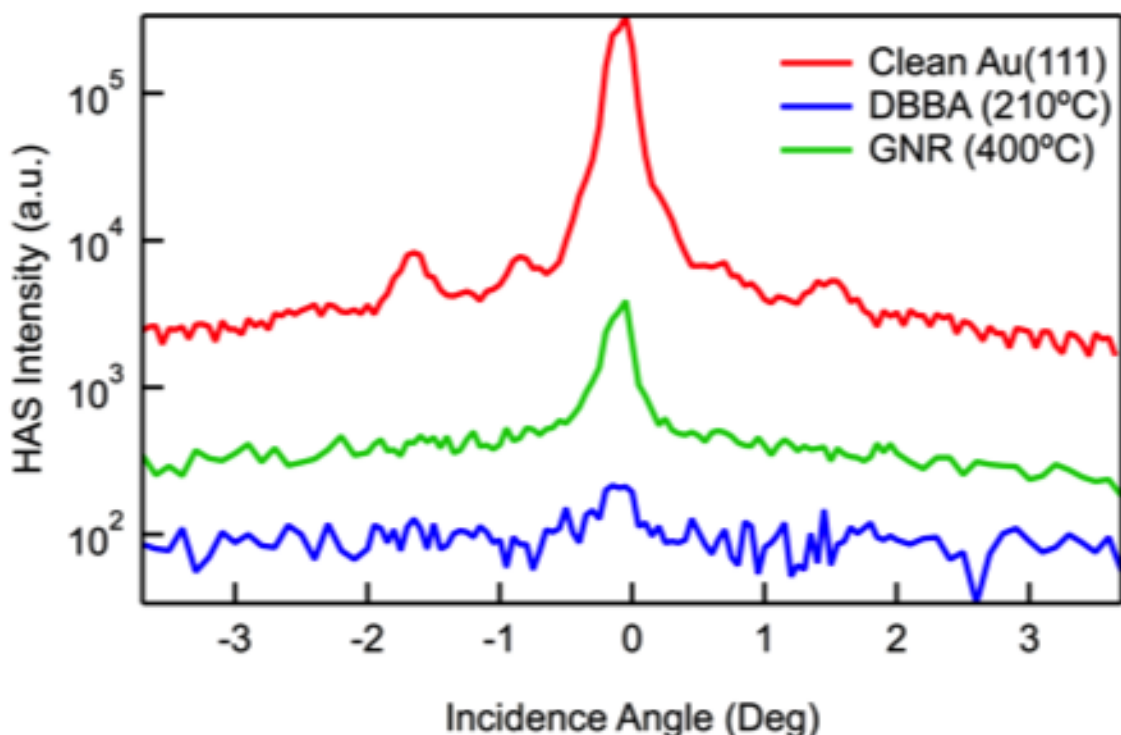


Figure 4.4 – Helium Atom Scattering with Temperature Ramp

HAS Intensity as a function of incident beam angle. Clean Au(111) (red) shows a strong peak at the specular angle (0). DBBA is deposited with the sample temperature at 210 C, resulting in the diminishment of the specular peak (blue) due to a disordered layer. Heating this film to 400C (green) shows that the signal recovers, signifying an increasingly ordered surface commensurate with polymerization and GNR formation.

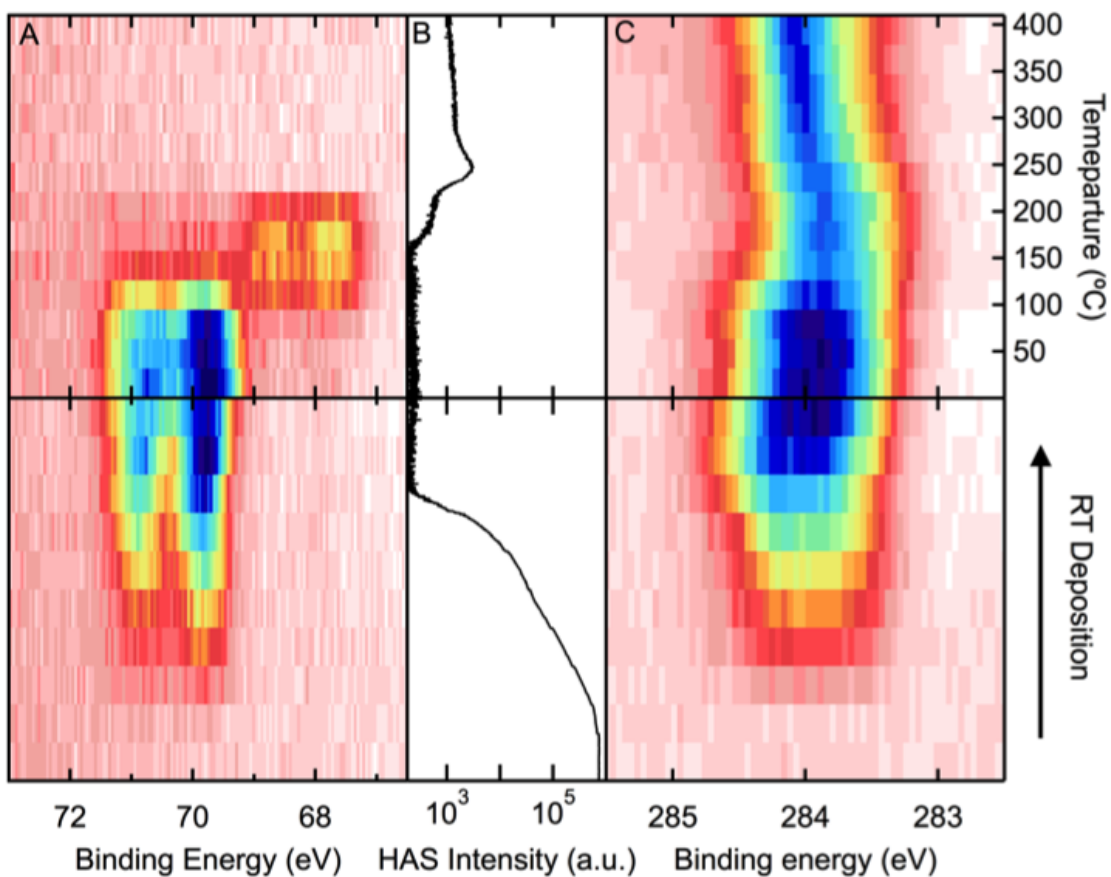


Figure 4.5 – Comparing HAS and XPS signals

Simultaneous measurement of HAS Specular Reflectivity and XPS signal as a function of DBBA deposition time and annealing temperature on Au(111). **A** Br XPS signal. **B** HAS Specular intensity single. **C** C1s XPS signal. The HAS intensity is lowest after molecule deposition at RT and increases as the substrate is annealed.

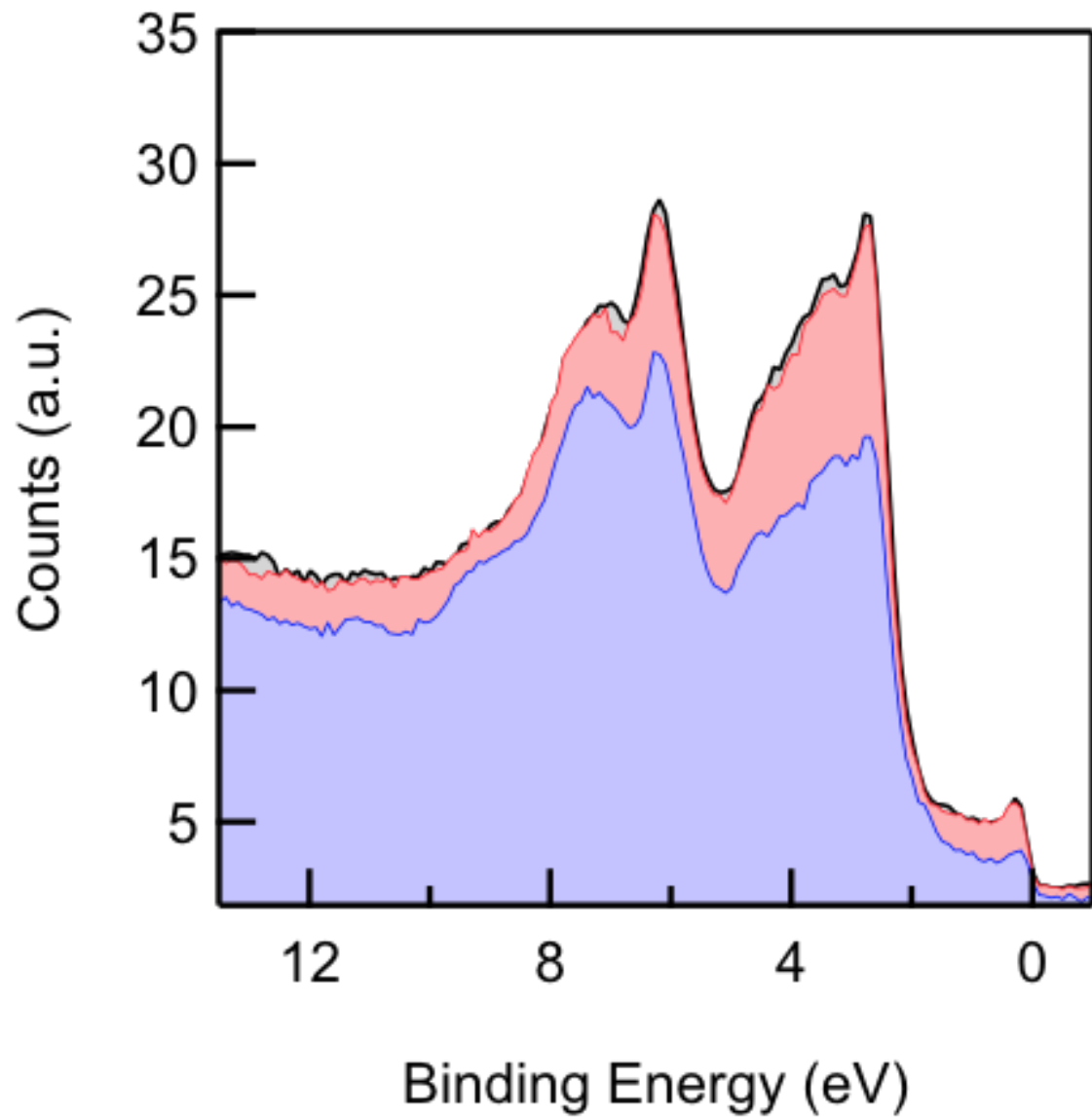


Figure 4.6 – UPS measurements show GNR film saturation

UPS spectrum for GNR (black, solid). Additional deposition at 100C (blue) results in a diminished gold signal, and molecular resonances appearing. On heating to 400C (red), the film recovers original UPS spectrum, showing that the original GNR film was saturated and inert.

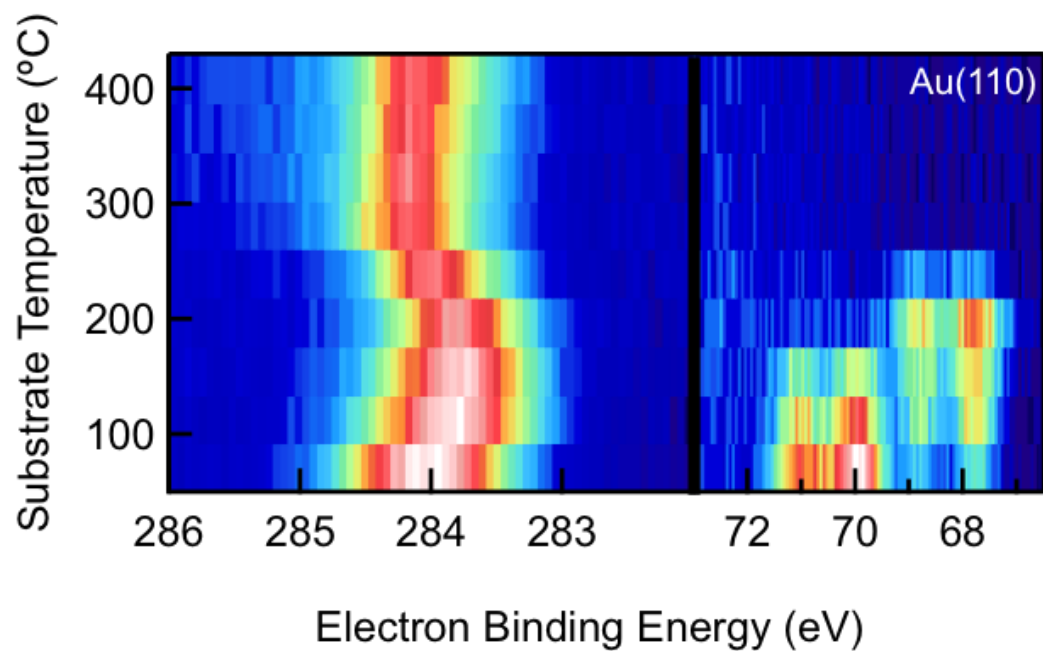


Figure 4.7 – Temperature dependent XPS on Au(110)

Temperature dependent XPS for C1s (left panel) and Br3d (right panel) for DBBA/Au(110). The overall evolution of the XPS signal is similar to that of DBBA/Au(111) presented in earlier sections.

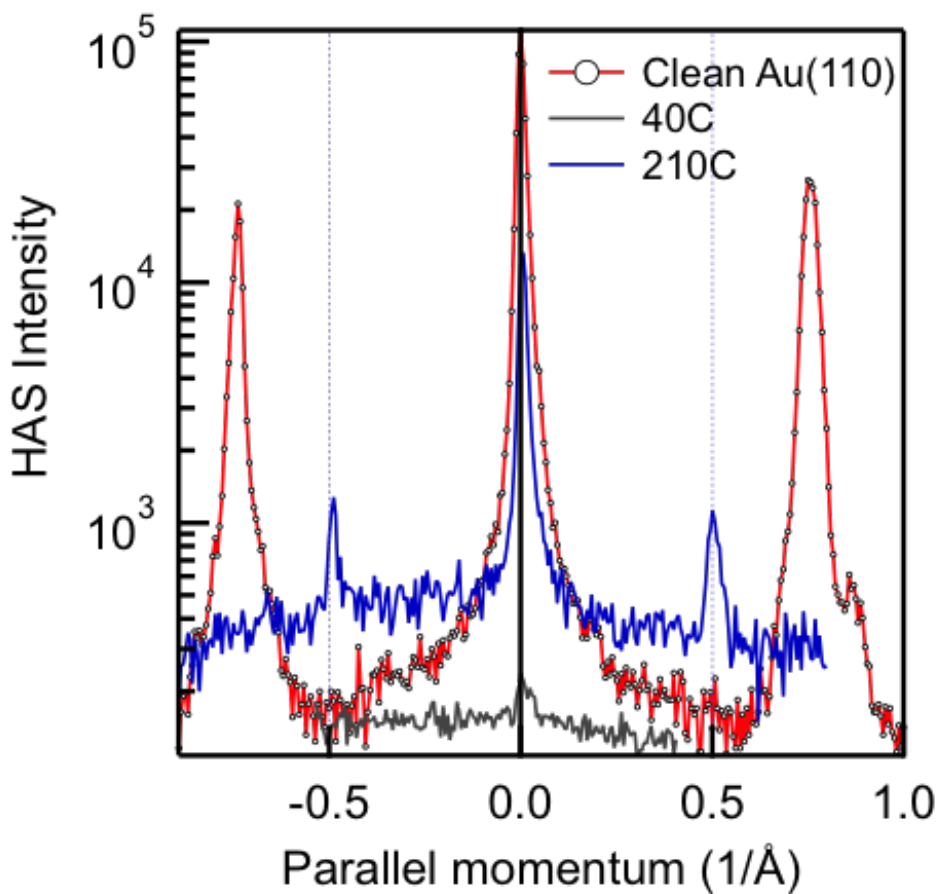


Figure 4.8 – HAS on DBBA/Au(110)

Helium Atom Scattering (HAS) on DBBA/Au(110). HAS Intensity as a function of incident beam angle for different film conditions. Clean Au(110) (red) shows the characteristic spectrum for a 1×2 reconstruction. A monolayer of DBBA is deposited at RT, resulting in the diminishment of the specular peak (black) due to disordered adsorption of the molecule. Heating this film to 210C (blue) and 400C (green) shows that the signal recovers but with a 1×3 reconstruction, suggesting that molecule-metal interaction changes the surface reconstruction.

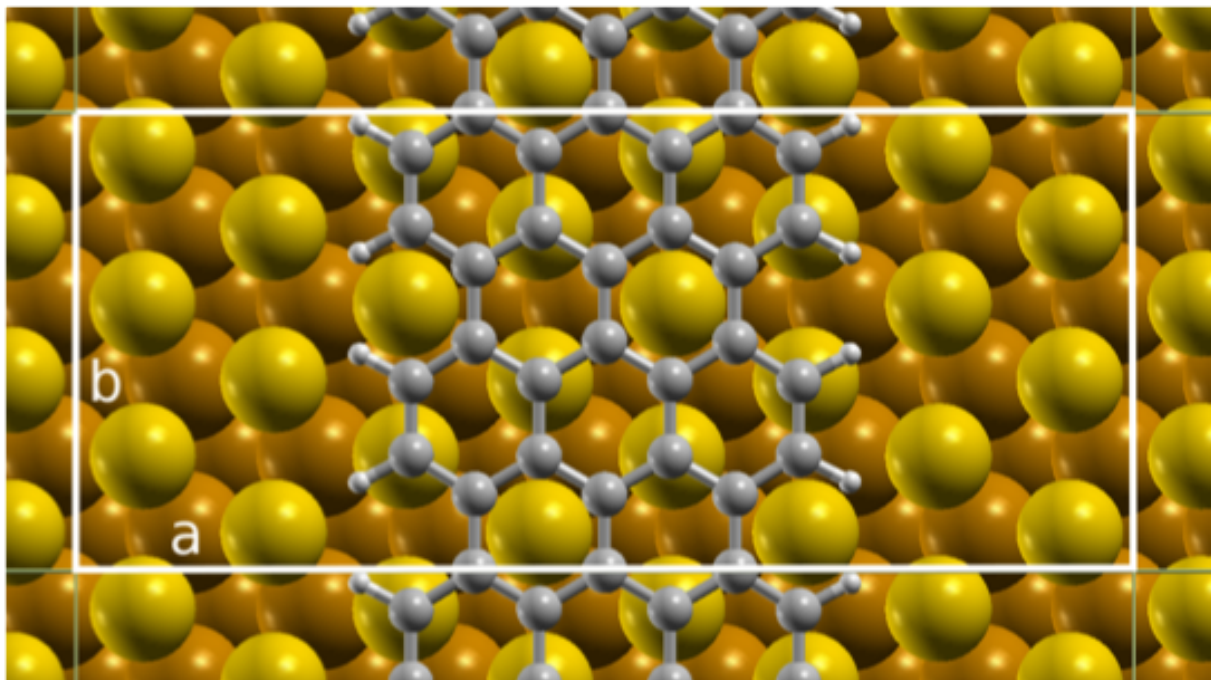


Figure 4.9 – Unit cell of the GNR + Au(111) surface system used in the calculations. The cell parameters of the unit cell in surface plane are $a = 19.84 \text{ \AA}$ and $b = 8.59 \text{ \AA}$. The surfaces were modeled using a five-layer slab of Au(111). Slabs were passivated with H on one side. Slab replicas were separated by a vacuum region of 12 \AA .

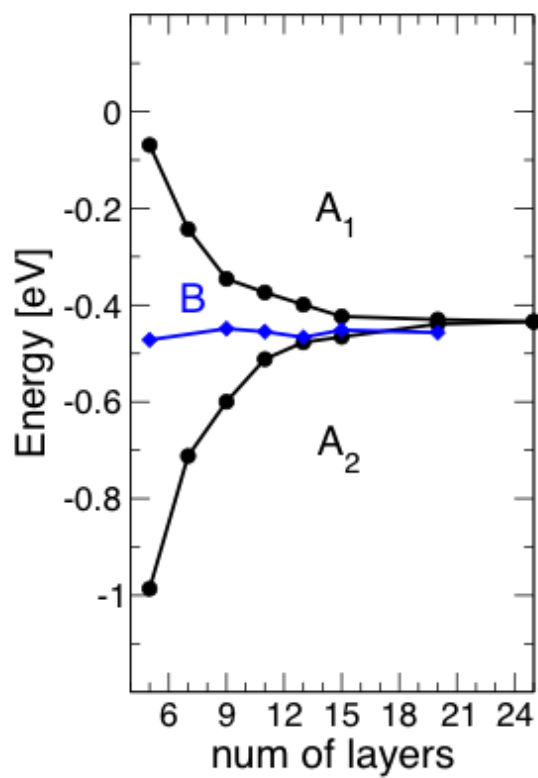


Figure 4.10 – Surface Band energy level convergence

Energy of the bottom of the surface band computed for slabs with different number of Au layers, both for non-hydrogenated (A1 and A2) and hydrogenated (B) slabs. All calculations were performed at the LDA level.

Bibliography

- [1] Hyungsub Choi and Cyrus CM Mody. The Long History of Molecular Electronics Microelectronics Origins of Nanotechnology. *Social Studies of Science*, 39(1):11–50, 2009. (page [1](#)).
- [2] A. Aviram and M. A. Ratner. Molecular Rectifiers. *Chemical Physics Letters*, 29(2):277–283, 1974. (pages [1](#), [77](#)).
- [3] Richard L McCreery, Haijun Yan, and Adam Johan Bergren. A critical perspective on molecular electronic junctions: there is plenty of room in the middle. *Physical Chemistry Chemical Physics*, 15(4):1065–1081, 2013. (page [2](#)).
- [4] Rolf Landauer. Electrical resistance of disordered one-dimensional lattices. *Philosophical Magazine*, 21(172):863–867, 1970. (page [2](#)).
- [5] M Büttiker, Y Imry, R Landauer, and S Pinhas. Generalized many-channel conductance formula with application to small rings. *Physical Review B*, 31(10):6207, 1985. (page [2](#)).
- [6] Supriyo Datta. *Electronic transport in mesoscopic systems*. Cambridge university press, 1997. (pages [3](#), [98](#)).
- [7] Ferdows Zahid, Magnus Paulsson, and Supriyo Datta. Electrical conduction through molecules. *Advanced Semiconductors and Organic Nano-Techniques*, 2003. (page [3](#)).

- [8] Magnus Paulsson, Ferdows Zahid, and Supriyo Datta. Resistance of a molecule. *arXiv preprint cond-mat/0208183*, 2002. (page 3).
- [9] JJ Palacios, AJ Pérez-Jiménez, E Louis, E SanFabián, and JA Vergés. First-principles approach to electrical transport in atomic-scale nanostructures. *Physical Review B*, 66(3):035322, 2002. (page 3).
- [10] Magnus Paulsson. Non equilibrium green's functions for dummies: Introduction to the one particle NEGF equations. *arXiv preprint cond-mat/0210519*, 2002. (pages 3, 4).
- [11] Y. S. Park, A. C. Whalley, M. Kamenetska, et al. Contact chemistry and single-molecule conductance: A comparison of phosphines, methyl sulfides, and amines. *Journal of the American Chemical Society*, 129(51):15768–15769, 2007. (pages 6, 48, 78).
- [12] Gemma C Solomon, David Q Andrews, Thorsten Hansen, et al. Understanding quantum interference in coherent molecular conduction. *The Journal of Chemical Physics*, 129(5):054701, 2008. (page 8).
- [13] David M Cardamone, Charles A Stafford, and Sumit Mazumdar. Controlling quantum transport through a single molecule. *Nano Letters*, 6(11):2422–2426, 2006. (page 8).
- [14] Charles A Stafford, David M Cardamone, and Sumit Mazumdar. The quantum interference effect transistor. *Nanotechnology*, 18(42):424014, 2007. (page 8).
- [15] Troels Markussen, Robert Stadler, and Kristian S Thygesen. The relation between structure and quantum interference in single molecule junctions. *Nano Letters*, 10(10):4260–4265, 2010. (page 8).

- [16] Kazunari Yoshizawa, Tomofumi Tada, and Aleksandar Staykov. Orbital views of the electron transport in molecular devices. *Journal of the American Chemical Society*, 130(29):9406–9413, 2008. (pages 8, 10).
- [17] C. M. Guédon, H. Valkenier, T. Markussen, et al. Observation of quantum interference in molecular charge transport. *Nature Nanotechnology*, 7(5):305–9, 2012. (pages 8, 48, 78).
- [18] Jianlong Xia, Brian Capozzi, Sujun Wei, et al. Breakdown of Interference Rules in Azulene, a Non-Alternant Hydrocarbon. *Nano Letters*, 2014. (page 10).
- [19] Sriharsha V. Aradhya, Jeffrey S. Meisner, Markrete Krikorian, et al. Dissecting Contact Mechanics from Quantum Interference in Single-Molecule Junctions of Stilbene Derivatives. *Nano Letters*, 12(3):1643–1647, 2012. (pages 10, 47, 48, 49, 50).
- [20] Jeffrey S. Meisner, Seokhoon Ahn, Sriharsha V. Aradhya, et al. Importance of Direct Metal-pi Coupling in Electronic Transport Through Conjugated Single-Molecule Junctions. *Journal of the American Chemical Society*, 134(50):20440–20445, 2012. (pages 10, 54).
- [21] M. A. Reed, C. Zhou, C. J. Muller, T. P. Burgin, and J. M. Tour. Conductance of a molecular junction. *Science*, 278(5336):252–254, 1997. (pages 11, 47, 77).
- [22] Wenjie Liang, Matthew P Shores, Marc Bockrath, Jeffrey R Long, and Hongkun Park. Kondo resonance in a single-molecule transistor. *Nature*, 417(6890):725–729, 2002. (page 11).
- [23] Jiwoong Park, Abhay N Pasupathy, Jonas I Goldsmith, et al. Coulomb blockade

- and the Kondo effect in single-atom transistors. *Nature*, 417(6890):722–725, 2002. (page 11).
- [24] Xuefeng Guo, Joshua P Small, Jennifer E Klare, et al. Covalently bridging gaps in single-walled carbon nanotubes with conducting molecules. *Science*, 311(5759):356–359, 2006. (page 11).
- [25] Sergey Kubatkin, Andrey Danilov, Mattias Hjort, et al. Single electron transistor with a single conjugated molecule. *Current Applied Physics*, 4(5):554–558, 2004. (page 11).
- [26] B. Q. Xu and N. J. Tao. Measurement of single-molecule resistance by repeated formation of molecular junctions. *Science*, 301(5637):1221–1223, 2003. (pages 11, 48, 78).
- [27] MP Seah. The quantitative analysis of surfaces by XPS: a review. *Surface and Interface Analysis*, 2(6):222–239, 1980. (page 14).
- [28] MP Seah. A review of the analysis of surfaces and thin films by AES and XPS. *Vacuum*, 34(3):463–478, 1984. (pages 14, 15).
- [29] PA Brühwiler, AJ Maxwell, C Puglia, et al. π^* and σ^* Excitons in C 1 s Absorption of Graphite. *Physical Review Letters*, 74(4):614, 1995. (page 16).
- [30] Georg Hähner. Near edge X-ray absorption fine structure spectroscopy as a tool to probe electronic and structural properties of thin organic films and liquids. *Chemical Society Reviews*, 35(12):1244–1255, 2006. (pages 16, 17, 18).
- [31] David J Griffiths. *Introduction to quantum mechanics: pearson new international edition*. Pearson Education Limited, 2013. (page 17).

- [32] J. Stohr. *NEXAFS Spectroscopy*. Heidelberg, 1992. (pages 18, 19, 65, 108).
- [33] PA Brühwiler, AJ Maxwell, A Nilsson, RL Whetten, and N Mårtensson. Resonant photoemission of solid C₆₀. *Chemical Physics Letters*, 193(5):311–316, 1992. (page 20).
- [34] AJ Maxwell, PA Brühwiler, A Nilsson, N Mårtensson, and P Rudolf. Photoemission, autoionization, and x-ray-absorption spectroscopy of ultrathin-film C₆₀ on Au (110). *Physical Review B*, 49(15):10717, 1994. (page 20).
- [35] P. A. Brühwiler, O. Karis, and N. Mårtensson. Charge-transfer dynamics studied using resonant core spectroscopies. *Reviews of Modern Physics*, 74(3):703–740, 2002. (pages 20, 22, 25, 33).
- [36] A. Batra, G. Kladnik, H. Vazquez, et al. Quantifying through-space charge transfer dynamics in pi-coupled molecular systems. *Nature Communications*, 3:1086, 2012. (pages 21, 23, 52).
- [37] Roald Hoffmann. Interaction of orbitals through space and through bonds. *Accounts of Chemical Research*, 4(1):1–9, 1971. (pages 24, 27).
- [38] Gregory D. Scholes and Garry Rumbles. Excitons in nanoscale systems. *Nature Materials*, 5(9):683–696, 2006. (page 24).
- [39] T. Nakano. Synthesis, structure and function of pi-stacked polymers. *Polymer Journal*, 42(2):103–123, 2010. (page 24).
- [40] Jason D Slinker, Natalie B Muren, Sara E Renfrew, and Jacqueline K Barton. DNA charge transport over 34 nm. *Nature Chemistry*, 3(3):228–233, 2011. (page 24).

- [41] Hirao Toshikazu. Conjugated systems composed of transition metals and redox active pi-conjugated ligands. *Coordination Chemistry Reviews*, 226(1–2):81–91, 2002. (page 24).
- [42] Taisuke Ohta, Aaron Bostwick, J. McChesney, et al. Interlayer Interaction and Electronic Screening in Multilayer Graphene Investigated with Angle-Resolved Photoemission Spectroscopy. *Physical Review Letters*, 98(20), 2007. (page 24).
- [43] S. T. Schneebeli, M. Kamenetska, Z. Cheng, et al. Single-molecule conductance through multiple pi-pi-stacked benzene rings determined with direct electrode-to-benzene ring connections. *Journal of the American Chemical Society*, 133(7):2136–9, 2011. (pages 24, 44).
- [44] Joseph Zyss, Isabelle Ledoux, Sergei Volkov, et al. Through-Space Charge Transfer and Nonlinear Optical Properties of Substituted Paracyclophe. *Journal of the American Chemical Society*, 122(48):11956–11962, 2000. (page 24).
- [45] H. Sirringhaus, P. J. Brown, R. H. Friend, et al. Two-dimensional charge transport in self-organized, high-mobility conjugated polymers. *Nature*, 401(6754):685–688, 1999. (page 24).
- [46] Serap Günes, Helmut Neugebauer, and Niyazi Serdar Sariciftci. Conjugated Polymer-Based Organic Solar Cells. *Chemical Reviews*, 107(4):1324–1338, 2007. (page 24).
- [47] Do Hwan Kim, Yunseok Jang, Yeong Don Park, and Kilwon Cho. Surface-Induced Conformational Changes in Poly(3-hexylthiophene) Monolayer Films. *Langmuir*, 21(8):3203–3206, 2005. (page 25).
- [48] Peter Peumans, Soichi Uchida, and Stephen R. Forrest. Efficient bulk heterojunction

- photovoltaic cells using small-molecular-weight organic thin films. *Nature*, 425(6954):158–162, 2003. (page 25).
- [49] Alex C. Mayer, Matthew T. Lloyd, David J. Herman, Todd G. Kasen, and George G. Malliaras. Postfabrication annealing of pentacene-based photovoltaic cells. *Applied Physics Letters*, 85(25):6272–6274, 2004. (page 25).
- [50] Yeong Don Park, Jung Ah Lim, Hwa Sung Lee, and Kilwon Cho. Interface engineering in organic transistors. *Materials Today*, 10(3):46–54, 2007. (page 25).
- [51] Lorette Scifo, Mathieu Dubois, Mickael Brun, et al. Probing the Electronic Properties of Self-Organized Poly(3-dodecylthiophene) Monolayers by Two-Dimensional Scanning Tunneling Spectroscopy Imaging at the Single Chain Scale. *Nano Letters*, 6(8):1711–1718, 2006. (page 25).
- [52] Dietrich Menzel. Ultrafast charge transfer at surfaces accessed by core electron spectroscopies. *Chemical Society Reviews*, 37(10):2212–2223, 2008. (page 25).
- [53] A. Fohlisch, P. Feulner, F. Hennies, et al. Direct observation of electron dynamics in the attosecond domain. *Nature*, 436(7049):373–376, 2005. (page 25).
- [54] Joachim Schnadt, Paul A. Bruhwiler, Luc Patthey, et al. Experimental evidence for sub-3-fs charge transfer from an aromatic adsorbate to a semiconductor. *Nature*, 418(6898):620–623, 2002. (page 25).
- [55] A. J. Britton, A. Rienzo, J. N. O’Shea, and K. Schulte. Charge transfer between the Au(111) surface and adsorbed C(60): Resonant photoemission and new core-hole decay channels. *Journal of Chemical Physics*, 133(9):094705, 2010. (page 25).
- [56] H. Hamoudi, S. Neppl, P. Kao, et al. Orbital-Dependent Charge Transfer Dynamics

- in Conjugated Self-Assembled Monolayers. *Physical Review Letters*, 107(2):027801, 2011. (page 25).
- [57] Wei Chen, Li Wang, Chun Huang, et al. Effect of Functional Group (Fluorine) of Aromatic Thiols on Electron Transfer at the Molecule-Metal Interface. *Journal of the American Chemical Society*, 128(3):935–939, 2005. (page 25).
- [58] M. Dell’Angela, G. Kladnik, A. Cossaro, et al. Relating energy level alignment and amine-linked single molecule junction conductance. *Nano Letters*, 10(7):2470–4, 2010. (page 25).
- [59] Paolo Vilmercati, Carla Castellarin-Cudia, Ralph Gebauer, et al. Mesoscopic Donor-Acceptor Multilayer by Ultrahigh-Vacuum Codeposition of Zn-Tetraphenyl-Porphyrin and C70. *Journal of the American Chemical Society*, 131(2):644–652, 2008. (page 25).
- [60] Steven M. Bachrach. DFT Study of [2.2]-, [3.3]-, and [4.4]Paracyclophanes: Strain Energy, Conformations, and Rotational Barriers. *The Journal of Physical Chemistry A*, 115(11):2396–2401, 2011. (page 27).
- [61] Christopher A. Hunter and Jeremy K. M. Sanders. The nature of .pi.-.pi. interactions. *Journal of the American Chemical Society*, 112(14):5525–5534, 1990. (page 27).
- [62] R. Friedlein, S. Braun, M. P. de Jong, et al. Ultra-fast charge transfer in organic electronic materials and at hybrid interfaces studied using the core-hole clock technique. *Journal of Electron Spectroscopy and Related Phenomena*, 183(1–3):101–106, 2011. (pages 28, 34).
- [63] W. Wurth and D. Menzel. Decay channels of resonant and continuum core excitations

- in condensed ethylene and cyclohexane. *Journal of Electron Spectroscopy and Related Phenomena*, 62(1–2):23–31, 1993. (pages 28, 34).
- [64] Lucas Viani, Yoann Olivier, Stavros Athanasopoulos, et al. Theoretical Characterization of Charge Transport in One-Dimensional Collinear Arrays of Organic Conjugated Molecules. *ChemPhysChem*, 11(5):1062–1068, 2010. (pages 28, 35, 47, 52).
- [65] L. Floreano, G. Naletto, D. Cvetko, et al. Performance of the grating-crystal monochromator of the ALOISA beamline at the Elettra Synchrotron. *Review of Scientific Instruments*, 70(10):3855–3864, 1999. (pages 30, 36, 61, 105).
- [66] D. Cvetko, A. Lausi, A. Morgante, et al. Compact He beam scattering apparatus for surface studies. *Measurement Science and Technology*, 3(10):997, 1992. (pages 30, 36).
- [67] A. J. Maxwell, P. A. Brühwiler, A. Nilsson, N. Mårtensson, and P. Rudolf. Photoemission, autoionization, and x-ray-absorption spectroscopy of ultrathin-film C₆₀ on Au(110). *Physical Review B*, 49(15):10717–10725, 1994. (page 33).
- [68] Paolo Vilmercati, Dean Cvetko, Albano Cossaro, and Alberto Morgante. Heterostructured organic interfaces probed by resonant photoemission. *Surface Science*, 603(10–12):1542–1556, 2009. (pages 36, 38, 43).
- [69] P. J. Cumpson and M. P. Seah. Elastic scattering corrections in AES and XPS .2. Estimating attenuation lengths and conditions required for their valid use in overlayer/substrate experiments. *Surface and Interface Analysis*, 25(6):430–446, 1997. (pages 42, 43, 75).

- [70] Yihan Shao, Laszlo Fusti Molnar, Younsung Jung, et al. Advances in methods and algorithms in a modern quantum chemistry program package. *Physical Chemistry Chemical Physics*, 8(27), 2006. (pages 44, 56, 74).
- [71] Anders Nilsson and Lars Gunnar Moody Pettersson. Chemical bonding on surfaces probed by X-ray emission spectroscopy and density functional theory. *Surface Science Reports*, 55(2–5):49–167, 2004. (pages 45, 75).
- [72] M. A. Reed and J. M. Tour. Computing with molecules. *Scientific American*, 282(6):86–93, 2000. (page 47).
- [73] J. C. Ellenbogen and J. Christopher Love. Architectures for molecular electronic computers: 1. Logic structures and an adder designed from molecular electronic diodes. *Proceedings of the IEEE*, 88(3):386–426, 2000. (pages 47, 77).
- [74] Arunabh Batra, Pierre Thomas Darancet, Qishui Chen, et al. Tuning Rectification in Single-Molecular Diodes. *Nano Letters*, 13(12):6233–7, 2013. (pages 47, 50, 51, 87).
- [75] M. Elbing, R. Ochs, M. Koentopp, et al. A single-molecule diode. *Proceedings of the National Academy of Sciences of the United States of America*, 102(25):8815–8820, 2005. (pages 47, 77, 78, 81).
- [76] I. Díez-Pérez, J. Hihath, Y. Lee, et al. Rectification and stability of a single molecular diode with controlled orientation. *Nature Chemistry*, 1(8):635–641, 2009. (pages 47, 77, 78, 81).
- [77] A. Aviram and M. A. Ratner. Molecular Rectifiers. *Chemical Physics Letters*, 29(2):277–283, 1974. (page 47).

- [78] K. Stokbro, J. Taylor, and M. Brandbyge. Do Aviram - Ratner Diodes Rectify? *Journal of the American Chemical Society*, 125(13):3674–3675, 2003. (page 47).
- [79] S. K. Yee, J. B. Sun, P. Darancet, et al. Inverse Rectification in Donor-Acceptor Molecular Heterojunctions. *ACS Nano*, 5(11):9256–9263, 2011. (pages 47, 77).
- [80] V. Mujica, M. A. Ratner, and A. Nitzan. Molecular rectification: Why is it so rare? *Chemical Physics*, 281(2-3):147–150, 2002. (pages 47, 77).
- [81] C. Joachim, J. K. Gimzewski, and A. Aviram. Electronics using hybrid-molecular and mono-molecular devices. *Nature*, 408(6812):541–548, 2000. (page 47).
- [82] R. M. Metzger. Electrical rectification by a molecule: The advent of unimolecular electronic devices. *Accounts of Chemical Research*, 32(11):950–957, 1999. (page 47).
- [83] R. M. Metzger. Unimolecular electrical rectifiers. *Chemical Reviews*, 103(9):3803–3834, 2003. (pages 47, 77).
- [84] M. L. Chabinyc, X. X. Chen, R. E. Holmlin, et al. Molecular rectification in a metal-insulator-metal junction based on self-assembled monolayers. *Journal of the American Chemical Society*, 124(39):11730–11736, 2002. (page 47).
- [85] J. G. Kushmerick, C. M. Whitaker, S. K. Pollack, T. L. Schull, and R. Shashidhar. Tuning current rectification across molecular junctions. *Nanotechnology*, 15(7):S489–S493, 2004. (page 47).
- [86] B. Larade and A. M. Bratkovsky. Current rectification by simple molecular quantum dots: An ab initio study. *Physical Review B*, 68(23), 2003. (page 47).
- [87] S. H. Ke, W. T. Yang, and H. U. Baranger. Quantum-Interference-Controlled Molecular Electronics. *Nano Letters*, 8(10):3257–3261, 2008. (page 47).

- [88] J. S. Meisner, S. Ahn, S. V. Aradhya, et al. Importance of Direct Metal-pi Coupling in Electronic Transport Through Conjugated Single-Molecule Junctions coupling in electronic transport through conjugated single-molecule junctions. *Journal of the American Chemical Society*, 134(50):20440–20445, 2012. (pages 47, 48, 49, 50).
- [89] Y. S. Park, J. R. Widawsky, M. Kamenetska, et al. Frustrated Rotations in Single-Molecule Junctions. *Journal of the American Chemical Society*, 131(31):10820–10821, 2009. (pages 48, 84, 85, 91, 98).
- [90] Troels Markussen, Robert Stadler, and Kristian S. Thygesen. Graphical prediction of quantum interference-induced transmission nodes in functionalized organic molecules. *Physical Chemistry Chemical Physics*, 13(32):14311–14317, 2011. (page 48).
- [91] L. Venkataraman, J. E. Klare, I. W Tam, et al. Single-Molecule Circuits with Well-Defined Molecular Conductance. *Nano Letters*, 6(3):458 – 462, 2006. (page 48).
- [92] J. R. Widawsky, M. Kamenetska, J. Klare, et al. Measurement of voltage-dependent electronic transport across amine-linked single-molecular-wire junctions. *Nanotechnology*, 20(43):434009, 2009. (pages 48, 50, 51, 78, 88).
- [93] M. Kamenetska, M. Koentopp, A. Whalley, et al. Formation and Evolution of Single-Molecule Junctions. *Physical Review Letters*, 102(12):126803, 2009. (pages 48, 87).
- [94] S. M. Wu, M. T. Gonzalez, R. Huber, et al. Molecular junctions based on aromatic coupling. *Nature Nanotechnology*, 3(9):569–574, 2008. (page 49).
- [95] J. S. Meisner, M. Kamenetska, M. Krikorian, et al. A Single-Molecule Potentiometer. *Nano Letters*, 11(4):1575–1579, 2011. (page 49).

- [96] Pierre Darancet, Jonathan R. Widawsky, Hyoung Joon Choi, Latha Venkataraman, and Jeffrey B. Neaton. Quantitative Current-Voltage Characteristics in Molecular Junctions from First Principles. *Nano Letters*, 12(12):6250–6254, 2012. (page 52).
- [97] J. R. Widawsky, W. Chen, H. Vazquez, et al. Length-Dependent Thermopower of Highly Conducting Au-C Bonded Single Molecule Junctions. *Nano Letters*, 13(6):2889–2894, 2013. (pages 52, 60, 83, 84, 98).
- [98] D. Fischer, A. Curioni, and W. Andreoni. Decanethiols on gold: The structure of self-assembled monolayers unraveled with computer simulations. *Langmuir*, 19(9):3567–3571, 2003. (page 59).
- [99] H. Hakkinen. The gold-sulfur interface at the nanoscale. *Nature Chemistry*, 4(6):443–455, 2012. (page 59).
- [100] J. C. Love, L. A. Estroff, J. K. Kriebel, R. G. Nuzzo, and G. M. Whitesides. Self-assembled monolayers of thiolates on metals as a form of nanotechnology. *Chemical Reviews*, 105(4):1103–1169, 2005. (page 59).
- [101] A. Ulman. Formation and structure of self-assembled monolayers. *Chemical Reviews*, 96(4):1533–1554, 1996. (page 59).
- [102] C. Li, I. Pobelov, T. Wandlowski, et al. Charge transport in single Au vertical bar alkanedithiol vertical bar Au junctions: Coordination geometries and conformational degrees of freedom. *Journal of the American Chemical Society*, 130(1):318–326, 2008. (page 59).
- [103] J. A. Rodriguez, J. Dvorak, T. Jirsak, et al. Coverage effects and the nature of the metal-sulfur bond in S/Au(111): High-resolution photoemission and density-

- functional studies. *Journal of the American Chemical Society*, 125(1):276–285, 2003. (page 59).
- [104] H. Basch, R. Cohen, and M. A. Ratner. Interface geometry and molecular junction conductance: Geometric fluctuation and stochastic switching. *Nano Letters*, 5(9):1668–1675, 2005. (page 59).
- [105] M. Yu, N. Bovet, C. J. Satterley, et al. True nature of an archetypal self-assembly system: Mobile Au-thiolate species on Au(111). *Physical Review Letters*, 97(16), 2006. (page 59).
- [106] M. H. Schoenfisch and J. E. Pemberton. Air stability of alkanethiol self-assembled monolayers on silver and gold surfaces. *Journal of the American Chemical Society*, 120(18):4502–4513, 1998. (page 59).
- [107] L. Venkataraman, J. E. Klare, I. W. Tam, et al. Single-molecule circuits with well-defined molecular conductance. *Nano Letters*, 6(3):458–462, 2006. (pages 59, 78).
- [108] Z. L. Cheng, R. Skouta, H. Vazquez, et al. In situ formation of highly conducting covalent Au-C contacts for single-molecule junctions. *Nature Nanotechnology*, 6(6):353–357, 2011. (pages 60, 64, 66, 70).
- [109] L. Laurentius, S. R. Stoyanov, S. Gusalov, et al. Diazonium-Derived Aryl Films on Gold Nanoparticles: Evidence for a Carbon-Gold Covalent Bond. *Acs Nano*, 5(5):4219–4227, 2011. (page 60).
- [110] A. M. Ricci, E. J. Calvo, S. Martin, and R. J. Nichols. Electrochemical Scanning Tunneling Spectroscopy of Redox-Active Molecules Bound by Au-C Bonds. *Journal of the American Chemical Society*, 132(8):2494–+, 2010. (page 60).

- [111] Sheng Zhang, Kusum L. Chandra, and Christopher B. Gorman. Self-assembled monolayers of terminal alkynes on gold. *Journal of the American Chemical Society*, 129(16):4876–+, 2007. (page 60).
- [112] F. Scholz, E. Kaletova, E. S. Stensrud, et al. Formation of n-Alkyl Mono layers by Organomercury Deposition on Gold. *Journal of Physical Chemistry Letters*, 4(16):2624–2629, 2013. (pages 60, 63).
- [113] Wenjing Hong, Hui Li, Shi-Xia Liu, et al. Trimethylsilyl-Terminated Oligo(phenylene ethynylene)s: An Approach to Single-Molecule Junctions with Covalent Au-C sigma-Bonds. *Journal of the American Chemical Society*, 134(47):19425–19431, 2012. (page 60).
- [114] Wenbo Chen, Jonathan R. Widawsky, Héctor Vázquez, et al. Highly Conducting pi-Conjugated Molecular Junctions Covalently Bonded to Gold Electrodes-Conjugated Molecular Junctions Covalently Bonded to Gold Electrodes. *Journal of the American Chemical Society*, 133(43):17160–17163, 2011. (pages 60, 78, 82, 83, 91, 98).
- [115] Arunabh Batra, Pierre Darancet, Qishui Chen, et al. Tuning Rectification in Single-Molecular Diodes. *Nano Letters*, 13(12):6233–6237, 2013. (pages 60, 76).
- [116] G. Henkelman, B. P. Uberuaga, and H. Jonsson. A climbing image nudged elastic band method for finding saddle points and minimum energy paths. *Journal of Chemical Physics*, 113(22):9901–9904, 2000. (page 61).
- [117] Wenbo Chen, Jonathan R. Widawsky, Hector Vazquez, et al. Highly Conducting pi-Conjugated Molecular Junctions Covalently Bonded to Gold Electrodes. *Journal of the American Chemical Society*, 133(43):17160–17163, 2011. (pages 61, 66).

- [118] J. Ashley Taylor, Sailesh M. Merchant, and D. L. Perry. Study of the oxidation of gold-tin preforms using x-ray photoelectron spectroscopy. *Journal of Applied Physics*, 78(9):5356–5361, 1995. (page [62](#)).
- [119] G. M. Bancroft, I. Adams, H. Lampe, and T. K. Sham. Esca Study of Sn Organometallic Compounds - Solid-State Broadening Effects. *Journal of Electron Spectroscopy and Related Phenomena*, 9(3):191–204, 1976. (page [62](#)).
- [120] J. Bjork, F. Hanke, and S. Stafstrom. Mechanisms of Halogen-Based Covalent Self-Assembly on Metal Surfaces. *Journal of the American Chemical Society*, 135(15):5768–5775, 2013. (pages [63](#), [104](#), [106](#), [107](#)).
- [121] A. Laforgue, T. Addou, and D. Belanger. Characterization of the deposition of organic molecules at the surface of gold by the electrochemical reduction of aryl diazonium cations. *Langmuir*, 21(15):6855–6865, 2005. (page [63](#)).
- [122] G. Kresse and J. Furthmuller. Efficient iterative schemes for ab initio total-energy calculations using a plane-wave basis set. *Physical Review B*, 54(16):11169–11186, 1996. (pages [66](#), [71](#), [73](#)).
- [123] P. E. Blochl. Projector Augmented-Wave Method. *Physical Review B*, 50(24):17953–17979, 1994. (pages [66](#), [71](#)).
- [124] J. P. Perdew and A. Zunger. Self-Interaction Correction to Density-Functional Approximations for Many-Electron Systems. *Physical Review B*, 23(10):5048–5079, 1981. (pages [66](#), [71](#)).
- [125] J. Klimes, D. R. Bowler, and A. Michaelides. Van der Waals density functionals applied to solids. *Physical Review B*, 83(19), 2011. (page [66](#)).

- [126] J. Klimes, D. R. Bowler, and A. Michaelides. Chemical accuracy for the van der Waals density functional. *Journal of Physics-Condensed Matter*, 22(2), 2010. (pages 66, 71).
- [127] D. Sheppard, R. Terrell, and G. Henkelman. Optimization methods for finding minimum energy paths. *Journal of Chemical Physics*, 128(13), 2008. (page 67).
- [128] Dushant Khobragade, Elizabeth S. Stensrud, Małgorzata Mucha, et al. Preparation of Covalent Long-Chain Trialkylstannyl and Trialkylsilyl Salts and an Examination of their Adsorption on Gold. *Langmuir*, 26(11):8483–8490, 2010. (page 69).
- [129] J. J. Mortensen, L. B. Hansen, and K. W. Jacobsen. Real-space grid implementation of the projector augmented wave method. *Physical Review B*, 71(3):035109, 2005. (page 74).
- [130] J. J. Yeh and I. Lindau. Atomic Subshell Photoionization Cross-Sections and Asymmetry Parameters - 1 Less-Than-or-Equal-to Z Less-Than-or-Equal-to 103. *Atomic Data and Nuclear Data Tables*, 32(1):1–155, 1985. (page 75).
- [131] Arieh Aviram and Mark A Ratner. Molecular rectifiers. *Chemical Physics Letters*, 29(2):277–283, 1974. (page 77).
- [132] J. Taylor, M. Brandbyge, and K. Stokbro. Conductance switching in a molecular device: The role of side groups and intermolecular interactions. *Physical Review B*, 68(12):1211011–1211014, 2003. (pages 77, 78).
- [133] R. Stadler, V. Geskin, and J. Cornil. A theoretical view of unimolecular rectification. *Journal of Physics: Condensed Matter*, 20(37), 2008. (page 77).
- [134] NJ Tao. Electron transport in molecular junctions. *Nature Nanotechnology*, 1(3):173–181, 2006. (page 77).

- [135] Richard L McCreery and Adam Johan Bergren. Progress with molecular electronic junctions: meeting experimental challenges in design and fabrication. *Advanced Materials*, 21(43):4303–4322, 2009. (page [77](#)).
- [136] M. S. Hybertsen, L. Venkataraman, J. E. Klare, et al. Amine-linked single-molecule circuits: systematic trends across molecular families. *Journal of Physics: Condensed Matter*, 20(37):374115, 2008. (page [77](#)).
- [137] E. Lortscher, B. Gotsmann, Y. Lee, et al. Transport Properties of a Single-Molecule Diode. *ACS Nano*, 6(6):4931–4939, 2012. (page [77](#)).
- [138] A Dhirani, P-H Lin, P Guyot-Sionnest, RW Zehner, and LR Sita. Self-assembled molecular rectifiers. *The Journal of Chemical Physics*, 106:5249, 1997. (page [77](#)).
- [139] JG Kushmerick, DB Holt, JC Yang, et al. Metal-molecule contacts and charge transport across monomolecular layers: Measurement and theory. *Physical Review Letters*, 89(8):086802, 2002. (page [77](#)).
- [140] Weidong Tian, Supriyo Datta, Seunghun Hong, et al. Conductance spectra of molecular wires. *The Journal of Chemical Physics*, 109:2874, 1998. (page [78](#)).
- [141] J. Taylor, M. Brandbyge, and K. Stokbro. Theory of rectification in tour wires: The role of electrode coupling. *Physical Review Letters*, 89(13):1383011–1383014, 2002. (page [78](#)).
- [142] John P Perdew, Kieron Burke, and Yue Wang. Generalized gradient approximation for the exchange-correlation hole of a many-electron system. *Physical Review B*, 54(23):16533, 1996. (pages [81](#), [91](#), [92](#)).
- [143] M. Brandbyge, J. L. Mozos, P. Ordejon, J. Taylor, and K. Stokbro. Density-functional

- method for nonequilibrium electron transport. *Physical Review B*, 65(16):165401, 2002. (page 81).
- [144] Pierre Darancet, Jonathan R. Widawsky, Hyoung Joon Choi, Latha Venkataraman, and Jeffrey B. Neaton. Quantitative Current-Voltage Characteristics in Molecular Junctions from First Principles. *Nano Letters*, 12(12):6250–6254, 2012. (pages 82, 84, 92, 96).
- [145] Michael Frei, Sriharsha V. Aradhya, Mark S. Hybertsen, and Latha Venkataraman. Linker Dependent Bond Rupture Force Measurements in Single-Molecule Junctions. *Journal of the American Chemical Society*, 134(9):4003–4006, 2012. (page 82).
- [146] Hyoung Joon Choi, L. Cohen Marvin, and G. Louie Steven. First-principles scattering-state approach for nonlinear electrical transport in nanostructures. *Physical Review B*, 76(15):155420, 2007. (pages 82, 92).
- [147] Aron J Cohen, Paula Mori-Sánchez, and Weitao Yang. Insights into current limitations of density functional theory. *Science*, 321(5890):792–794, 2008. (page 82).
- [148] Khoong Hong Khoo, JB Neaton, Young Woo Son, Marvin L Cohen, and Steven G Louie. Negative differential resistance in carbon atomic wire-carbon nanotube junctions. *Nano Letters*, 8(9):2900–2905, 2008. (page 84).
- [149] Pablo Ordejón, Emilio Artacho, and José M Soler. Self-consistent order-N density-functional calculations for very large systems. *Physical Review B*, 53(16):R10441, 1996. (page 91).
- [150] José M Soler, Emilio Artacho, Julian D Gale, et al. The SIESTA method for ab initio

- order-N materials simulation. *Journal of Physics: Condensed Matter*, 14(11):2745, 2002. (page 91).
- [151] Su Ying Quek, Latha Venkataraman, Hyoung Joon Choi, et al. Amine-gold linked single-molecule circuits: experiment and theory. *Nano Letters*, 7(11):3477–3482, 2007. (page 92).
- [152] Su Ying Quek, Hyoung Joon Choi, Steven G Louie, and Jeffrey B Neaton. Length dependence of conductance in aromatic single-molecule junctions. *Nano Letters*, 9(11):3949–3953, 2009. (page 92).
- [153] Xiaolin Li, Xinran Wang, Li Zhang, Sangwon Lee, and Hongjie Dai. Chemically Derived, Ultrasmooth Graphene Nanoribbon Semiconductors. *Science*, 319(5867):1229–1232, 2008. (page 103).
- [154] J. Cai, P. Ruffieux, R. Jaafar, et al. Atomically precise bottom-up fabrication of graphene nanoribbons. *Nature*, 466(7305):470–3, 2010. (pages 103, 104).
- [155] Yen-Chia Chen, Dimas G. de Oteyza, Zahra Pedramrazi, et al. Tuning the Band Gap of Graphene Nanoribbons Synthesized from Molecular Precursors. *ACS Nano*, 7(7):6123–6128, 2013. (page 103).
- [156] C. Bronner, S. Stremlau, M. Gille, et al. Aligning the band gap of graphene nanoribbons by monomer doping. *Angewandte Chemie International Edition*, 52(16):4422–5, 2013. (page 103).
- [157] M. Xi and B. E. Bent. Mechanisms of the Ullmann Coupling Reaction in Adsorbed Monolayers. *Journal of the American Chemical Society*, 115(16):7426–7433, 1993. (page 103).

- [158] Zheyuan Chen, Pierre Darancet, Lei Wang, et al. Physical Adsorption and Charge Transfer of Molecular Br₂ on Graphene. *ACS Nano*, 2014. (page 106).
- [159] Marco Bieri, Matthias Treier, Jinming Cai, et al. Porous graphenes: two-dimensional polymer synthesis with atomic precision. *Chemical Communications*, (45):6919–6921, 2009. (page 106).
- [160] Denis Syomin and Bruce E. Koel. Adsorption of iodobenzene (C₆H₅I) on Au(111) surfaces and production of biphenyl (C₆H₅–C₆H₅). *Surface Science*, 490(3):265–273, 2001. (page 106).
- [161] Marco Bieri, Manh-Thuong Nguyen, Oliver Gröning, et al. Two-Dimensional Polymer Formation on Surfaces: Insight into the Roles of Precursor Mobility and Reactivity. *Journal of the American Chemical Society*, 132(46):16669–16676, 2010. (page 107).
- [162] H. Agren, O. Vahtras, and V. Carravetta. Near-Edge core photoabsorption in polyacenes - Model molecules for graphite. *Chemical Physics*, 196(1-2):47–58, 1995. (page 108).
- [163] D Pacilé, M Papagno, A Fraile Rodríguez, et al. Near-edge X-ray absorption fine-structure investigation of graphene. *Physical review letters*, 101(6):066806, 2008. (page 108).
- [164] J Ziroff, P Gold, A Bendounan, F Forster, and F Reinert. Adsorption energy and geometry of physisorbed organic molecules on Au (111) probed by surface-state photoemission. *Surface Science*, 603(2):354–358, 2009. (pages 108, 109, 111).
- [165] C. Bronner, F. Leyssner, S. Stremmlau, et al. Electronic structure of a subnanometer wide bottom-up fabricated graphene nanoribbon: End states, band gap, and dispersion. *Physical Review B*, 86(8):085444, 2012. (page 109).

- [166] M. Koch, F. Ample, C. Joachim, and L. Grill. Voltage-dependent conductance of a single graphene nanoribbon. *Nature Nanotechnology*, 7(11):713–717, 2012. (page 109).
- [167] S. Linden, D. Zhong, A. Timmer, et al. Electronic Structure of Spatially Aligned Graphene Nanoribbons on Au(788). *Physical Review Letters*, 108(21):216801, 2012. (page 109).
- [168] Pascal Ruffieux, Jinming Cai, Nicholas C. Plumb, et al. Electronic Structure of Atomically Precise Graphene Nanoribbons. *ACS Nano*, 6(8):6930–6935, 2012. (page 109).
- [169] A. Varykhalov, J. Sánchez-Barriga, A. M. Shikin, et al. Electronic and Magnetic Properties of Quasifreestanding Graphene on Ni. *Physical Review Letters*, 101(15):157601, 2008. (page 109).
- [170] A. Bostwick, T. Ohta, T. Seyller, K. Horn, and E. Rotenberg. Quasiparticle dynamics in graphene. *Nature Physics*, 3(1):36–40, 2007. (page 109).
- [171] S. D. Kevan and R. H. Gaylord. High-resolution photoemission study of the electronic structure of the noble-metal (111) surfaces. *Physical Review B*, 36(11):5809–5818, 1987. (page 109).
- [172] S. LaShell, B. A. McDougall, and E. Jensen. Spin Splitting of an Au(111) Surface State Band Observed with Angle Resolved Photoelectron Spectroscopy. *Physical Review Letters*, 77(16):3419–3422, 1996. (page 109).
- [173] Paolo Giannozzi, Stefano Baroni, Nicola Bonini, et al. QUANTUM ESPRESSO: a modular and open-source software project for quantum simulations of materials. *Journal of Physics: Condensed Matter*, 21(39):395502, 2009. (pages 110, 112).

- [174] G. Giovannetti, P. A. Khomyakov, G. Brocks, et al. Doping Graphene with Metal Contacts. *Physical Review Letters*, 101(2):026803, 2008. (page [111](#)).
- [175] P. A. Khomyakov, G. Giovannetti, P. C. Rusu, et al. First-principles study of the interaction and charge transfer between graphene and metals. *Physical Review B*, 79(19):195425, 2009. (page [111](#)).
- [176] D. Cvetko, A. Lausi, A. Morgante, et al. Compact He Beam Scattering Apparatus for Surface Studies. *Measurement Science and Technology*, 3(10):997–1000, 1992. (page [113](#)).